
Electronic Thesis and Dissertation Repository

11-3-2017 4:30 PM

Functional Design and Analysis of a Linked Shoulder Prosthesis

Emily West, *The University of Western Ontario*

Supervisor: Dr. Louis Ferreira, *The University of Western Ontario*

Co-Supervisor: Dr. George Athwal, *The University of Western Ontario*

A thesis submitted in partial fulfillment of the requirements for the Master of Engineering
Science degree in Biomedical Engineering

© Emily West 2017

Follow this and additional works at: <https://ir.lib.uwo.ca/etd>



Part of the [Biomedical Devices and Instrumentation Commons](#)

Recommended Citation

West, Emily, "Functional Design and Analysis of a Linked Shoulder Prosthesis" (2017). *Electronic Thesis and Dissertation Repository*. 5149.

<https://ir.lib.uwo.ca/etd/5149>

This Dissertation/Thesis is brought to you for free and open access by Scholarship@Western. It has been accepted for inclusion in Electronic Thesis and Dissertation Repository by an authorized administrator of Scholarship@Western. For more information, please contact wlsadmin@uwo.ca.

Abstract

Persistent shoulder instability following joint arthroplasty remains a concern with mixed outcomes following clinical and surgical intervention. Thus, a linked universal joint implant was developed and functionally analyzed. A virtual model of the linked implant was developed and implanted in a 3D bony specimen to measure the available circumduction range of motion. Stresses in the implant were estimated using finite element analysis based on joint loads during activities of daily life. The glenoid fixation stress was evaluated using finite element analysis.

The results of this feasibility study show the linked implant is predicted to restore normal range of motion, and withstand expected joint loads without yield or fatigue failure. Bone fixation stress remains a concern, depending on the implant configuration and aggressive joint loading.

Keywords

Shoulder arthroplasty, Chronic Shoulder Instability, Salvage Procedure, Universal Joint, Linked Implant.

Co-Authorship Statement

Chapter 1:	Emily West – sole author
Chapter 2:	Emily West – study design, data collection, statistical analysis, wrote manuscript Elizabeth Litchfield – data collection Louis Ferreira – study design, reviewed manuscript George Athwal – study design, reviewed manuscript
Chapter 3:	Emily West – study design, data collection, statistical analysis, wrote manuscript Louis Ferreira – study design, reviewed manuscript
Chapter 4:	Emily West – study design, data collection, statistical analysis, wrote manuscript Nikolas Knowles – study design Louis Ferreira – study design, reviewed manuscript George Athwal – study design
Chapter 5:	Emily West – sole author

Acknowledgments

First of all, I would like to thank my supervisors, Dr. Louis Ferreira and Dr. George Athwal. Your mentorship, guidance, and encouragement generously provided throughout my graduate studies are so appreciated. Louis, thank you for your patience and coaching during the entirety of this project. This work would not have been possible without your contributions and advice. George, the excitement you show for the possibilities of this research is infectious and motivating. Thank you for sharing your expertise with me; your involvement has greatly improved this research project. Thank you both.

Also, thank you to all the students at the HULC; you've made the last couple years a lot of fun. I am particularly grateful to Nik, thank you for your guidance and sharing your knowledge of finite element studies. Your assistance in generating the models was invaluable. Elizabeth, thank you for your meticulous data collection.

Finally, thank you to my parents for your unending support and encouragement. Steve, for being my sounding board, my cheerleader and always believing in me. You are the best.

Table of Contents

Abstract	i
Co-Authorship Statement.....	ii
Acknowledgments	iii
Table of Contents	iv
List of Tables.....	vii
List of Figures	viii
Chapter 1	1
1 Introduction	1
1.1 Shoulder Anatomy	1
1.2 Shoulder Instability	7
1.2.1 Causes of Shoulder Instability	7
1.3 Shoulder Arthroplasty State of the Art.....	9
1.3.1 Total Shoulder Arthroplasty	9
1.3.2 Reverse Shoulder Arthroplasty	10
1.3.3 Constrained Shoulder Reconstruction	12
1.4 Revision Surgical Challenges	14
1.5 Development of a Linked Shoulder Implant	15
1.5.1 Design Objectives and Rationale for a Universal Joint Implant	16
1.6 Thesis Rationale.....	17
1.7 Objectives and Hypotheses.....	18
1.8 Thesis Overview	19
Chapter 2.....	20
2 Range of Motion of a Linked Shoulder Implant with Variable Configurations.....	20
2.1 Development of a Universal Joint Shoulder Implant.....	20

2.1.1	Universal Joint Components	21
2.2	Development of Virtual Prototype	24
2.3	Virtual Implantation of Universal Joint Implant into Bony Geometry	25
2.4	Parameter Variations	27
2.5	Range of Motion Testing Protocol.....	32
2.6	Range of Motion Results	35
2.7	Statistical Analysis of Range of Motion Results	41
2.8	Conclusions	54
Chapter 3.....		59
3	Finite Element Analysis of the Linked Implant in Activities of Daily Living	59
3.1	In-vivo Loading of Clinical Implants.....	59
3.2	Materials and Methods.....	60
3.2.1	Material Selection.....	60
3.2.2	Hertzian Contact Stress Analysis	63
3.2.3	Static Yielding Analysis	65
3.2.4	Fatigue Failure Analysis	70
3.3	Results	71
3.3.1	Hertzian Contact Stress Analysis	71
3.3.2	Static Failure Analysis	71
3.3.3	Fatigue Failure Analysis	79
3.4	Conclusion.....	83
Chapter 4.....		85
4	Finite Element Analysis of the Glenoid Component Fixation	85
4.1	Introduction	85
4.2	Materials and Methods.....	89
4.3	Results	94

4.4 Conclusions	103
Chapter 5.....	106
5 General Conclusions and Future Work.....	106
5.1 Summary and General Discussion	106
5.2 Strengths and Limitations.....	108
5.3 Future Work.....	109
5.4 Conclusion.....	110
References or Bibliography	111
Appendix A - Glossary of Medical Terms.....	122
Appendix B – Detailed Part Drawings of Linked Implant	124
129	
Appendix C – Individual Range of Motion Plots for 6 Repeated Configurations	131
Appendix D: Tolerance Calculations for Pin and Center Trunnion.....	135
Appendix E: Hertzian Contact Stress Calculations	136
Appendix F: Fatigue Calculations	138
Appendix G: Glenoid Bone Fixation Stress.....	140
Curriculum Vitae	145

List of Tables

Table 1.1: Relevant Muscles and Contributions to Shoulder Function	5
Table 2.1: Anthropometric data of specimens used for range of motion testing	34
Table 2.2: Maximum range of motion for 24 configurations in medium specimen	38
Table 2.3: Pairwise comparisons for mean differences between configurations	46
Table 2.4: Pairwise comparisons for mean differences in Adduction range of motion	48
Table 2.5: Pairwise comparisons of mean differences in Forward Elevation.....	50
Table 2.6: Pairwise comparisons of mean differences in Superior Elevation	51
Table 2.7: Pairwise comparisons of mean differences in Posterior Elevation.....	52
Table D.1: Tolerance Dimensions for Pin, Center Trunnion, and Yoke holes	135
Table E.1: Variables used for Hertzian contact stress calculations.....	136
Table F.1: Fatigue Calculations and Intermediate Values	139
Table G.1: Central Screw Bone Stresses	140
Table G.2: Anterior Screw Bone Stresses	141
Table G.3: Superior Screw Bone Stresses	142
Table G.4: Posterior Screw Bone Stresses.....	143
Table G.5: Inferior Screw Bone Stresses	144

List of Figures

Figure 1.1: Planes of the body and rotational motions of the shoulder	2
Figure 1.2: Bony anatomy of the shoulder joint.....	3
Figure 1.3: Soft tissue structures of the shoulder	6
Figure 1.4: Total Shoulder Arthroplasty.....	10
Figure 1.5: Reverse Shoulder Arthroplasty	11
Figure 1.6: Torque transmitting universal joint (pin and block style).....	15
Figure 2.1: Components of proposed linked universal joint implant	21
Figure 2.2: Y-yoke universal joint	25
Figure 2.3: Positioning of the glenoid baseplate	26
Figure 2.4: Glenoid yoke orientation variation	28
Figure 2.5: Glenoid yoke position variation	29
Figure 2.6: Glenoid yoke tilt variation	30
Figure 2.7: Offset distance of hinge joints in center trunnion variation	31
Figure 2.8: Range of motion template	33
Figure 2.9: Joint angle measurement	36
Figure 2.10: Numbered spokes on the template to divide range of motion measurements into separated movements.....	40
Figure 2.11: Overall mean circumduction range of motion.....	42
Figure 2.12: Comparison of mean circumduction range of motion angles between 6 configurations.....	43

Figure 2.13: Individual range of motion spheres for 6 configurations	44
Figure 2.14: Comparison of 6 configurations across all 30 angular locations.....	45
Figure 2.15: Comparison of 6 configurations in Adduction	47
Figure 2.16: Comparison of 6 configurations for Forward Elevation range of motion.....	49
Figure 2.17: Comparison of 6 configurations for Superior Elevation range of motion	50
Figure 2.18: Comparison of 6 configurations for Posterior Elevation range of motion.....	52
Figure 2.19: Angles used for repeatability analysis	54
Figure 2.20: Angle between scapular plane and frontal plane. Birds eye view.	56
Figure 3.1: Material selection graph.....	62
Figure 3.2: Loading scenarios used for analysis	65
Figure 3.3: Local Coordinate System	66
Figure 3.4: Boundary conditions of humeral yoke	67
Figure 3.5: Boundary conditions of center trunnion assembly	68
Figure 3.6: Boundary conditions of glenoid yoke	69
Figure 3.7: Von Mises stress distribution in the humeral yoke under loaded 90° abduction .	72
Figure 3.8: Von Mises stress in humeral yoke (CoCrMo) under 90° loaded abduction by region	73
Figure 3.9: Von Mises stress distribution in the glenoid yoke under loaded 90° abduction ..	73
Figure 3.10: Von Mises stress in glenoid yoke (CoCrMo) under 90° loaded abduction by region	74
Figure 3.11: Von Mises stress distribution in the center trunnion subassembly under loaded 90° abduction	75

Figure 3.12: Von Mises stress in center trunnion (CoCrMo) under loaded 90° abduction by region	75
Figure 3.13: Von Mises stress distribution in the humeral yoke under loaded 90° forward elevation.....	76
Figure 3.14: Von Mises stress in humeral yoke (CoCrMo) under loaded 90° forward elevation by region	77
Figure 3.15: Von Mises stress distribution in the glenoid yoke under loaded 90° forward elevation.....	77
Figure 3.16: Von Mises stress in glenoid yoke (CoCrMo) under loaded 90° forward elevation by region	78
Figure 3.17: Von Mises stress distribution in the center trunnion subassembly under loaded 90° forward elevation	78
Figure 3.18: Von Mises stress in center trunnion (CoCrMo) under loaded 90° forward elevation by region	79
Figure 3.19: Von Mises stress distribution in the humeral yoke under unloaded 40° abduction.....	80
Figure 3.20: Von Mises stress in humeral yoke (CoCrMo) under unloaded 40° abduction by region	80
Figure 3.21: Von Mises stress distribution in the glenoid yoke under unloaded 40° abduction	81
Figure 3.22: Von Mises stress in glenoid yoke (CoCrMo) under unloaded 40° abduction by region	81
Figure 3.23: Von Mises stress distribution in the center trunnion subassembly under unloaded 40° abduction	82

Figure 3.24: Von Mises stress in center trunnion (CoCrMo) under unloaded 40° abduction by region	82
Figure 4.1: Cortical shell surrounding inner trabeculae	86
Figure 4.2: Lateralization of the abductor hinges for comparison	88
Figure 4.3: Scapula with implanted glenoid baseplate	90
Figure 4.4: FEA model of implanted scapula showing loading and boundary conditions.	92
Figure 4.5: Stress distribution in glenoid face	96
Figure 4.6: Glenoid bone stress: 1 BW Shear and Compressive Load.....	97
Figure 4.7: Glenoid Bone Stress: Unloaded 40° Abduction	98
Figure 4.8: Glenoid Bone Stress: Loaded 90° Abduction.....	99
Figure 4.9: Glenoid Bone Stress: Loaded 90° Forward Elevation	100
Figure 4.10: Glenoid Bone Stress: Unsupported Arm Weight	101
Figure 4.11: Glenoid Bone Stress: Unsupported Arm Weight plus 10 kg weight	102
Figure C.1: Circumduction RoM for configuration 1	131
Figure C.2: Circumduction RoM for configuration 2	132
Figure C.3: Circumduction RoM for configuration 3	132
Figure C.4: Circumduction RoM for configuration 4	133
Figure C.5: Circumduction RoM for configuration 5	133
Figure C.6: Circumduction RoM for configuration 6	134

Chapter 1

1 Introduction

OVERVIEW: The introductory chapter describes the shoulder joint and the relevant anatomical structures involved in the joint's function. Since the designed implant aims to treat chronic shoulder instability, the symptoms and causes of instability are discussed. Current surgical treatment options for shoulder instability and related pathology are presented, along with their successes and limitations. The chapter concludes with a rationale and objective for the design of a novel linked shoulder implant based off a universal joint.

1.1 Shoulder Anatomy

The shoulder joint (glenohumeral joint) is a shallow ball and socket joint, comprised of the humeral head articulating against the glenoid fossa of the scapula. The shape of the glenoid fossa is a shallow dish, which allows both translation and rotation of the humeral head against it. This combination of movements allows the glenohumeral joint to have the largest range of motion in the human body. Unlike most other joints which are mechanically stabilized and primarily constrained by the shape of the articular bony surface, the glenohumeral joint is mainly stabilized by soft tissues, primarily the muscles of the rotator cuff. This soft tissue stabilization allows a larger range of motion, but also introduces increased opportunity for instability, especially in cases where the rotator cuff is damaged.

The glenohumeral joint has three rotational degrees of freedom; it is capable of abduction/adduction (rotation about the sagittal plane), forward and backward flexion (rotation about the frontal plane), and internal/ external rotation around the humeral axis. (Figure 1.1) The humeral head simultaneously translates against the glenoid socket as it rotates towards the extremes of motion.¹ The magnitude of the humeral head's translation within the glenoid was reported to be under 2 mm by Graichen et al.² and reported as high as 4 mm by Howell et al. with abnormal translation patterns recorded in unstable shoulders.¹

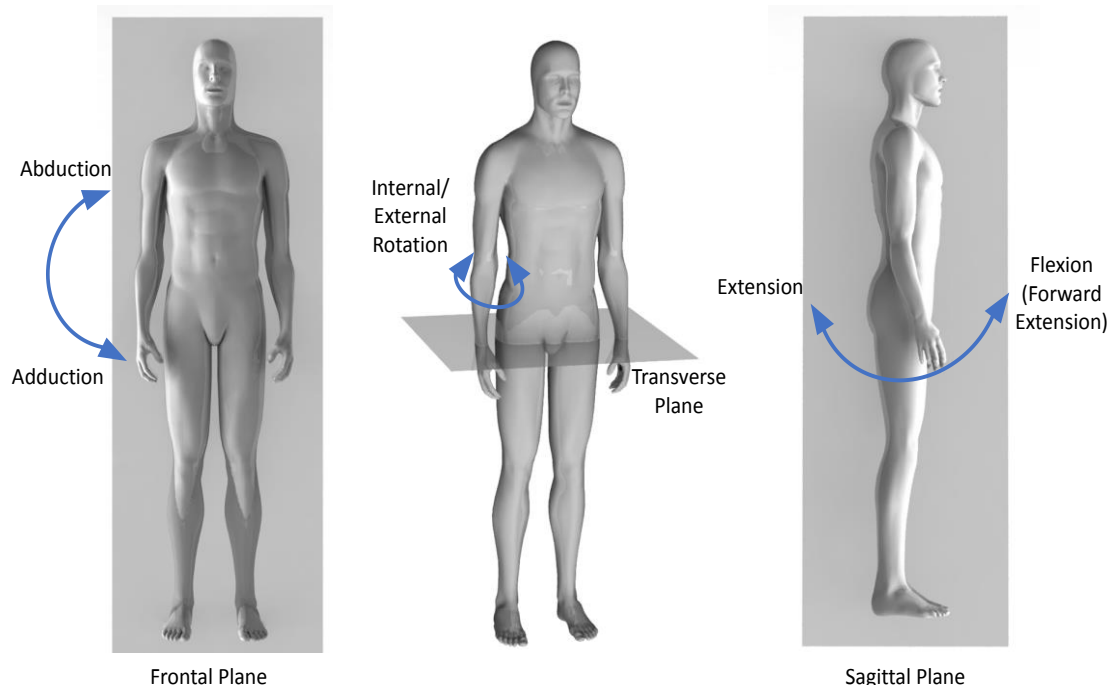


Figure 1.1: Planes of the body and rotational motions of the shoulder

Abduction-adduction occur within the frontal plane, and constitute a rotation about the transverse plane. Flexion-extension movement occurs within the sagittal plane, and is a rotation about the frontal plane. Internal and external rotation is rotation about the long axis of the arm. It is not confined to any plane, and can occur in conjunction with other motions of the joint.

The relevant bony surfaces of the humeral joint are described below and can be seen in Figure 1.2.

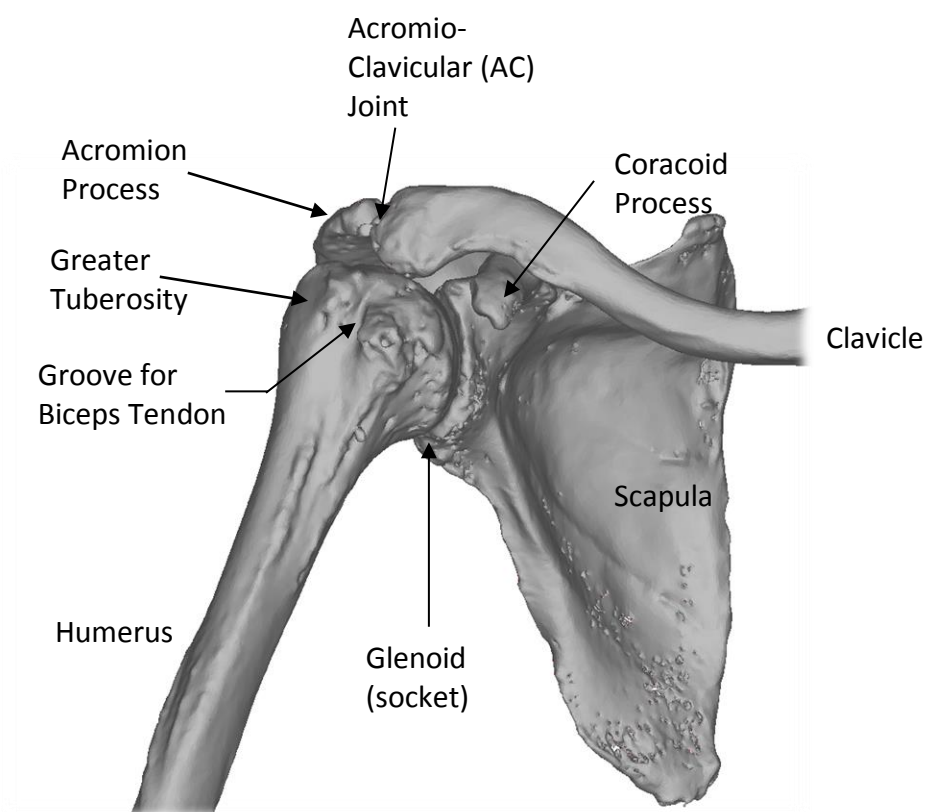


Figure 1.2: Bony anatomy of the shoulder joint

The humeral head is the most proximal surface of the humerus that articulates with the glenoid fossa of the scapula. It is estimated as a partial sphere, however, is closer to an ovoid shape, being longer in the superoinferior direction than the anteroposterior. It is covered in cartilage for a smooth articulation.

The glenoid fossa is a shallow socket on the lateral side of the scapula, forming the second half of the articulation couple comprising the glenohumeral joint. The glenoid surface is close to conforming to the humeral head, but some mismatch in curvature is present. It is also a small socket, covering only approximately a quarter of the humeral head. The low level of bony constraint is a major factor in allowing the large range of motion of the shoulder.

The scapula has two large bony prominences originating from the lateral superior section of the bone, above the glenoid fossa. The coracoid process is the more anterior of the two

processes, and serves as an attachment point for various ligaments that stabilize the joint. The acromion is the larger, posterior protrusion, which serves as a strut against the clavicle, and provides as an attachment site for the deltoid muscle. Both the coracoid and acromion, together with the ligaments that run between them, provide a superior mechanical stop to limit the superior translation of the humeral head, and may limit abduction if the tubercles are in a position to impinge on either the coracoid or acromion.

The superior part of the humerus has bony protrusions, known as the greater and lesser tuberosities. They encompass most of the superior half of the humeral head, and provide a nearly encompassing region for the insertions of the tendons of the rotator cuff, the primary stabilizers of the glenohumeral joint. The tuberosities (and bicipital groove between them) are also often used as surgical landmarks for implant positioning. The humeral shaft (diaphysis) forms the long axis of the humerus, and is the distal insertion of the deltoid.

The joint capsule contains thickenings that have been defined as ligaments that include three ligaments connecting the humeral head to the glenoid, wrapping around the anterior side of the joint. On the superior aspect of the joint, the coraco-humeral ligament wraps from the greater humeral tuberosity to the coracoid process.

Due to its relatively unconstrained geometry, the glenohumeral joint relies on muscles not only for effecting motion, but also to compress the joint for stability. The relevant soft tissue structures are described in Table 1.1 below.

Table 1.1: Relevant Muscles and Contributions to Shoulder Function

Muscle	Role
Deltoid	Abducts humerus Compress humeral head into glenoid fossa May compensate for deficient rotator cuff if the joint is reconstructed in a reverse ball and socket orientation
Rotator Cuff (Infraspinatus, teres minor, subscapularis, supraspinatus)	Encapsulates the humeral head and constrains the joint capsule for stability and arm motion
Joint capsule	Connects humeral head to glenoid and retains synovial fluid Starts loose when humerus is in neutral position, but tightens as humerus moves to extreme positions, providing additional stability when it is needed
Glenohumeral ligaments (Superior, Medial, Inferior)	Connects humeral head to the surface of scapula by wrapping across the anterior aspect of the joint
Trapezius	Rotates scapula with respect to thorax
Serratus anterior	Rotates scapula with respect to thorax
Pectoralis major	Large muscle forming anterior cover of glenohumeral joint. Adducts, and internally rotates humerus.
Latissimus dorsi	Large muscle covering posterior region of back and shoulder. Adducts, extends, and allows internal rotation of humerus.

These structures are illustrated in Figure 1.3 below:

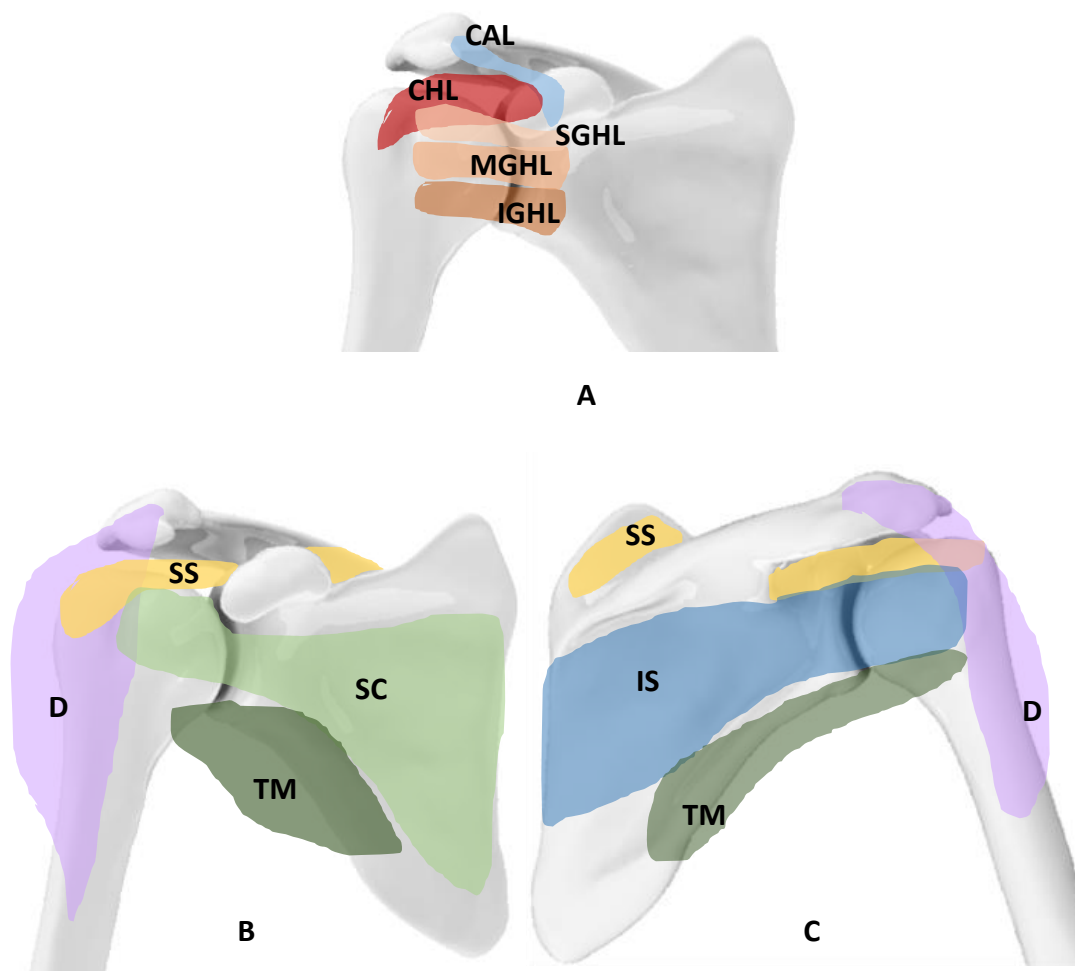


Figure 1.3: Soft tissue structures of the shoulder

(A): Anterior view showing ligaments of the shoulder. CAL: Coraco-acromial ligament. CHL: Coraco-humeral ligament. SGHL: Superior Glenohumeral ligament. MGHL: Medial Glenohumeral ligament. IGH: Inferior Glenohumeral ligament.

(B) Anterior view showing muscles of the shoulder. D: Deltoid. SS: Supraspinatus. Teres Minor. SC: Subscapularis.

(C) Posterior view showing muscles of the shoulder. IS: Infraspinatus.

1.2 Shoulder Instability

Chronic shoulder instability is characterized by excessive humeral head translation relative to the glenoid, and may cause recurrent subluxation or frequent dislocations with minimal dislocating force. Subluxation is defined by the humeral head resting in a partially dislocated state, typically the humeral head is translated from the stable position where the radial surfaces of the humeral head and the glenoid socket are concentric to a position where the humeral head rests eccentrically in the glenoid. Instability is associated with a loss of function of the joint due to joint pain, loss of range of motion, and apprehension or the sensation that the shoulder may dislocate.

1.2.1 Causes of Shoulder Instability

Shoulder instability may be caused by deficient rotator cuff muscles, glenoid morphology, or weakness in the muscles responsible for scapulothoracic motion.³⁻⁸

The rotator cuff is comprised of three muscle strands that wrap around the humeral head and connect it to the scapula. The rotator cuff envelopes the joint and compresses the humeral head into the glenoid as the arm moves. The combination of these functions makes the rotator cuff the primary stabilizer of the shoulder joint. If the rotator cuff is weak or damaged, it will be unable to properly constrain the humeral head to its centered, stabilized position, contributing to shoulder instability. If the cuff cannot be repaired, the shoulder will continue to be unstable.

The morphology of the glenoid fossa is also related to joint stability. A normal glenoid fossa, when viewed normal to the face, has a pear-shaped silhouette, with the inferior portion approximating a perfect circle. Traumatic injury can alter the shape of the glenoid rim, and cause irregularities in the inferior circularity. These irregularities have shown to be present in up to 90% of traumatically induced unstable glenohumeral joints.^{6,9} An intact glenoid rim plays an important role to provide a small lip which prevents excessive humeral head translation or subluxation. Additionally, instability is more likely if the glenoid is tilted inferiorly,^{4,5} since the inferior lip is not in a position to provide a physical barrier for the humeral head.

If instability is caused by glenoid rim defects or repairable rotator cuff injury, surgical treatments such as the Latarjet or Bankart procedures are usually successful in restoring stability to the joint.^{6,10,11} The Latarjet procedure repositions part of the coracoid and attaches it as a bone graft to the anterior portion of the glenoid, to restore the bony rim of the glenoid. The Bankart procedure involves suturing the joint capsule to the glenoid labrum.¹² While these surgeries are successful in restoring stability and range of motion in most patients, recurring instability and apprehension is documented in up to 10% of cases.¹²⁻¹⁴ Additionally, patients with a previous traumatic dislocation and surgical repair are at a higher risk of developing arthritis in the joint,^{13,14} and may be candidates for joint replacement as the arthritis progresses.

Shoulder arthroplasty aims to correct any abnormal glenoid morphology by reconstructing the joint so that the humeral head curvature is centered and conforming to the glenoid socket, but the success of the procedure will be dependent on surgical factors such as soft tissue balancing, and proper position and orientation of the components.¹⁵

Another factor in glenohumeral instability is the movement of the scapula. As the arm is abducted, the scapula also rotates upward, such that the glenoid fossa follows and supports the humeral head through its arc of motion. Typically, there is a 2:1 ratio between glenohumeral abduction and scapulothoracic rotation, which begins when the humerus is abducted past 60°.^{3,16,17} This rotation allows the glenoid to follow the humeral head through its arc of rotation and provide support from the inferior direction. The primary muscles responsible for scapulothoracic motion (serratus anterior and trapezius) retract the superior aspect of the scapula towards the midline of the body, allowing the humeral head to rotate and occupy this space. Weakness in the serratus anterior and trapezius⁸ has been shown to accompany anteroinferior instable shoulders as well as those with impingement syndrome.¹⁸ Impingement syndrome is related to instability because in both these conditions, the scapula is not sufficiently retracted to move the acromion process out of the humeral head's path as it would be in a healthy shoulder.¹⁹ If these muscles are not strong enough to affect the scapulothoracic rotation, the humeral head will not be adequately supported in abduction, and this is a contributing factor to instability.

1.3 Shoulder Arthroplasty State of the Art

One option for late stage shoulder pain or loss of function of the joint is the surgical replacement of the articular surfaces with prosthetic components, a procedure known as arthroplasty. Several implant designs are available and clinically used today.

1.3.1 Total Shoulder Arthroplasty

Total shoulder arthroplasty (TSA) is an effective treatment for several joint pathologies, including osteoarthritis, rheumatoid arthritis, severe humeral fracture, or avascular necrosis.^{20,21} In this procedure, the articular surface of the humeral head is resected per the plane of the articular neck, the humeral canal is reamed, and a metal implant that replicates the anatomic shape of the humerus is inserted, often cemented to fixate in place.^{22–25} On the scapular side, the glenoid is reamed smooth, and small holes are drilled into the bone for the fixation pegs, resulting in both articular surfaces replaced by prosthetic components. A smooth polyethylene implant to create a smooth bearing surface is then cemented in place. (Figure 1.4) TSA can restore pain free motion to the damaged shoulder, with generally good outcomes reported if the rotator cuff is intact.^{26,27} However, in cases with a deficient rotator cuff, a total shoulder arthroplasty can do little to restore motion or stability of the shoulder, and in this case the recommended alternative is a reverse total shoulder arthroplasty.²⁸

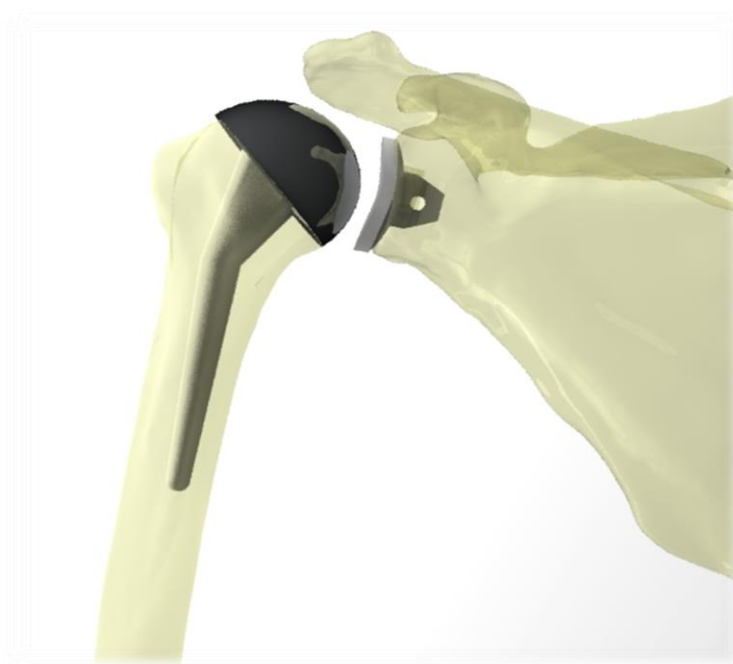


Figure 1.4: Total Shoulder Arthroplasty

Although an accepted treatment of shoulder pathology, in some cases the implant must be revised due to complications such as humeral head migration after rotator cuff degeneration, implant failure or malposition, infection or instability. Revision rates of TSA are estimated at 10% after 10 years and 20% at 20 years.²⁷ Schoch et al.²⁹ report revision rates of 17% after 15 years. Higher revision rates are associated with male gender (perhaps due to higher loading of the joint), rotator cuff disease or tumors.^{27,30}

1.3.2 Reverse Shoulder Arthroplasty

In a reverse shoulder arthroplasty (RSA), the surgical preparation is similar to a TSA, the difference being the ball and socket are reversed. In an RSA, the ball (glenosphere) is fixed to the glenoid, and the proximal humerus is removed and replaced with a polyethylene cup, with an elongated shaft through the humeral canal (Figure 1.5). This results in a fixed joint center of rotation, and allows the deltoid to replace the function of a deficient rotator cuff. The indications for RSA include a prior failed TSA, deficient rotator cuff, arthritis, and fractures.^{31–33}



Figure 1.5: Reverse Shoulder Arthroplasty

Although the RSA has been used with success, and the prevalence of RSA is increasing dramatically,³⁴ it is not without complications.

The most common reported complication after an RSA is instability,^{32,35–41} with an incidence of dislocation in up to 15% of RSA's.³² Boileau et al.⁴² reported that nearly half of all revision RSA surgeries were due to instability of the joint.⁴² This may be due to inadequate deltoid tensioning, achieved through lateralizing the humeral component to increase the offset of the center of rotation.^{38,43} Another potential factor in instability following RSA is an irreparable subscapularis tendon. Edwards et al.³⁹ found the risk of post-operative dislocation to be almost twice as high in patients with an irreparable subscapularis tendon, compared to those with a repaired or intact tendon.³⁹ Gallo et al.³² also found that an abnormal subscapularis was present in all cases with post-operative dislocations as well as a compromised or absent greater tuberosity. However, Clark et al.⁴⁴ found no difference in rates of dislocation between patients with an intact subscapularis and patients without a repaired subscapularis and suggests the subscapularis does not have an effect on post-operative stability.

Surgical management of recurrent instability after an RSA is limited, especially in revision cases where glenoid bone quality is compromised.^{40,45} Chalmers et al. found that instability rates for revised RSA's were three times higher than in primary RSA cases.⁴⁰ A second revision surgery to manage chronic instability after an RSA was found successful in only 50% of cases,⁴⁰ indicating a need for a new solution to chronic instability.

Due to the configuration of a reverse shoulder implant, arm motion is limited in the allowable adduction range of motion. The inferior edge of the resected humerus may impinge on the glenosphere when the humerus is adducted, resulting in an adduction deficit. Because the CoR is medialized in an RSA, the humerus is displaced medially towards the glenoid. When this medialization is combined with the geometry of the glenosphere, the medialized humerus sits at the inferior edge of the glenosphere in adduction, resulting in impingement. With repeated impingement in adduction, the humeral cup wears away scapular bone directly inferior to the glenosphere.^{38,46,47} The ability to restore humeral adduction is important for patient comfort, as this is a frequently used position in activities of daily living.^{48,49}

In conjunction with the loss of adduction range of motion and damage to the scapula through scapular notching, a consistent and distinct wear pattern at the inferior aspect of the humeral cup is observed in retrieved components from unsuccessful RSA's.^{38,50} The wear pattern indicates high stress concentrations that may be a result of unfavorable loading conditions of this type of implant.^{50,51} This accelerated wear can lead to osteolysis, implant loosening, or premature component failure and the need for revision surgery.

A key clinical indication for a RSA procedure is a deficient rotator cuff. The reversed ball and socket configuration allows the deltoid to abduct the arm, a motion typically dependent on rotator cuff function. However, limitations on the range of motion are identified, with internal rotation affected by the size⁵² and positioning⁵³ of the glenosphere.

1.3.3 Constrained Shoulder Reconstruction

In the case of severe fracture or joint reconstruction following tumor resection, insufficient residual bone may be available to provide fixation for a traditional total or reverse shoulder

arthroplasty system. In this situation, more constrained shoulder prostheses are considered. Due to the infrequent use of these implants, they may be custom-made for a patient.

Bayley Walker Implant (Fixed Fulcrum)

This model is a constrained reverse ball and socket joint or fixed fulcrum design, meaning the socket encompasses more than half the sphere, similar to a traditional hip arthroplasty system. It is recommended for reconstruction of the shoulder joint for recurrent instability, revision joint arthroplasty, or following aggressive tumor resection in the joint.⁵⁴ However, this device has not been approved for use in the United States. It is worth noting that the ball is popped into the socket and then held in place with a retaining ring, which is the mechanism's weak link and point of expected failure with a load that exceeds the design load.⁵⁵ The available range of motion is still limited, at two-thirds of a normal range of motion.⁵⁴

Custom Scapula and constrained joint reconstruction

In the case of high-grade sarcoma in the glenohumeral area, more bone than just the joint surfaces must be replaced. A scapulectomy may be required, with some portion of the proximal humerus resected as well. Typical commercially available modular shoulder replacement systems do not provide for extended bone loss past the glenoid vault, or past the humeral neck. In these situations, a custom implant may be required. Past cases have documented the use of a frame reconstructed scapula with a constrained ball and socket joint in a limited number of patients.⁵⁶⁻⁵⁸ A hollow scapular frame with holes through the edges for muscular reattachment, combined with a locking ball joint has been used to restore some functionality to the arm. This system requires intact musculature to both hold the scapular prosthesis in place as well as to actuate humeral movement.⁵⁶

Although this system can aid in the preservation of rotator cuff, it does not provide ideal stability or sufficient range of motion to be considered fully successful. Long term viability is still unknown.

1.4 Revision Surgical Challenges

Although shoulder replacement is generally considered an effective treatment for end stage shoulder arthritis, severe fracture, and osteonecrosis, there are some unsuccessful cases where the implant must be removed and replaced (known as a revision). In the absence of complications, it is generally accepted that a joint replacement should last approximately 15 years before it may need replacement.^{27,59} This timeline may be accelerated due to infection, instability, loosening, or mechanical failure. Revision rates are estimated at 10% after 10 years and 20% at 20 years.²⁷ Higher revision rates associated with male gender (perhaps due to higher loads placed on the joint), and rotator cuff disease or tumors.^{27,30}

Due to a combination of low bone density, bone resorption and/or surgical damage to the bone while removing the previous implants, there may be a lack of available quality bone stock for good fixation of the new implant. Surgical damage often manifests itself as a large cavitory defect, and may be on either the humeral or glenoid side. It is often a consequence of revising a previous cemented implant; the bond of the cement mantle and implant is stronger than the surrounding bone, so that the bone itself fractures first and some is removed with the cemented implant.^{60,61} A contributing and related factor is bone resorption due to stress shielding by the previous implant. Because the metals used for implants are so much stiffer than the surrounding bone, the bone surrounding the implant no longer carries the load. This causes an imbalance in bone remodeling such that more bone is resorbed and new bone is not created.^{62–64}

A lack of available bone stock is not only an issue for ensuring adequate fixation of the implant to the bone, but it also suggests that some of the landmarks used for surgical navigation and landmarks may not be available. This leads to difficulty positioning the components in the absence of clinically relevant landmarks, such as the anatomic neck or humeral tuberosities. Scalise et al.⁶⁵ suggest that the implant may be positioned by referencing the distance from the lateral edge of the acromion to the glenoid margin.⁶⁵ Alternatively, several studies have found a correlation with the contralateral shoulder and suggest using it as a guide when anatomic landmarks are unavailable on the affected side.^{6,66–68}

A final challenge in revision surgery is the possibility that the rotator cuff or other soft tissues may not be intact. The rotator cuff, as the primary stabilizer of the joint, is a key structure for effecting anatomic motion. It may be damaged by the surgical incisions from a previous procedure,⁶⁹ damaged because of improper sizing of a prosthetic component, trauma induced injury, or disease. These soft tissue structures are needed for joint stability and ambulation of a ball and socket joint.

1.5 Development of a Linked Shoulder Implant

Universal joints (also known as Cardan joints, Hooke's joints, Spicer joints) allow rotational motion and torque to be transmitted between two shafts that are not co-linear. (Figure 1.6) While the universal joint is not a recent invention – the first record of its use was a variation based on gimbals by the ancient Greeks for the ballasts of ships – its modern form comprised of perpendicular pins and yokes are still in use today and are credited to Robert Hooke in 1667 for a sundial.⁷⁰ The most common modern application may be for automotive driveshafts, allowing torque to be transmitted to propel the vehicle, while also providing forgiveness for misaligned input and output shafts. In addition to its widespread use in automotive driveshafts, universal joints are also found in many industrial applications, hand tools, robotics, etc.

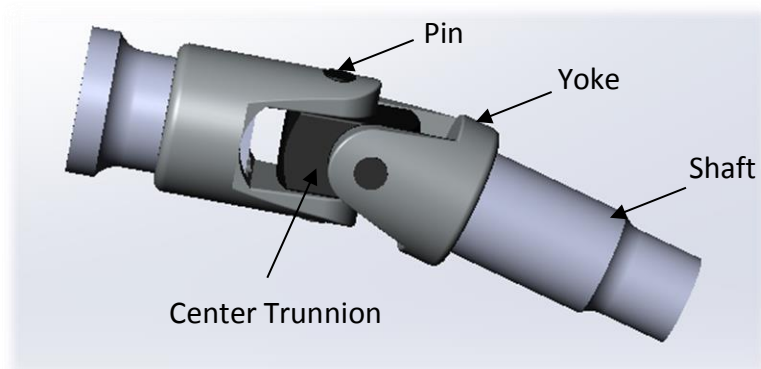


Figure 1.6: Torque transmitting universal joint (pin and block style)

Universal joints are rated based on the combined requirements of operating angle, maximum speed, and maximum torque. There is an inverse relationship between operating angle and allowable torque; a larger shaft misalignment lowers the allowable torque

transmission. A similar penalty-based relationship exists between the rated speed and the remaining factors. Commercial literature for universal joints allows for joint angles up to a maximum of 45° , with a torque transmission rating penalty that rises proportionally with the mismatch angle between input and output shafts. To increase the joint angle, a double universal joint can be used, with the understanding that rated torque capacity and shaft rotation speed must decrease by at least a factor of two. The driveshaft efficiency decreases as joint angle increases.

1.5.1 Design Objectives and Rationale for a Universal Joint Implant

The new design for a linked implant was modelled after a universal joint to replicate its large range of motion, along with its smoothness of motion for higher quality movement. Unlike the traditional application of universal joints to transmit torque between non-collinear shafts, the universal joint implant has a third revolute joint to allow internal and external rotation of the humerus. The introduction of this swivel also minimizes the torque on the glenoid fixation, which is identified as a potential failure mechanism.

Typical applications of universal joints include automotive driveshafts, where high speed, low torque and low joint angles are expected. In contrast, the application for a shoulder implant requires a universal joint to allow a large joint angle, with low speed, and minimal torque transmission. It must however, be capable of resisting both bending stress, contact stress, and fatigue.

The linked shoulder implant will be subjected to frequent bending stress, with the magnitude varying depending on the loading case. Thus, it is worth considering both the loading data generated from the instrumented traditional shoulder hemiarthroplasty as well as knowledge about the loading and contact patterns of hip implants. Metal on metal articulating surfaces are no longer used due to the complications associated with the wear particles generated from surface contact stresses. The wear particles generated can contribute to bone resorption and ultimately implant loosening as the encompassing bone degrades,⁷¹⁻⁷³ as well as allergic reactions to the metal ions released in the body.⁷⁴ With

the small size of components of a universal joint, the components would need to be made of a strong, stiff metal to withstand the loads placed on the joint.

Due to the sphere on sphere contact geometry of a ball and socket joint, by Hertzian contact theory, the theoretical contact area is an infinitely small point. However, in reality, there is some deformation whenever a load is applied, resulting in a patch of contact with some area. The same theory states that the theoretical contact pattern of two concentric cylinders would be a line, which in reality would turn into an ellipse as the surfaces deformed slightly under loads. This larger contact area distributes the force, thereby decreasing the contact stress at the surface. This reduces stress concentrations which in turn reduces the likelihood of developing scratches and premature excessive wear on the articulating surfaces of a pin and block style universal joint.

A second layer of protection against the negative effects of wear particles is encapsulating the implant linkage within a flexible silicon boot (or sleeve). This is a common technique for a universal joint driveshaft that operates in a dirty environment, and keeps dirt and grit out of the mechanism, and can be filled with lubricant to minimize friction between surfaces. In a medical implant application, the purpose of the sleeve would be to keep any wear particles within the boot, as well as keep the joint lubricated.

1.6 Thesis Rationale

Despite advances in joint arthroplasty components and surgical techniques, a small subset of patients continues to experience chronic subluxation and instability of the shoulder, impairing their ability to perform basic activities of daily life. Existing prostheses have limited ability to restore both stability and normal range of motion to the shoulder, especially in cases of severe stabilizing soft tissue deficit. A universal joint, by virtue of its linked components, cannot dislocate, and thus could provide intrinsic stability to the joint. It allows three rotational degrees of freedom, necessary to replicate the motion of the shoulder.

No linked universal type joints have been investigated for use in shoulder arthroplasty. It is unknown whether such an implant is capable of restoring normal range of motion, or the

ability of the implant and its fixation to withstand the expected loads of the shoulder. The purpose of this project is to design a novel linked implant for the shoulder that can achieve full range of motion while providing intrinsic stability to the joint. The feasibility of this implant design will be computationally evaluated with a basic parametric design, ahead of any experimental models.

1.7 Objectives and Hypotheses

The primary objective of this work was to develop a universal joint linkage as a shoulder prosthesis, and evaluate its feasibility and performance in context of the requirements for activities of daily living. The design requirements were based on healthy shoulders, with the goal of restoring normal function to a compromised joint. The joint's performance was assessed on three criteria, forming the pillars of this research project. The corresponding hypothesis directly follows each objective.

Objective 1:

Design a parametric linked shoulder implant. The implant design should include variable parameters to create an array of configurations that may be computationally tested in order to determine which configuration affords superior three-dimensional range of motion.

Hypothesis 1:

Normal range of motion can be achieved by some configuration of a universal joint linked implant.

Objective 2:

Determine the stresses experienced by the components of the designed linked implant in physiologically relevant joint loads using finite element analysis. These stresses are to be compared against static yielding and fatigue criteria.

Hypothesis 2:

The joint components will be capable of withstanding the expected stresses with a wide margin of safety.

Objective 3:

Evaluate the bone stresses experienced at the glenoid fixation interface by comparison of different implant configurations with variable lateralization distance of the center of rotation.

Hypothesis 3:

Bone fixation stresses will increase based on lateralization distance of the center of rotation, but stay within the allowable limits of bone strength.

1.8 Thesis Overview

Chapter 2 presents the development of the basic implant design and identifies the variable parameters of its configuration. After generating an array of implant configurations, the circumduction range of motion for each configuration was measured to determine the configuration that allows the greatest range of motion. After determining a basic configuration, Chapter 3 will confirm component design feasibility in terms of static yield and fatigue failure criteria. Chapter 4 will investigate relative bone failure risk due to the increased bending moment generated from this novel linked implant design. Finally, chapter 5 provides an overall summary and discussion of the findings of this research, and explores future work for further development of this implant

Chapter 2

2 Range of Motion of a Linked Shoulder Implant with Variable Configurations

OVERVIEW: Quantification of the allowable circumduction range of motion is an important metric to determine the success of restoring shoulder motion. A parametric implant model was created and several parameters (proximal yoke orientation, tilt, and location, offset distance of the two revolute joints of the implant) were varied for a total of twenty-four unique configurations. A standardized computational testing protocol was developed to test each of the implant configurations. A partial spherical surface that represents the allowable circumduction range of motion was developed to provide a visual representation for comparison of parameters to select the optimal configuration to maximize range of motion.

2.1 Development of a Universal Joint Shoulder Implant

To restore full motion in the glenohumeral joint, especially in the case of compromised bony anatomy or soft tissue, the joint mechanism must be inherently stable and constrained. Common universal joint designs were used as a starting point. Applications include automotive driveshafts or socket set drivers. While capable of transmitting high levels of torque, the joint angle is limited to 45° in any direction for a commercial universal joint. The geometry of the yokes lends additional strength to the joint, but at the expense of the range of available motion. Additionally, the geometry of the center trunnion plays a role in the range of motion; a flat cross provides less range of motion than an offset pin and block center trunnion. Each component of the universal joint shoulder implant is described in the following sections.

2.1.1 Universal Joint Components

Components for the proposed universal joint implant are illustrated in Figure 2.1 below. Detailed drawings of each component can be found in Appendix B.

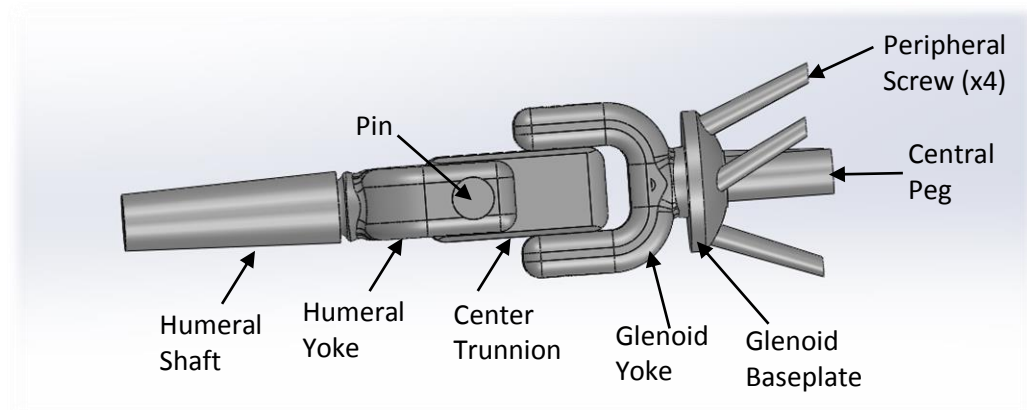


Figure 2.1: Components of proposed linked universal joint implant

Yokes

The yokes provide a frame to hold each pin, and form a hinge joint together with the center trunnion. The yokes must be strong enough to withstand bending stresses, but also sufficiently cantilevered to allow a large range of motion. There must also be a mechanism to connect the base of each yoke to its mated counterpart - ie. the glenoid baseplate and humeral shaft.

To accomplish the above requirements, yokes with a rectangular profile were used. The aspect ratio and radius were adjusted to allow clearance with the center trunnion at its maximum joint angle. A filleted rectangular cross-section was also used to prevent impingement with the center trunnion as it rotates through the axis at the base of the yoke.

Center Trunnion

The center trunnion articulates with the pins to allow two orthogonal rotational degrees of freedom, and withstands axial compression transmitted from the humeral yoke to the glenoid yoke. A pivot pin and block style was used for its high strength to size ratio.

The hinge joints of the trunnion were laterally offset to allow for clearance as the humeral component travels around the fixed glenoid component. A pin and block assembly was used, with the interface between the pins and block considered to act as journal bearings under compression.

Pins

Two identical pins were created to connect the center trunnion to each yoke. The tolerance was selected to be a press fit with the yoke hole, and a close running fit with the holes in the center trunnion. This will allow the ends of the hinge to remain constrained, and provide free, low friction articulation with the surface of the center trunnion.

Humeral Shaft

The humeral shaft was designed to fit around the base of the humeral yoke for a third rotational degree of freedom to replicate native internal and external rotation, as well as minimize the torque transmitted to the glenoid. An additional feature is its greater length compared to standard total and reverse shoulder arthroplasty systems' humeral stems. This will allow greater fixation in poorer quality bone, as is expected in revision surgery cases, or patients with low bone density.

Glenoid Baseplate

The universal joint trunnion must be fixed to the glenoid to provide a stable fulcrum for the joint motion. The success of the glenosphere fixation in reverse shoulder arthroplasty using a baseplate and bone screws has been studied as the use of RSA's have increased.^{61,75–}

⁷⁷ The lateralized abduction hinge of the universal joint implant is expected to show a similar loading pattern on the glenoid fixation to that of a lateralized offset glenosphere of a RSA. Therefore, the glenoid baseplate was modelled after the baseplate for a lateralized

offset RSA glenosphere (DJO RSP).²⁵ A circular baseplate was used with a domed back to closely fit against a reamed glenoid. The central screw is 6.5 mm diameter, and 25 mm in length, with 4 peripheral captured screws of the same length, but 4.5 mm in diameter.⁷⁶

An additional benefit of using an established design is in the case of revision surgery from a RSA to the proposed linked shoulder implant; if the existing glenoid baseplate is intact and well-fixed, it can be used with the linked implant system, minimizing the surgical damage to the patient and preserving glenoid bone quality.

Protector Sleeve for Implant

At the articulation of each joint, the resulting contact stress causes wear. Wear debris from metal and polyethylene components can cause complications in patients. It is associated with osteolysis, which may lead to pain and stiffness in the joint.^{38,63,73,78}

In typical mechanical applications for a universal joint in a driveshaft, the joint surfaces can be protected using a bellowed boot.^{79,80} This protective boot both preserves lubrication on the articulating surfaces and prevents dirt and grit from entering the joint and contributing to early wear acting as third body particles.

Replicating this concept with a biocompatible silicone boot can prevent any metal debris from escaping into the body, preventing adverse reactions as well as providing the opportunity to use materials typically excluded from consideration due to bio-incompatibility or bio-reactivity. A final benefit is the ability to keep lubrication in the joint to reduce friction and therefore also reduce wear.^{81,82}

This thesis describes the design of a linked implant which is intended to be used in conjunction with a protective boot. While the design of the boot itself is outside the scope of this thesis, it is important to ensure that appropriate materials exist for this application and are currently used for a variety of medical implant applications. Examples include materials such as Elasthane,⁸³ CarboSil,⁸⁴ and BioNate,⁸⁵ with documented use as an insulative encapsulation for neuro-electrical stimulator implants, which would otherwise be toxic to the body. Additionally, tough, flexible materials (ie.- CarboSil,⁸⁴ BioSpan,⁸⁶ or BioNate⁸⁵) with a high fatigue life are currently used for implants that flex continuously in

use, such as artificial heart pumps and valves. These materials are demonstrated to be biocompatible and bio-inert, safe for use as long-term implanted medical devices. Therefore, the design of the implant itself proceeds with the knowledge that appropriate booting materials and technology exists. The design of the boot is considered future work after evaluating the feasibility of a linked shoulder implant.

2.2 Development of Virtual Prototype

Several iterations of a universal joint were made in 3D CAD software (SolidWorks 2017, Dassault Systems, France) with varying geometries: a Y-yoke joint with a crossed center trunnion (Figure 2.2), a square yoke with a flat trunnion, and a square yoke with an offset center trunnion. The square yoke with an offset center trunnion provided the greatest range of motion. The next step was to adjust the dimensions such that the center trunnion was free to swivel about both pins without impinging on the base of the yokes. This involved longer yokes than typically seen in driveshaft torque transmitting designs to allow a larger rotational range of motion around each pin. While this would be a concern for the additional torsional stress on the yokes in a driveshaft application, since there is a third revolute joint on the humeral shaft, there is minimal torque transmitted through the joint. One caveat to the square yoked design with an offset center trunnion is that the joint is not capable of moving in a continual hemispherical motion; at the equator of motion, the joint must retract to pass the yoke at a lesser angle before it can swing out again.

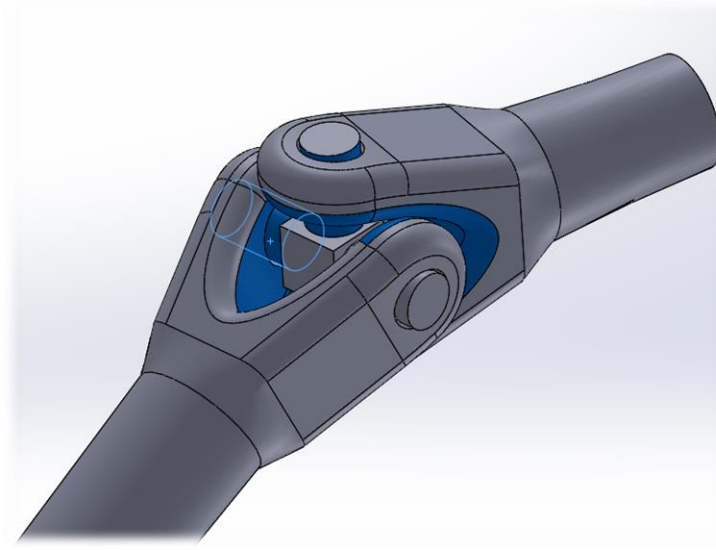


Figure 2.2: Y-yoke universal joint

*Range of motion limited by impingement between proximal and distal yokes.
(Impingement shown in blue highlighted faces).*

The third revolute joint is added to provide the arm with internal/external rotation and minimize torque transmitted to the glenoid. This could be located on either the proximal or distal side of the trunnion. The revolute joint was incorporated into the humeral shaft for more intuitive user motion, as it would replicate natural humeral internal/external rotation more closely. Additionally, the longer shaft to fix the humerus in place lends itself seamlessly to a sleeved revolute joint.

With a basic linkage model created, it could be virtually implanted into a bone model. Different parameters in linkage geometry as well as the implantation technique could be varied to sift out the combination that affords the greatest range of motion.

2.3 Virtual Implantation of Universal Joint Implant into Bony Geometry

A full-arm bone model was created from the bone density threshold of a CT scan of a cadaveric scapula and humerus. The donor was an 85 year old male (height: 165 cm, weight: 67 kg). The bones were segmented using a semi-automatic algorithm (Mimics v17.0, Materialise, Belgium). The arm was placed in a neutral, adducted position (30°

between the transepicondylar axis and the scapular plane).⁸⁷ Reference geometry was created to provide consistent landmarks for positioning the implant. Points were placed along the glenoid rim, and a best fit plane was created from the points using a least squares algorithm. This will be referred to as the glenoid plane. Bisectors connecting the superior and inferior points of the glenoid rim, and anterior-posterior were created to form the center point of the glenoid dish. With this reference geometry in place, the glenoid yoke could be positioned appropriately. The center of the glenoid yoke was coincident with the center of the glenoid face, and the edges of the yokes could be set parallel or perpendicular to the superoinferior bisector to control the glenoid yoke orientation. (Figure 2.3)



Figure 2.3: Positioning of the glenoid baseplate

The antero-posterior and supero-inferior bisectors of the glenoid are shown as black lines. The intersection of these bisectors represents the center of the glenoid face. The glenoid baseplate shown is lowered 5 mm from the center of the glenoid face (blue line).

The humeral head resection plane was placed by an experienced fellowship trained shoulder surgeon (GSA), based on surgical landmarks of the anatomic neck. The virtual osteotomy was performed aggressively – the osteotomy plane was translated 5 mm more distal than for a traditional shoulder arthroplasty. This had a noticeable effect on the range of motion, since the humeral yoke is inset into the humeral head. A traditional osteotomy

plane restricted internal and external rotation, and caused earlier impingement with the superior portion of the humeral head with the glenoid yoke at less than 90° of abduction relative to the glenoid face. Only the cortical bone was considered, such that the humeral yoke was set in a hollow humeral head, resembling a large contained cavitory defect, a common occurrence in revision surgery.⁶⁰

The native shoulder has a center of rotation that can be calculated from the landmarks of the humerus and glenoid fossa.⁸⁸ Custom code (Matlab 2016a, MathWorks, Massachusetts) was used to extract the center of the best fit sphere of the humeral head, which approximated by the geometric center of rotation.⁸⁹ The linked implant was initially positioned such that the center of mass of the 6 mm offset center trunnion (midpoint between pins) was coincident with the geometric center of rotation of the native humeral head. For the default orientation, the medial face of the glenoid yoke was mated parallel and coincident to the glenoid plane.

For parameter variation, the tilt of the glenoid component was adjusted using specified angular relationships between the medial face of the glenoid yoke and the glenoid plane. The location of the lowered glenoid component was set so its center was 5 mm inferior to the center of the glenoid face.⁹⁰

The humeral stem was aligned with the center of the canal circle fit for the proximal third of the humerus to replicate current surgical techniques.^{23,24,91}

2.4 Parameter Variations

First, the parameters to be varied were identified, along with their levels of variations. Variation was set at discrete increments since kinematic functions have not been developed for an offset center trunnion universal joint. The goal of the implant is to maximize the available range of motion, while still ensuring its mechanical integrity and preventing dislocation of the joint. Common surgical practices for the implantation of RSA, a semi-constrained prosthesis, suggest the lateralization offset of the CoR, tilt of the glenoid component, and position of the glenoid all contribute to the available ROM and the development of scapular notching.³⁵

The parameters to be varied were:

- Glenoid Yoke Orientation
- Glenoid Yoke Position
- Glenoid Yoke Tilt
- Offset Distance of Center Trunnion

As described in the following sections.

Glenoid Yoke Orientation

The arms of the glenoid yoke were oriented to be either horizontal or vertical relative to the face of the glenoid (Figure 2.4). This may influence the lever arm of the deltoid muscle; as the location of the horizontal pin joint moves more distal/lateral, the deltoid moment arm will be shortened, resulting in a higher required muscle force to abduct the arm. Medializing the horizontal pin joint may lengthen the lever arm for the deltoid, making the deltoid more effective in abducting the arm. This could be evaluated by muscle force balance analysis. However, muscle contributions and force analysis are outside the scope of this project.

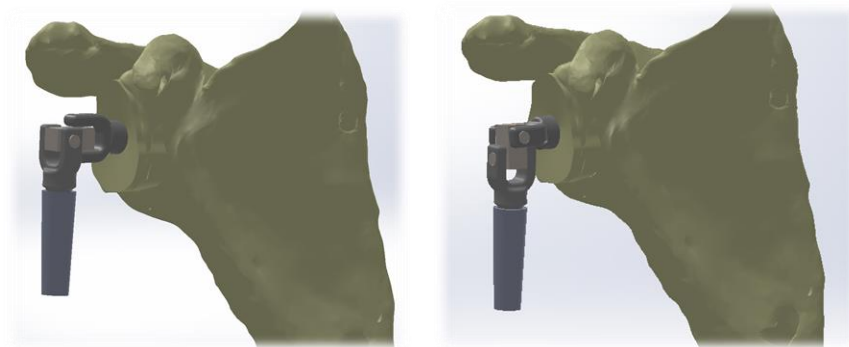


Figure 2.4: Glenoid yoke orientation variation

Left: Vertically oriented glenoid yoke (VG). Right: Horizontally oriented glenoid yoke (HG). Both are centered in the glenoid face.

Glenoid Yoke Position

The glenoid yoke was located either in the center of the glenoid face, determined by the intersection of the anteroposterior and superoinferior bisectors, or lowered 5 mm from the center (Figure 2.5). A common surgical technique in a reverse shoulder arthroplasty is to position the glenosphere so that it is tangent to the inferior portion of the glenoid. This provides two key benefits – it helps avoid scapular impingement and puts additional tension on the deltoid to give it a mechanical advantage as it is replacing the function of the rotator cuff.^{38,43,53} Ladermann et al found that lengthening the humerus tended to result in a more stable shoulder.⁴³

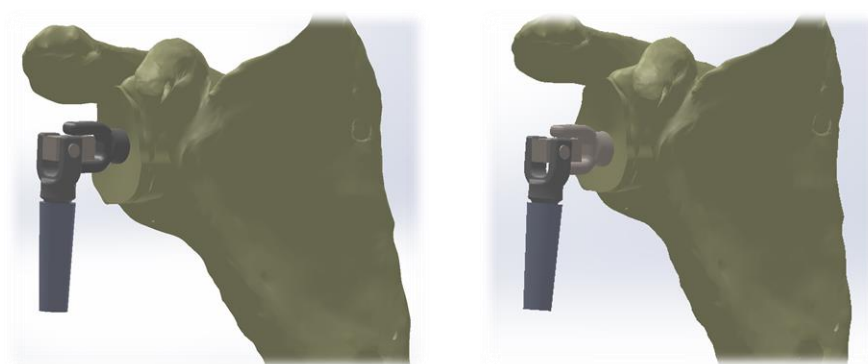


Figure 2.5: Glenoid yoke position variation

Left: Proximal glenoid yoke centered (C) in the glenoid face. Right: Proximal glenoid yoke lowered (L) 5 mm from the center of the glenoid face. Both are depicted with the vertically oriented glenoid yoke in neutral tilt.

Glenoid Yoke Tilt

The tilt of the glenosphere is another variation currently under investigation for the reverse shoulder arthroplasty technique. It is thought that an inferior tilt helps maximize available range of motion by preventing scapular notching. An additional benefit is additional deltoid lengthening, which increases the lever arm of the deltoid, providing a mechanical advantage to the muscle.^{38,43} As such, three different tilts were investigated with the linked shoulder implant: neutral, 10° inferior, and 20° inferior (Figure 2.6). A superior tilt was not used – preliminary testing (performed using the protocol described in 2.3) showed that a superior tilt increased the incidence of scapular impingement, so it was not pursued further.



Figure 2.6: Glenoid yoke tilt variation

Left: Neutral (N) tilt of glenoid yoke. Middle: Glenoid yoke tilted inferiorly by 10° (10D). Right: Glenoid yoke tilted inferiorly by 20° (20D). All three share a vertically oriented, centered glenoid yoke (VG_C).

Offset Distance of Center Trunnion

Varying the offset distance of the center trunnion displaces the centers of rotation of the two joints created by the linked universal joint design. While a larger offset distance between the two joint centers may achieve a larger range of motion, the moment arm for the deltoid should be considered. Additionally, lateralization of the humerus in reverse shoulder arthroplasty designs may contribute to lowering joint and muscle loads, as well as decreasing the incidence and severity of scapular impingement.⁵²



Figure 2.7: Offset distance of hinge joints in center trunnion variation

Left: 6 mm offset between center and hinges in the center trunnion (C6). Right: 8 mm offset between center and hinges in the center trunnion (C8). Both share a vertically oriented, centered, neutral tilted glenoid yoke. (VG_C_N)

An additional consideration is that the patient may encounter some proprioceptive changes because of the joint's non-anatomical geometry. In changing from a ball and socket joint configuration to a universal joint configuration, there may be discomfort in the user's perception of the dual center of motion, and that coincident supplementary motions are now required to achieve the intended motion. (The user must reposition the implant around the yokes by backing off and then reaching back out again). However, clinical testing of this implant is outside the scope of this thesis, and requires FDA approval so any changes in proprioception due to the dual centers of rotation will not be known until clinical trials.

To investigate the effects of the offset distance of joints on range of motion, two different offset distances were used. We tested offset distances from the center of the center trunnion

to the center of the pin of 6 mm and 8 mm (Figure 2.7). The 8 mm offset distance would result in a net lengthening of the humerus by 4 mm compared to the 6 mm offset, and provide an extended reach around the yokes.

2.5 Range of Motion Testing Protocol

With four parameters identified to be varied per their respective levels, range of motion testing could be performed.

The humerus was manually moved to the extremes of motion for the full circumduction range,^{92,93} using the collision detection function (SolidWorks). We checked for impingement in both bone-on-bone contact and bone-on-implant contact. Once a collision was detected, the joint was moved back slightly to a position with no impingement and the position of the midpoint of the transepicondylar axis was recorded. The humerus was axially rotated to an orientation that would minimize bony impingement and allow a larger joint angle, by retracting the superior portion of the humeral head to the side. A template was overlaid to the scapula on each model to ensure consistency in the rotational spacing of the humerus. (Figure 2.8) The template had thirty spokes, so that when the transepicondylar midpoint was aligned with each spoke, each position recorded was approximately 12° apart.

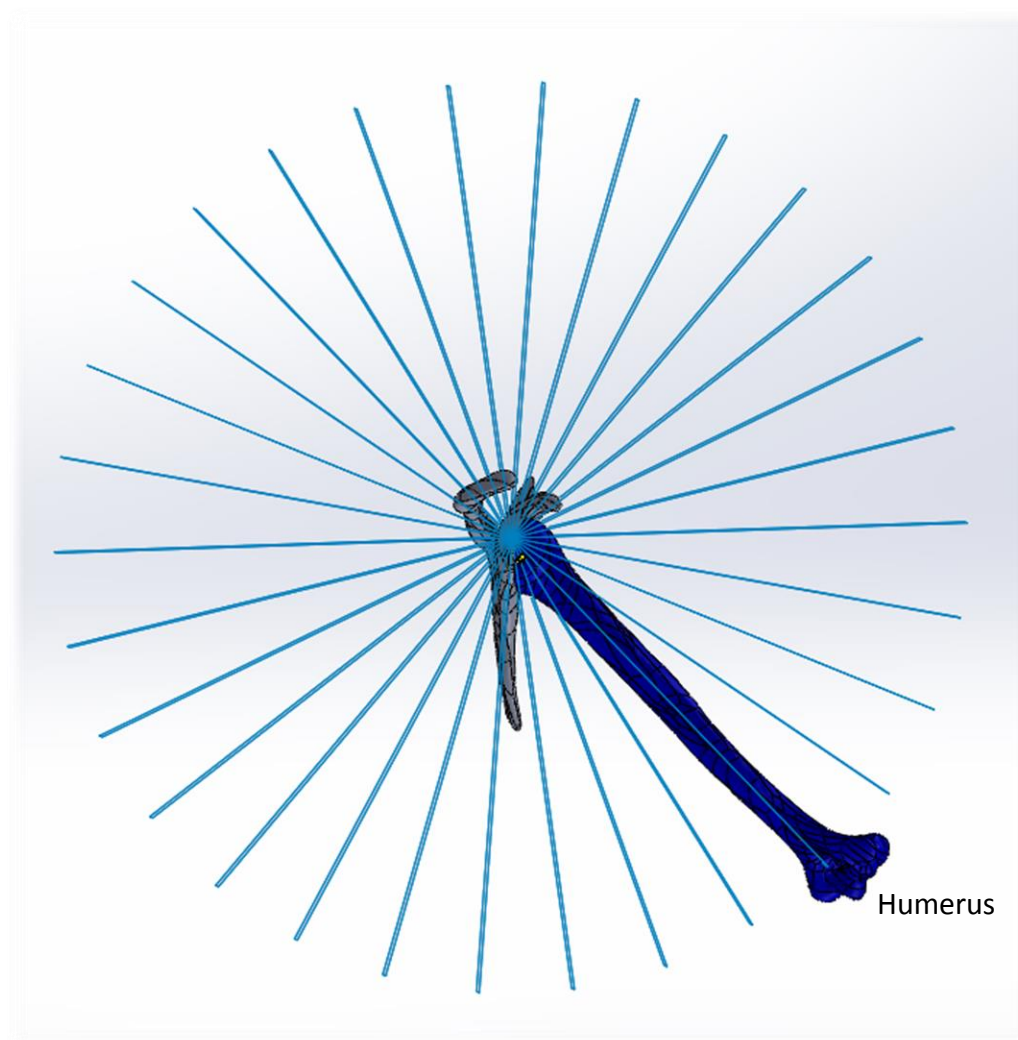


Figure 2.8: Range of motion template

View is orthogonal to the glenoid face. Humerus is shown aligned with one of the spokes of the range of motion template. Once the humerus was aligned with a spoke, it was then rotated toward the glenoid until impingement was detected.

Once all circumduction range of motion points had been plotted, a surface was created, bounded by the lines connecting each placed circumduction point and the geometric center of rotation of the native humeral head. Knitting each of these surfaces together resulted in a 3D boundary of motion, which was then used as a cutting tool to cut out the available boundary out of a sphere to depict the allowable range of motion for each implant configuration (Figure 2.9). The boundaries of motion are recorded, without concern of the contributing kinematics. Humeral rotation is incorporated into the measurements, rather than reported separately.

These partial spheres were then overlaid on top of each other and the assembly to determine which configurations provided the most range of motion. This setup also allowed direct comparison of which configurations allowed the greatest joint angles in specific movements. For example, determination of which configuration allows the greatest adduction before impingement is quick and obvious.

This protocol was first done for all configurations on a medium specimen which also had average head-neck and retroversion angles.^{94,95} Sizing of cadaveric specimens was determined based on humeral length. (Donor information given in Table 2.1) Based on the results of the full study, this protocol was repeated for six specific configurations in both a small specimen and a large specimen to elucidate the range of motion of the universal joint linkage itself, rather than the effects of differing bone morphology of a single specimen. These additional specimens incorporated a wider humeral retroversion angle range.

Table 2.1: Anthropometric data of specimens used for range of motion testing

Specimen	Specimen ID	Sex	Weight (kg)	Height (cm)	Humeral Length (cm)	Age (years)	Head-Neck Angle (°)	Version Angle ¹ (°)
Small	09-05059R	F	60	157	280	66	129	42
Medium	14-07032R	M	67	165	320	85	137	35
Large	11-01002R	M	101	178	345	58	137	11

¹ Humeral version angle is measured referencing the distal epicondylar axis.

The six configurations used for repeated range of motion assessment in the additional two bone models were selected based on their overall range of motion, with a bias toward the adduction and forward elevation movements. The configurations with the 5 largest ranges of motion were selected, as well as the configuration with minimal range of motion to ensure that this was not simply an effect of the bone specimen but of the linkage configuration.

2.6 Range of Motion Results

The work envelopes representing each configuration's allowable range of motion were all plotted on the same model to visually evaluate the largest range of motion. Knowing that most time is spent with the humerus either adducted or in low forward elevation,⁴⁸ a sufficient range of motion in these quadrants was essential for configuration selection.

The larger offset distance between centers of rotation of the trunnion block resulted in larger ranges of motion compared to the same configurations with the smaller offset distance. The same observation was made with the 20° inferior tilt, although this was associated with a smaller effect on range of motion.

The orientation of the glenoid yoke made a difference in the location of the maximum range of motion. The vertical glenoid yoke had better adduction, while the horizontal glenoid yoke had more forward and backward elevation in the pilot study with one specimen. Interestingly, the most forward elevation occurred with a vertical, lowered glenoid yoke, tilted 20° inferior, and an 8 mm center offset distance. The most adduction was found with the same variables, except a horizontal glenoid yoke instead of vertical. Interestingly, these maximum joint angles correspond to the rotation axis of the proximal pin.

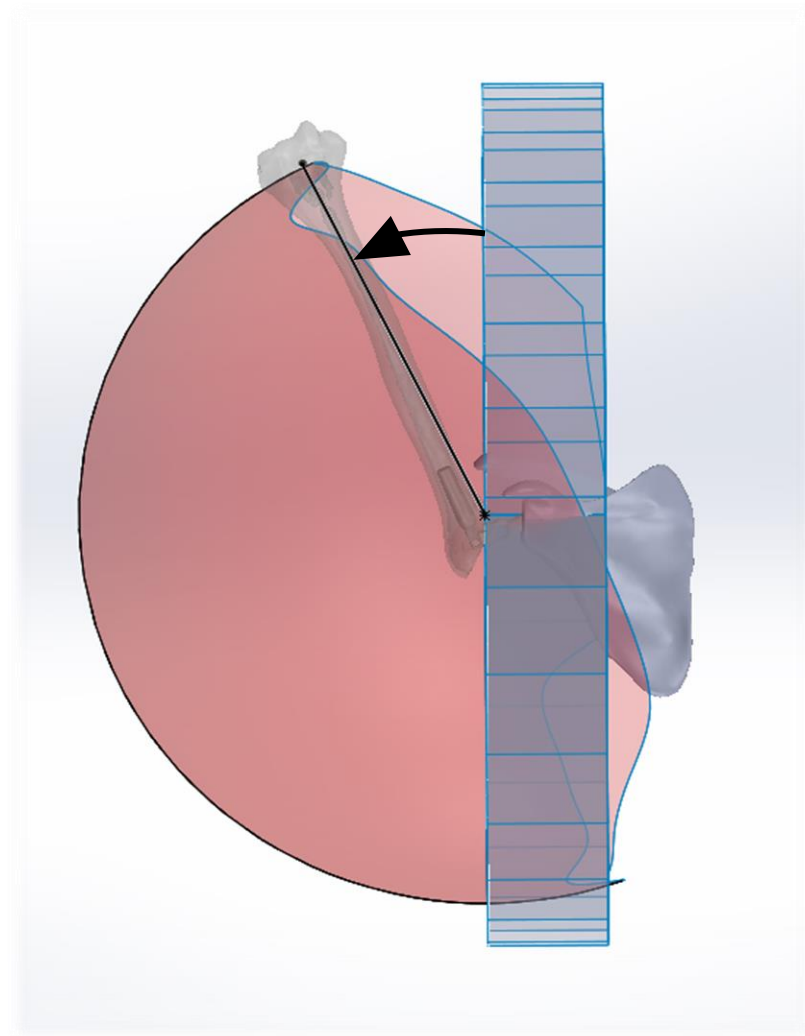


Figure 2.9: Joint angle measurement

Joint angle (black radial arrow) is measured between the plane of the glenoid and the humeral axis.

The reported output measure represents the joint angle between the humeral shaft axis and the glenoid plane (illustrated in Figure 2.9). Angles were measured from the best fit plane (Matlab, 2016) of the glenoid rim for each of the 24 configurations tested in the medium specimen and presented in Table 2.2. Both abduction and maximum forward elevation result in the humerus raised superiorly as far as possible. The distinguishing features between these movements are the humeral rotation and the plane in which the motion occurs. Because this protocol evaluates the circumduction profile, the motion is not constrained to a 2D arc within a set plane, as is commonly done in range of motion assessments. Additionally, the measurement refers to the end position of the midpoint of the transepicondylar axis, which integrates the axial humeral rotation, rather than having axial rotation reported as a separate motion. Therefore, the most superior points are not separated into abduction or forward elevation, but are instead referred to as “superior elevation”.

These values were measured at the location that provided the maximum angle, rather than measuring the angle at an identical node across all configurations. This is more relevant to physiological measures of patient’s ability to reach range of motion targets that are loosely constrained in terms of the arm trajectory to reach the maximum range of motion. However, there are some configurations that are more consistent (showing a smoother profile) than others with more variable profiles, with configurations smoother profile given preference for further analysis.

Table 2.2: Maximum range of motion for 24 configurations in medium specimen

Configuration	Adduction (°)	Superior Elevation (°)	Cross arm angle at 90° Forward Elevation (°)	Cross arm angle at 90° Posterior Elevation (°)
VG_L_20D_C6	-18.06	12.37	-8.39	1.63
VG_L_20D_C8	-18.55	15.84	-14.90	-8.80
VG_L_10D_C6	-4.51	9.33	0.34	0.54
VG_L_10D_C8	-11.86	11.70	-15.70	-12.52
VG_L_N_C6	-4.76	2.08	0.47	2.33
VG_L_N_C8	1.29	8.32	-7.56	-11.70
VG_C_20D_C6	-18.03	19.74	4.03	1.16
VG_C_20D_C8	-17.73	18.23	-4.78	-12.47
VG_C_10D_C6	-11.52	9.98	2.72	2.02
VG_C_10D_C8	-6.34	5.71	-10.86	-11.36
VG_C_N_C6	1.77	2.68	7.57	4.58
VG_C_N_C8	3.2	4.83	6.59	-12.22
HG_L_20D_C6	-11.74	11.25	3.59	2.29
HG_L_20D_C8	-19.26	23.22	1.08	2.07
HG_L_10D_C6	3.34	14.10	-8.43	9.20
HG_L_10D_C8	-14.11	18.05	0.46	1.77
HG_L_N_C6	0.80	16.16	0.27	1.29
HG_L_N_C8	-10.17	18.55	1.27	1.84
HG_C_20D_C6	3.57	15.80	1.76	0.90
HG_C_20D_C8	-10.06	21.69	0.22	1.67
HG_C_10D_C6	3.58	23.55	0.63	0.91
HG_C_10D_C8	-5.69	24.68	0.54	2.42
HG_C_N_C6	10.27	12.09	3.94	1.81
HG_C_N_C8	0.29	27.32	5.31	0.74

Highlighted configurations are tested in two additional specimens with the results described in more detail in Section 2.7. Angles have been translated to reference the physiological planes of the body, consistent with common clinical practice.

*Naming convention is as follows: **Glenoid Yoke Orientation** (VG or HG)_**Glenoid Yoke Position** (C or L)_**Glenoid Yoke Tilt** (N or 10D or 20D)_**Offset distance of Center Trunnion** (C6 or C8)*

The overall largest range of motion can only be fairly evaluated if looking at the full circumduction profile because of the uneven profiles in some cases. Thus, the five configurations with the largest overall circumduction range of motion profiles were visually identified and chosen. These configurations were also virtually implanted into both a small specimen and a large specimen bone model for range of motion testing. Additionally, the smallest range of motion profile was tested in the small and large specimen to verify that it was the implant configuration that most limited the range of motion rather than individual bony morphology differences.

For the overall circumduction range of motion, it was found that a vertical glenoid yoke, lowered 5 mm from the center of the glenoid face, tilted 20° inferiorly, with an 8 mm offset between hinges in the center trunnion provided the greatest range of motion (labelled configuration 1). This result was consistent across all three sizes of bony models.

The results from each of the six common configurations can be found in the figures below, one with the full circumduction range of motion, and each subsequent figure isolating one distinct motion at a time. The angles were measured with respect to the best fit plane of the glenoid rim for each specimen. A negative angle implies that the humerus extends past the equator of a sphere centered on the face of the glenoid, towards the medial plane of the body. Thus, the smaller the sum of each of the thirty angles is, the larger the overall range of motion is. Points were measured starting at the most superior point, and travelling clockwise around the circle. Thus, points 28 through 5 are superior elevation, points 6 through 12 are forward elevation, points 13 through 20 correspond to abduction, and points 20 through 27 are posterior elevation. (Figure 2.10)

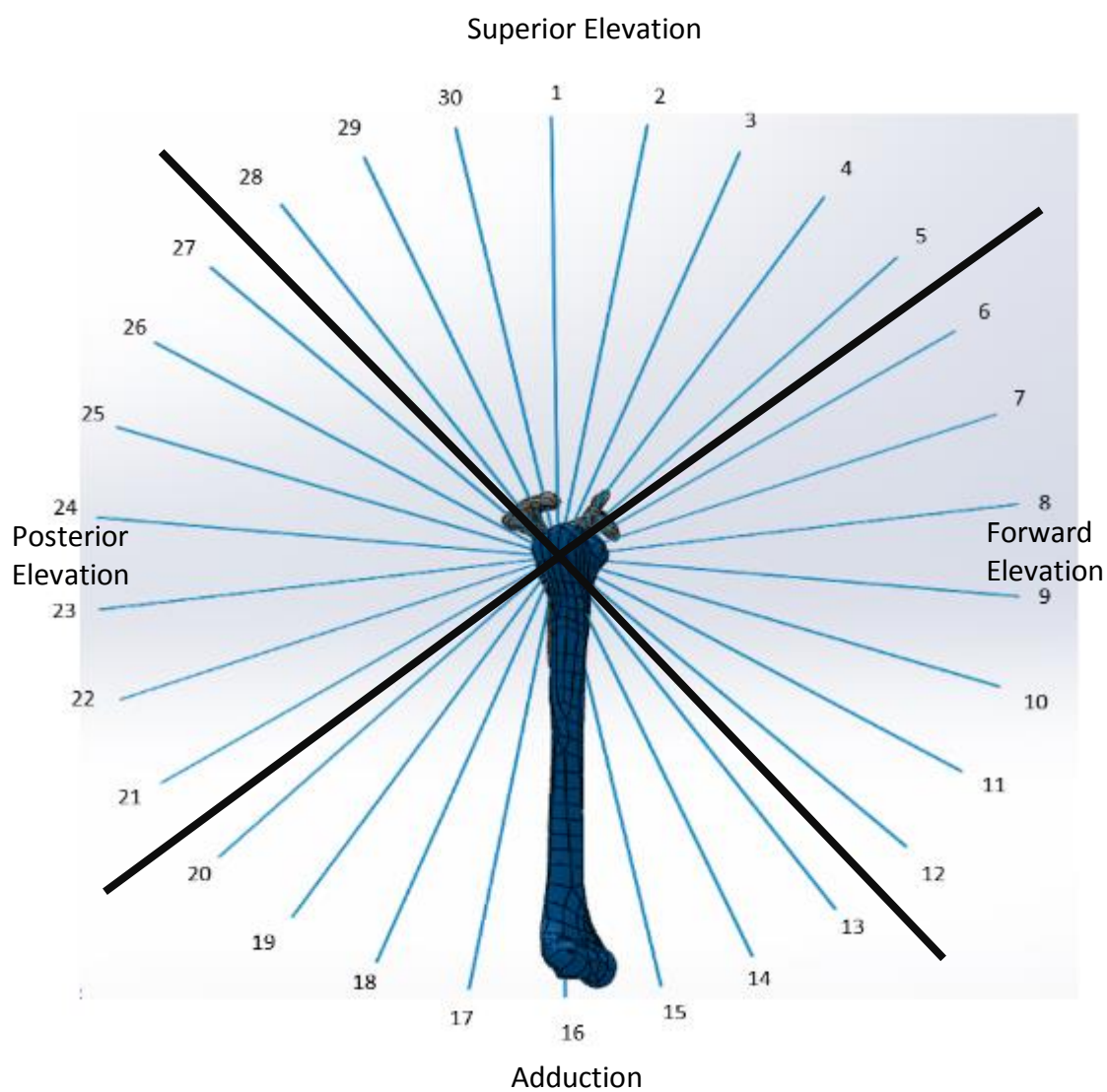


Figure 2.10: Numbered spokes on the template to divide range of motion measurements into separated movements

Based on the functional requirements of daily living, the most important motions are adduction and low angles of forward elevation. Langohr et al.⁴⁸ reported on the frequency of arm motions using an instrumented shirt to track the daily arm motions of both healthy participants and patients with joint implants. Arm motions were stratified at 20° increments. It was found that 88% of all motions in a day were below 80°. Coley et al.⁴⁹ also recorded arm movement of healthy volunteers and found similar results, with 99% of arm motions occurring at or below 90° of humeral excursion, and almost 90% of arm motions recorded were under 50°.

2.7 Statistical Analysis of Range of Motion Results

Full Circumduction Profile

A 2 way repeated measures ANOVA was performed on the measured angle between the humeral axis (the vector originating at the CoR and ending at the recorded point of the epicondylar midpoint) and the plane of the glenoid. The location of measurement (points 1-30) and the configuration were set as the within subject factors, with n=3 (representing the small, medium, and large specimens).

The tests of within subjects effects indicate that both the configuration ($p=0.011$) and the location of measurement ($p=0.041$) have an effect on the range of motion, and that there is no interaction ($p=0.165$) between the configuration and measurement location. As shown in Figure 2.11, the general profile of the humeral angle follows a “U shape”. During superior elevation, the humeral range of motion is limited by the excursions of the coracoid and acromion processes past the glenoid plane. Thus, we expect to see the humerus impinge at a lesser joint angle than at lower elevations where the coracoid and acromion do not affect the ROM, and this is precisely what the shape of the graph confirms. The steep slopes of the graph indicate that once the humerus moves past the coracoid and acromion, the joint is able to achieve a larger range of motion, and maintains a large joint angle through the rest of the circumduction movement.

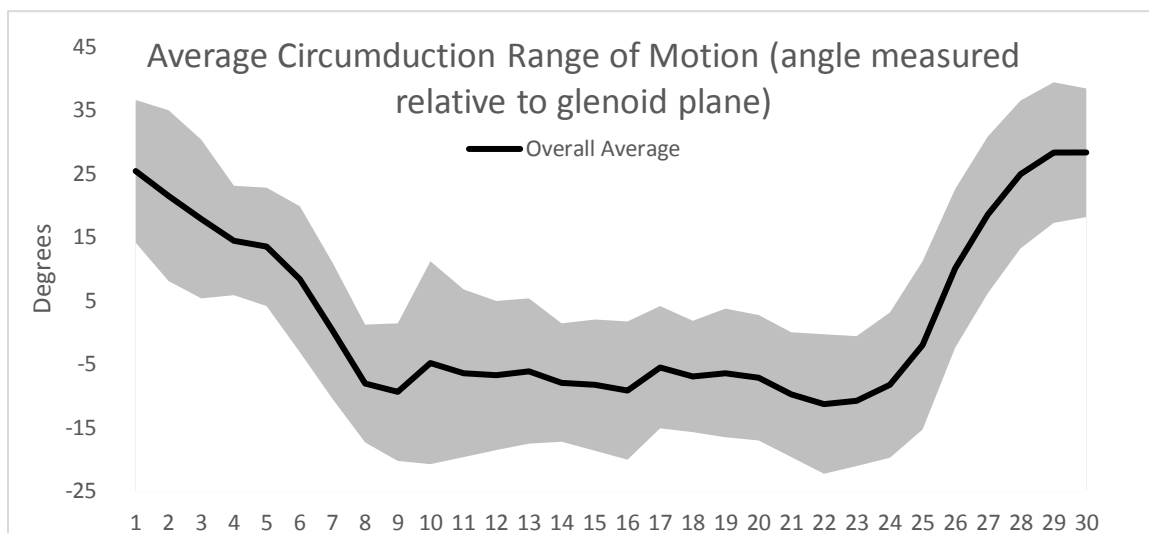


Figure 2.11: Overall mean circumduction range of motion

Angle is average between all 6 configurations tested and three sizes of specimens. Black line represents mean joint angle, with the shaded grey band depicting one standard deviation on either side of the mean value. Individual plots separated by configuration are presented in Appendix C.

Configuration was also found to have a significant effect. But its effect is less obvious since it is divided categorically rather than as a scale input variable. Additionally, there are unequal samples of each varied parameter level within the six configurations chosen for further study, which makes elucidating the effects of each variable more difficult. This is identified as a limitation, and an area of further study in the future after the feasibility of the implant has been studied.

The fact that there is no interaction between location and configuration supports the conclusion that the range of motion measured is a function of the implant configuration and the location of measurement. This result also indicates that individual differences in the bony anatomy of the three specimens were not enough to alter the measured range of motion in a significant way.

Once the overall effects were determined, a one-way repeated measures ANOVA with Bonferroni correction was performed with pooled measurements for all three specimens investigate significant differences in pairwise comparisons. Configuration was set as the within-subjects factor, with six levels, set to each of the six configurations.

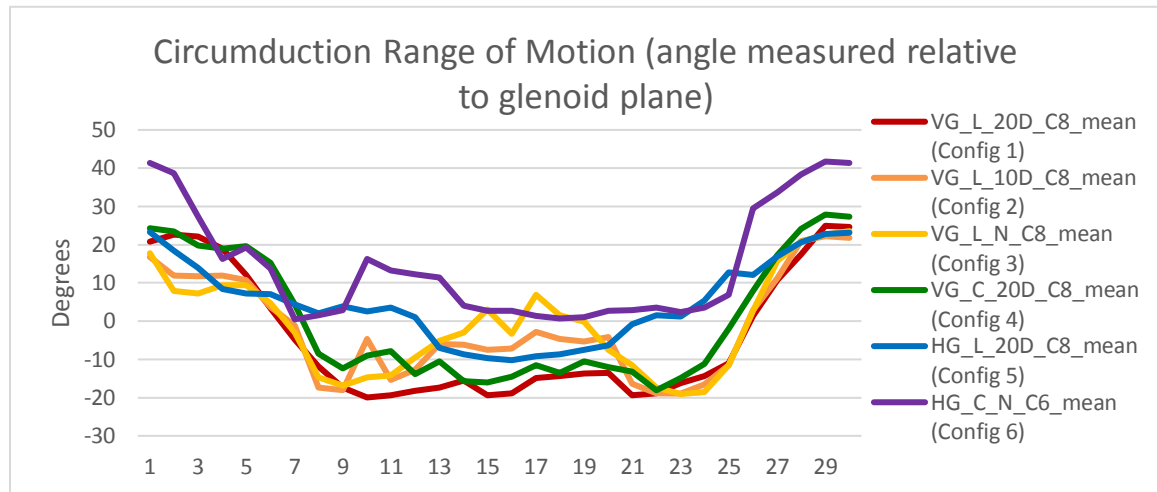


Figure 2.12: Comparison of mean circumduction range of motion angles between 6 configurations

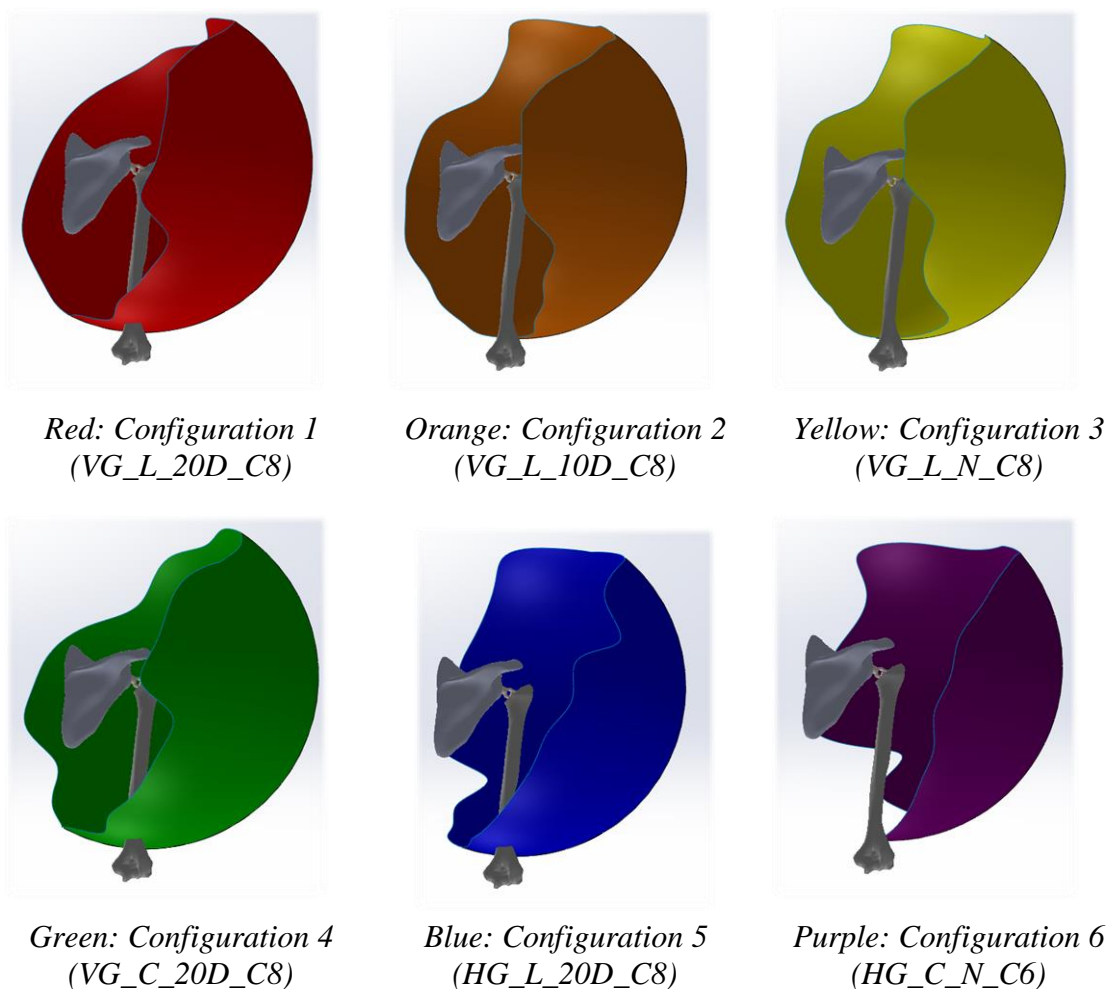


Figure 2.13: Individual range of motion spheres for 6 configurations

Posterior view of scapula, with humerus in a neutral, adducted position. The boundary of the coloured spheres represents the allowable 3D range of motion of the humerus. These illustrations correspond to the measured angles presented in Figure 2.12 above.

The humerus is shown in a neutral, adducted position for all implant configurations. Adduction is impaired in configurations 2, 3, and 6, shown by the intersection of the distal humerus and the RoM sphere.

Mauchly's test of sphericity indicated the assumption of sphericity was violated, ($\chi^2=117.22$, $p<0.0005$). Thus, Greenhouse-Geisser corrections were used. Configuration was found to have a significant effect on the angular range of motion ($p=0.016$). The means, standard deviation, and upper and lower bounds of the 95% confidence interval were plotted for each of the six configurations, with pooled results from all three specimens, shown in Figure 2.14.

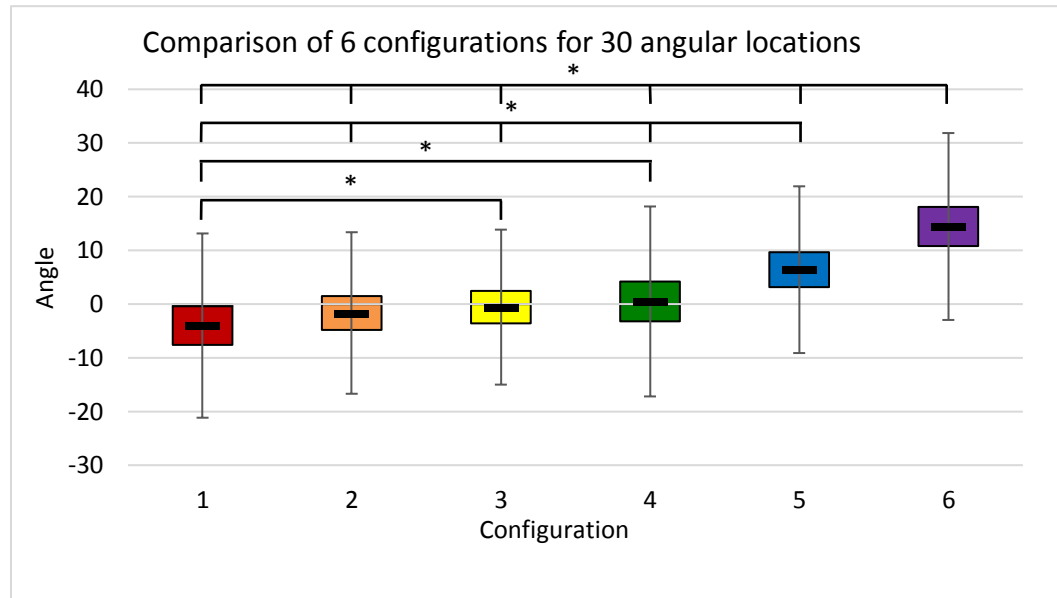


Figure 2.14: Comparison of 6 configurations across all 30 angular locations

Boxes represent the upper and lower bounds of the 95% confidence interval, with the thick black bar depicting the average value of all angular locations and specimens. Asterisks indicate a significant difference between mean ranges of motion. ($p<0.05$).

Pairwise comparisons between each configuration are summarized in Table 2.3 below. The significance level was set at $p<0.05$, and significant differences are highlighted in green.

Table 2.3: Pairwise comparisons for mean differences between configurations

	Config 1	Config 2	Config 3	Config 4	Config 5	Config 6
Config 1						
Config 2	-2.35 p=0.24					
Config 3	-3.44 p=0.023	-1.09 p=1.000				
Config 4	-4.50 p<0.005	-2.51 p=0.579	-1.06 p=1.000			
Config 5	-10.41 p<0.0005	-8.067 p<0.0005	-6.98 p<0.0005	-5.91 p<0.0005		
Config 6	-18.45 p<0.0005	-16.11 p<0.0005	-15.02 p<0.0005	-13.96 p<0.0005	-8.04 p<0.0005	

The ranges of motion of configurations 5 and 6 (both are versions of a horizontal glenoid yoke) were significantly smaller than the four other configurations which all share a vertical glenoid yoke. Configuration 1 had a superior range of motion to all other configurations except for configuration 2, with the only difference between these configurations being the level of tilt in the glenoid yoke.

The overall range of motion can be further separated based on the location of the humerus into four physiologically relevant zones representing adduction, forward elevation, superior elevation, and posterior range of motion. With pooled data from the three specimens, the following results were found.

Adduction Range of Motion

In adduction (points 13-20), configuration was found to have a significant effect on range of motion ($p<0.0005$). Configurations 1, 4, and 5 have the most allowable range of motion in adduction. (Figure 2.15) These configurations all share the 20° inferior tilt and the longer center trunnion.

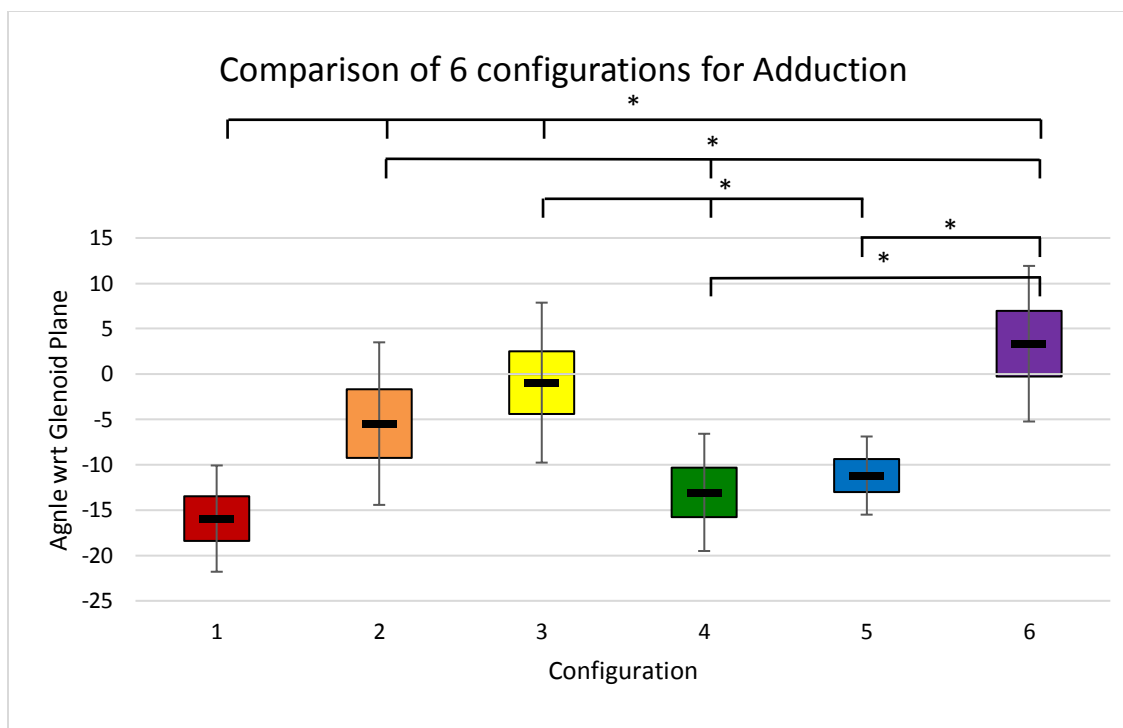


Figure 2.15: Comparison of 6 configurations in Adduction

Boxes represent the upper and lower bounds of the 95% confidence interval, with the thick black bar depicting the average value of all angular locations and specimens. Asterisks indicate a significant difference between mean ranges of motion. ($p < 0.05$).

Pairwise comparisons are summarized below in Table 2.4. The significance level was set at $p < 0.05$, and significant differences are highlighted in green.

Table 2.4: Pairwise comparisons for mean differences in Adduction range of motion

	Config 1	Config 2	Config 3	Config 4	Config 5	Config 6
Config 1						
Config 2	-10.471 p<0.0005					
Config 3	-14.987 p<0.0005	-4.515 p=0.062				
Config 4	-2.889 p=0.325	7.582 p=0.007	12.098 p<0.0005			
Config 5	-4.743 p=0.239	5.728 p=0.427	10.244 p=0.004	-1.854 p=1.000		
Config 6	-19.279 p<0.0005	-8.08 p=0.002	-4.292 p=0.53	-16.39 p<0.0005	-14.536 p<0.0005	

Forward Elevation Range of Motion

For forward elevation, points (6-12), configuration was found to again have a significant effect on the range of motion. Configurations 1, 2, and 3 have the most allowable motion at forward elevation as shown in Figure 2.16. These configurations all share a vertical glenoid yoke that is lowered 5 mm from the center of the glenoid and the longer center trunnion.

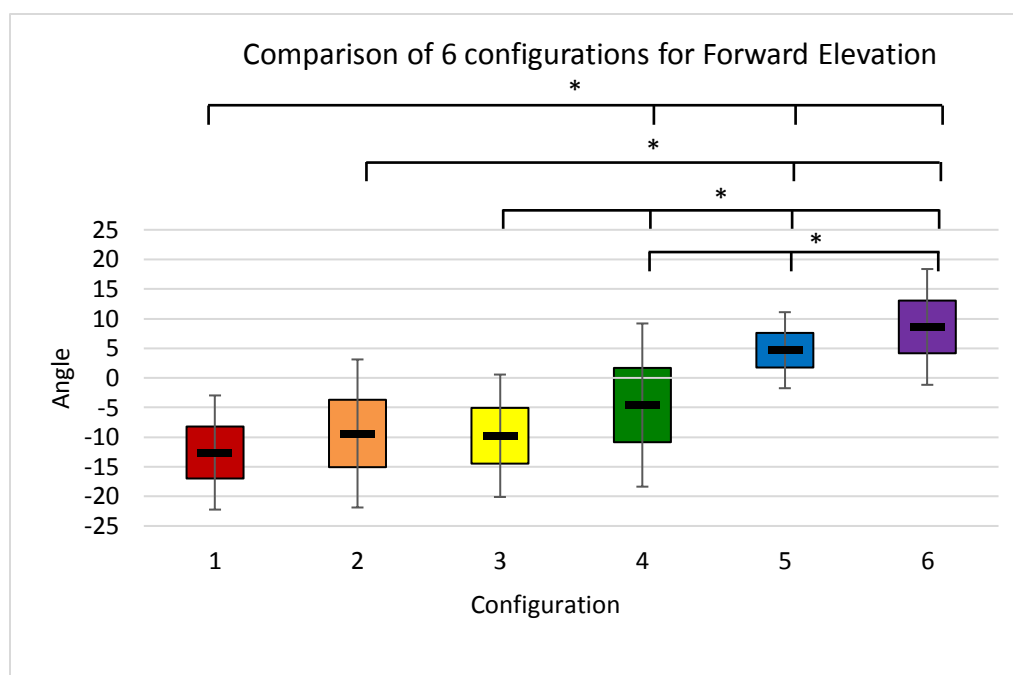


Figure 2.16: Comparison of 6 configurations for Forward Elevation range of motion

Boxes represent the upper and lower bounds of the 95% confidence interval, with the thick black bar depicting the average value of all angular locations and specimens. Asterisks indicate a significant difference between mean ranges of motion. ($p < 0.05$).

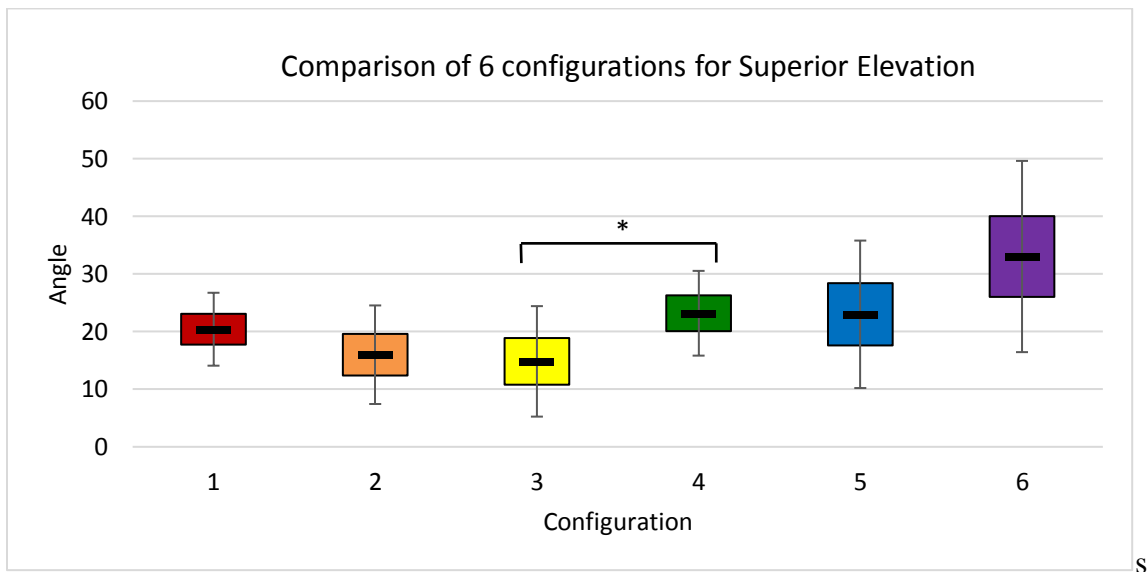
Pairwise comparisons are summarized below in Table 2.5. Significant differences are highlighted in green, with the significance level set at $p < 0.05$.

Table 2.5: Pairwise comparisons of mean differences in Forward Elevation

	Config 1	Config 2	Config 3	Config 4	Config 5	Config 6
Config 1						
Config 2	-3.216 p=1.000					
Config 3	-2.828 p=0.433	-0.388 p=1.000				
Config 4	-8.012 p=0.003	-4.796 p=0.63	-5.184 p<0.0005			
Config 5	-17.273 p<0.0005	-14.057 p<0.0005	-14.445 p<0.0005	-9.261 p=0.023		
Config 6	-21.202 p<0.0005	-17.986 p<0.0005	-18.374 p<0.0005	-13.19 p=0.017	-3.929 p=0.961	

Superior Elevation Range of Motion

For forward elevation, points (28-30, 1-5), configuration was not found to have a significant effect on the range of motion ($p=0.108$). There were no differences between any configurations, except for configurations 3 and 4. (Figure 2.17)

**Figure 2.17: Comparison of 6 configurations for Superior Elevation range of motion**

Boxes represent the upper and lower bounds of the 95% confidence interval, with the thick black bar depicting the mean humeral axis angle. Asterisks indicate a significant difference between mean ranges of motion. ($p<0.05$).

Pairwise comparisons are summarized below in Table 2.6. Significant differences are highlighted in green, with the significance level set at $p < 0.05$.

Table 2.6: Pairwise comparisons of mean differences in Superior Elevation

	Config 1	Config 2	Config 3	Config 4	Config 5	Config 6
Config 1						
Config 2	4.426 $p=1.000$					
Config 3	5.580 $p=1.000$	1.154 $p=1.000$				
Config 4	-2.770 $p=1.000$	-7.197 $p=0.428$	-8.350 $p < 0.0005$			
Config 5	-2.588 $p=1.000$	-7.015 $p=1.000$	-8.168 $p=0.740$	0.182 $p=1.000$		
Config 6	-12.618 $p=1.000$	-17.044 $p=1.000$	-18.198 $P=0.873$	-9.847 $p=1.000$	-10.029 $p=1.000$	

Table 2.6 above illustrates that, with the exception of configurations 3 and 4, there are no significant differences in joint angle in the superior elevation quadrant based on the configuration of the implant. This can be explained by the coracoid and acromion processes – these bony prominences restrict the range of motion in this quadrant, and thus we see their effects here, rather than the effects of the implant configuration on the range of motion.

Posterior Elevation Range of Motion

For forward elevation, points (21-27), configuration was found to again have a significant effect on the range of motion ($p < 0.0005$). However, the results from pairwise comparisons do not differentiate any one configuration for providing a superior range of motion within the posterior elevation motion quadrant. (Figure 2.18)

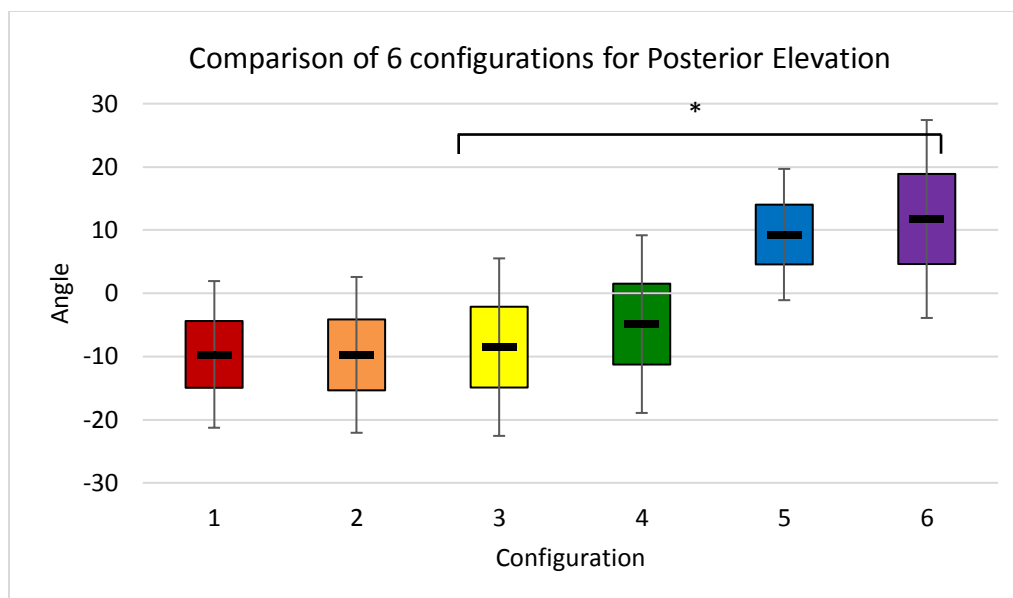


Figure 2.18: Comparison of 6 configurations for Posterior Elevation range of motion

Pairwise comparisons are summarized below in Table 2.7. Significant differences are highlighted in green, with the significance level set at $p < 0.05$.

Table 2.7: Pairwise comparisons of mean differences in Posterior Elevation

	Config 1	Config 2	Config 3	Config 4	Config 5	Config 6
Config 1						
Config 2	0.075 p=1.000					
Config 3	-1.151 p=1.000	-1.226 p=1.000				
Config 4	-4.794 p=1.000	-4.869 p=1.000	-3.643 P=1.000			
Config 5	-18.970 p=0.419	-19.044 p=0.337	-17.819 p=0.198	-14.176 p=0.192		
Config 6	-21.428 p=0.151	-21.503 p=0.103	-20.277 p=0.041	-16.634 p=0.228	-2.459 p=1.000	

The results from posterior elevation and superior elevation do not show a distinguishable configuration that provides a superior range of motion. Although these motion quadrants are physiologically relevant, they are not areas frequently occupied by the humerus, and thus are not the critical criteria for evaluating the range of motion of this implant.

Since configuration 1 is represented in both the top scorers of forward elevation and adduction, as well as best overall range of motion, it is the clear choice for further study.

Repeatability

Inter-rater repeatability was assessed as the range of motion testing was performed by two people. Variability could be introduced by the manual process of manipulating the humerus; using three independent axes to govern this motion can introduce variability because the order in which rotations were performed can influence the final position. Additionally, the humerus was not always exactly aligned with the templated spokes, and this position variation could affect what areas of bony processes interfere with humeral excursion. Both raters performed the circumduction test protocol for a single configuration. The spoke angles and plane angles (Figure 2.19) were recorded for comparison. Since there were only two raters, the ICC(2) was calculated for absolute agreement for both the spoke and plane angles. The results are below. While there was no correlation between the spoke angles (defined as the angle between the spokes and the line connecting the point to the center of rotation, as on a clock face), there was very good repeatability [ICC(2,2) = 0.892, ($p < 0.0005$)] (for average measures) for the plane angles between raters. Higher agreement between the plane angles is a more relevant measure, because it measures the actual range of motion profile, whereas the spoke angles simply determine the spacing of measurement points. All spoke angles were within 1.5° of the spoke, but the points can be on either side, resulting in about a 3° range that the point may fall in. 3° on a 12° spacing for the spokes on the template is a large percentage, which makes the spoke angle ICC value quite high, especially relative to the ICC for the plane angles. The poor repeatability on the spoke angles is acceptable, since the angular position of the points placed is not a relevant measure of the available range of motion of the joint.

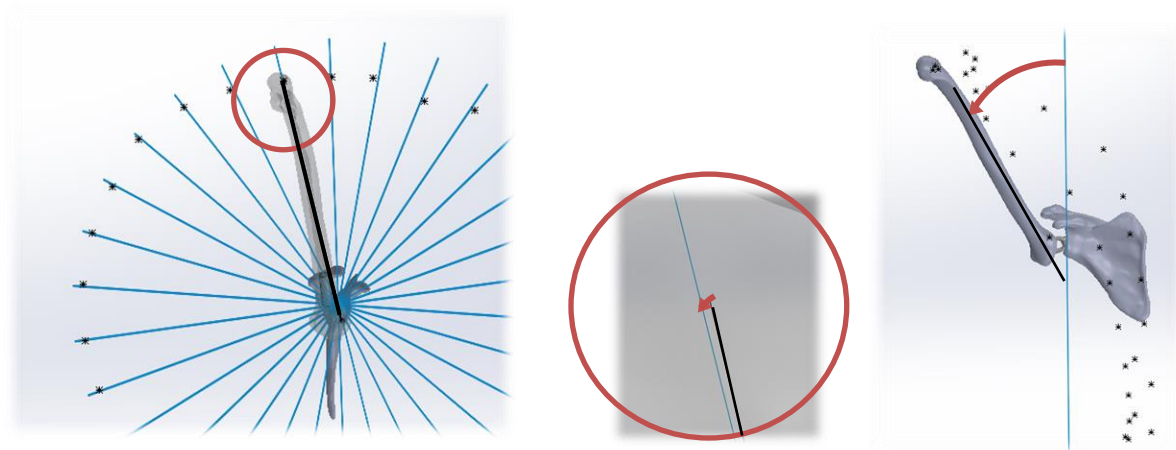


Figure 2.19: Angles used for repeatability analysis

Left: spoke angle. Middle: Enlarged detail to show spoke angle. Right: plane angle

Intra-rater reliability was assessed for the same specimen, with the range of motion tests completed by the same rater (EL) approximately six weeks after the initial assessment. The points of the initial assessment were hidden such that it was a blind test. As with the inter-rater reliability testing, ICC was calculated (in this case ICC(2,1) or “single measures”. The plane angles had excellent correlation [ICC(2,1) = 0.926, ($p < 0.0005$)].

The spoke angles, as with inter-rater reliability, did not show correlation [ICC(2,1) = -0.194, $p = 0.679$].

2.8 Conclusions

The purpose of this chapter was to design a linked implant that would restore normal range of motion to the shoulder joint while providing stability. Once the basic model was created, variations of parameters were set up and tested to determine the configuration that provided the most range of motion, especially in the abduction and forward elevation motions. This configuration was determined to be a vertical glenoid yoke, lowered from the center of the glenoid by 5 mm, tilted inferiorly 20° , with an 8 mm offset between the two pins in the center trunnion. With the configuration providing the largest range of motion identified, finite element testing of the implant can be streamlined by minimizing the number of configurations to analyze.

These results indicate that normal range of motion for a healthy shoulder can be achieved with the use of this linked shoulder implant. Because the model referenced a bony model of the scapula and humerus only, first the average angle between the glenoid face and the frontal plane had to be used to translate the results into a clinically relevant joint angle, so that comparisons with values found in literature could be made.

The glenoid plane used for the reported angular range of motion results is nearly perpendicular to the scapular plane defined by the International Society of Biomechanics definition.⁸⁸ The retroversion of the glenoid plane determines its deviation from perpendicularity from the scapular plane. The glenoid retroversion has been reported to be within 10° of perpendicular to the scapular plane.⁸⁷ The three specimens used in this study all have $3\text{--}5^\circ$ of retroversion between the glenoid plane and the scapular plane. This is consistent with reported glenoid version of normal scapulae.^{96,97} Previous authors have measured the relationship between the resting position of the scapula to the cardinal planes of the body, which are the common references for shoulder range of motion test reports because of their clinical relevance and easy visualization. This measurement is reported to be a 30° angle between the scapular plane and the coronal or frontal plane of the body (Figure 2.20).^{87,98} Thus, the values of forward extension measured from the glenoid plane must be offset by 90° , less the retroversion value, to convert to the scapular plane, and then a further 30° to translate the results into a joint angle referencing the frontal plane. This corresponds to the angular offset proposed by De Wilde et al.,⁹⁹ who recommended a 125° angle between the axis of the glenoid and the frontal plane of the body.

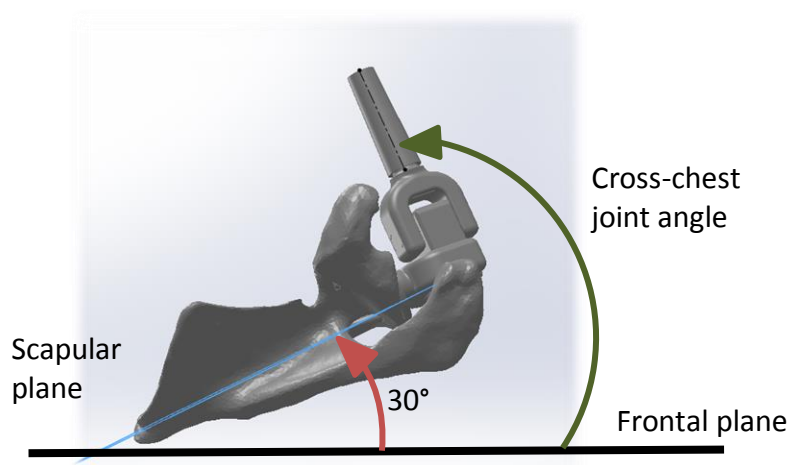


Figure 2.20: Angle between scapular plane and frontal plane. Birds eye view.

Figure 2.20 shows the 30° angle between the frontal plane (black) and scapular plane (blue). 30° must be added to the measured cross-chest joint angle (green arrow) relative to the scapular plane in order to convert into a joint angle referencing the frontal plane.

With this conversion, the maximum joint angle for cross-chest joint angle in 90° of forward elevation is 129° relative to the frontal plane.

While not part of the reported work envelope profile, the true abduction in the scapular plane could reach approximately a 90° glenohumeral joint angle before impingement of the tubercles of the osteotomized humeral head and the protruding glenoid yoke. Once this point was reached, the humerus was internally rotated to continue its abduction arc. The internal rotation retracted the wide portion of the resected humeral head shell away from the glenoid, allowing a larger joint angle. This angle falls short of the 150° threshold to be considered normal joint motion; however, the aim of this study was to determine the work envelope, and with axial rotation of the humerus, the transepicondylar midpoint could reach a maximum superior elevation of 160° in the glenoid plane. If normal scapular rotation is assumed, then the physiologic joint angle between the humerus and torso would be 210°. The acromion and coracoid process will certainly limit humeral elevation before this joint angle could be achieved, thus the implant will allow restoration of normal shoulder range of motion.

A joint angle of 170° between the humerus and torso has been reported for forward elevation in normal healthy shoulders of young adults.¹⁰⁰ This value is expected to decrease as adults age; by 50 years old, the maximum forward elevation joint angle decreases to 155° .^{100,101} Westerhoff et al.¹⁰² reported on joint angles of 4 patients following shoulder joint replacement. The mean active elevation joint angle was 135° , ranging from 110° to 160° .¹⁰² This suggests the linked implant will allow sufficient superior elevation capacity to match both age-matched healthy shoulders as well as a successful traditional shoulder replacement.

A limitation that must be addressed when comparing these results to in-situ range of motion testing is the lack of soft tissue in this model. Soft tissue and joint capsule tension serve to constrain the joint, therefore a bony model will overestimate the allowable joint angle.¹⁰³ Nonetheless, it is an important result to know that the implant will not be the limiting factor in the patient's range of motion. Another limitation was that the scapula-thoracic movement was not measured. It is accepted that the scapula tilts upward within the scapular plane as the arm is raised, beginning at 60° of humeral excursion, with a 2:1 ratio of glenohumeral angle to scapulothoracic angle.^{3,16,17} However, in patients with shoulder pathology, including chronic instability, the scapular kinetics may be altered.^{5,104} This may be due to weakness in the muscles that rotate the scapula. Therefore, a stationary scapula, as was modelled here, may serve as a worst-case scenario for pathological shoulders. Additionally, superior elevation range of motion was limited by the coracoid and acromion processes, so any joint angle contribution by scapular tilting will be matched by a lesser glenohumeral angle, still resulting in a range of motion that is at least as high as that of a normal, young healthy shoulder.

Finally, the range of motion was evaluated in only three shoulders. While the sample size is not large enough to draw conclusions about the effects of bony morphology on joint range of motion, it does allow analysis to determine the overall trends arising from parameter variations of the implant configuration, which was the goal of this study. Variability in bony morphology is expected in a clinical practice, and measurements referencing the plane of the glenoid rim will follow this variability. In general, the glenoid

plane is expected to be nearly perpendicular to the scapular plane defined by the International Society of Biomechanics.⁸⁸

The strengths of this study revolve around the comprehensive range of motion measurements made. The full circumduction motion profile was included, which is more detailed than other studies which only report the joint angle in limited motions. Most studies report only on maximal abduction, forward elevation, and internal/external rotation at 90° of humeral elevation.⁵³ This ignores evaluation of overall mobility of the three simultaneous rotational degrees of freedom shoulder, and is an important metric especially for a non-anatomic joint replacement design.

Additionally, the protocol used is highly repeatable, making it an effective method to consistently measure available range of motion in virtual shoulder models.

Thus, with the best configuration for range of motion identified, the linked implant design was subsequently evaluated using finite element analysis, and these results are reported in the next two chapters.

Chapter 3

3 Finite Element Analysis of the Linked Implant in Activities of Daily Living

OVERVIEW: Ensuring the implant will withstand expected loading in its intended use is vital to the future successful use of the proposed implant. The scope of the current chapter is on the development of a computational model to assess the ability of the proposed geometry and size of the implant components to bear clinically relevant loads. Load vectors from telemetrized traditional shoulder implants were used for the applied force, with the glenoid component assumed to be fixed. The goal of this chapter is to verify that the stresses experienced by the linked implant in physiologically relevant loading scenarios do not approach the failure criteria.

3.1 In-vivo Loading of Clinical Implants

After decades of joint implant research, testing, and analysis of failed implants, fatigue has been determined to be the primary mechanical failure mode of implants,^{105,106} resulting from the cyclical loads of everyday activities. However, failure due to static yielding from occasional high stresses must also be ruled out for a successful implant. Based on the geometry of the joint, slightly eccentric compressive forces are expected, resulting in bending and contact stresses of the implant components. These stresses may be estimated through finite element analysis software, and compared with the allowable stress of the implant material.

While load data specific to the proposed universal joint is not yet known, it can be approximated using force and moment loads from a previous instrumented shoulder implant. Bergmann et al.^{102,107} modified a commercially available humeral implant to measure force and moment joint reaction loads relative to the center of the humeral head. Joint reaction forces could be isolated for any motion and input as the load vectors in

computational models of the shoulder joint, referencing a common coordinate system between the reported joint loads and the finite element model.

Although joint reaction forces are somewhat dependent on the joint geometry, and thus the data from a TSA implant may not be fully representative of the loads on a universal joint implant, most joint load studies are indirectly calculated,^{108–110} and therefore are less reliable than a direct measurement. There was high variability in the measured load data, as the participant's motion path was left unconstrained, only the endpoint was dictated, as would be done in regular daily life. Multiple participants performed the same tasks, and repeated each task several times. Variability between participants was higher than variability between multiple movements performed by the same participant.¹⁰² Since this published data is used in this chapter to evaluate the possibility of failure, the highest values of the joint reaction forces were used as a worst case scenario, and variability can be neglected.

3.2 Materials and Methods

3.2.1 Material Selection

As a starting point for material selection, common materials for orthopedic implants as well as high performance drive shaft universal joints were considered. The most important criteria for this application were high bending strength, wear resistance, and high fatigue strength. Biocompatibility and bio-inertness were not prioritized as one of the design goals is to enclose the linked implant within a biocompatible silicone boot^{80,111} to isolate both the linkage and any generated wear particles from the patient's joint capsule and tissues.

Commercial datasheets for high strength universal joints indicate low alloy, heat treated steels (often hardened AISI 8620 grade alloys) are most commonly used to produce a high performance joint.^{112,113} However, some high strength joints are made of medium carbon steel alloyed with cobalt, nickel, and/or molybdenum¹¹⁴ or high carbon steel needle bearings combined with cobalt chromium molybdenum alloy (CoCrMo) and nickel for the trunnion assembly.¹¹⁵ Comparing the mechanical properties of low alloy steel to CoCrMo indicates similar yield strength and fatigue strength, varying by alloy and heat treatment process, but the low alloy steel does not have excellent resistance to adhesive wear,

especially if paired to itself (CES EduPack 2016, Granta Design Ltd, Cambridge, UK). Wear particles are to be minimized, as third body particles trapped in the boot may damage the joint surface and contribute to further wear of the implant.

A material selection plot was created in CES, using the criteria of fatigue strength and yield strength. A second selection threshold was added; only materials classified as having an “excellent” adhesive wear resistance were included in the final candidates. The candidate materials identified are presented in Figure 3.1 below.

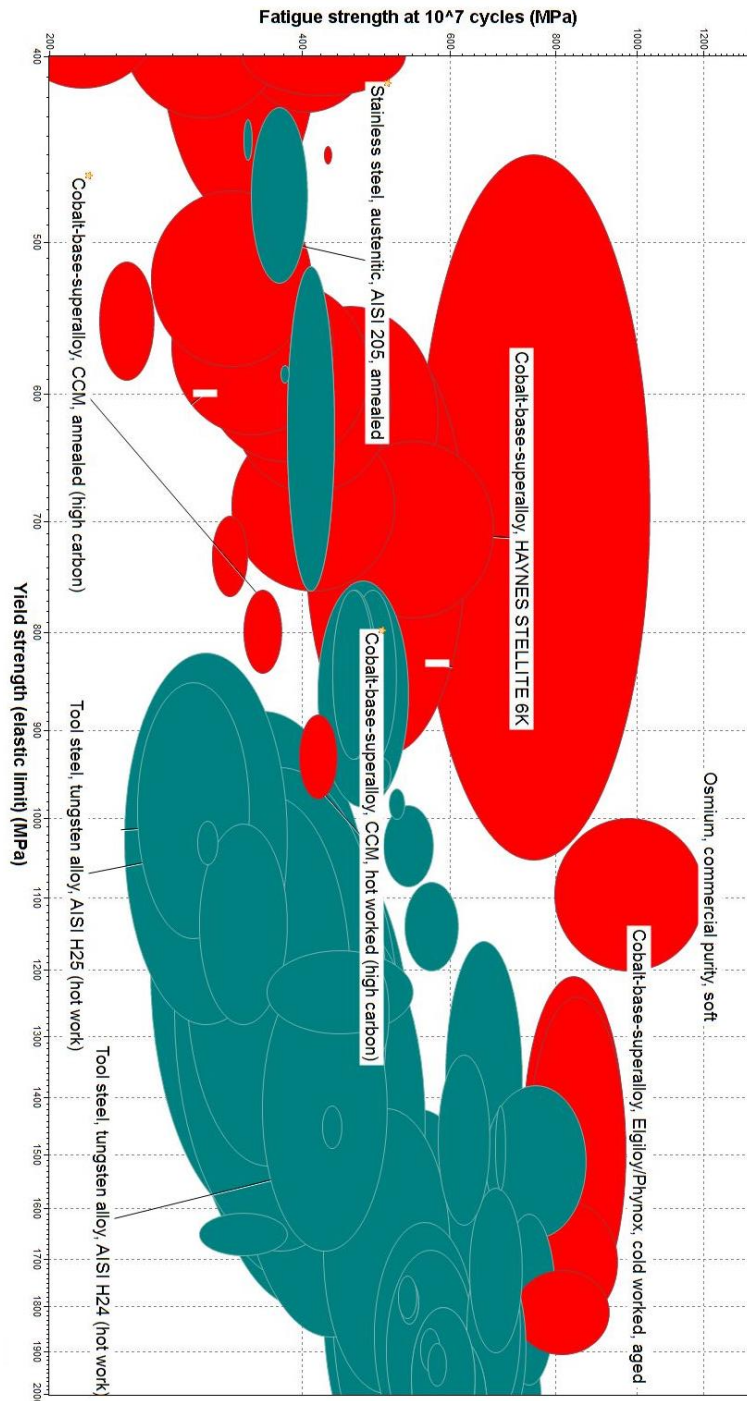


Figure 3.1: Material selection graph

The main criteria for selection were fatigue strength and yield strength, with only materials having excellent adhesive wear resistance considered viable candidates (coloured materials).

Within the materials successfully used in high strength universal joints, CoCrMo is shown to be a more appropriate choice for an implanted universal joint due to its higher strength and superior wear resistance. As the focus of this project was to assess the functional capability of a universal joint to act as a shoulder implant, extensive material selection to consider exotic materials for design optimization was not undertaken. This is considered future work pending successful preliminary testing.

The finite element analysis (FEA) of the linkage was split into two major analyses: the first was a static yielding check based on two different aggressive loading scenarios, and the second was a fatigue analysis of repeated low angle elevation movements with no weight in the hand (unloaded). The analysis was performed both in SolidWorks and Simsolid software. SolidWorks FEA uses a traditional method of meshing each part and calculating the stresses, strains, and displacement at each node of the mesh. Simsolid instead employs external finite element basis functions, with no mesh. The strength of using Simsolid is that no assumptions are required in terms of mesh geometry or boundary conditions, which both tend to be challenging aspects in biomechanics studies. However, Simsolid has generally not been validated for biomechanical applications. Since an experimental model of the linked shoulder implant does not yet exist for validation purposes, the choice was made to utilize both types of FEA software, in order to serve as cross validation. Moreover, since the intent was to analyze stress patterns and safety factors well under yield limits, then absolute agreement between both software was not a requirement.

The target factor of safety range was set between 1.5 and 2 to account for using the highest measured loads for any motion scenario. Considering that the surrounding bone may likely break if the user falls on the arm, extreme scenarios (such as falling) that would impart more force than a user would reasonably be expected to generate on the joint were excluded from this analysis.

3.2.2 Hertzian Contact Stress Analysis

The contact stress was evaluated separately from the bending stresses of each component. Given the pin and block design of a universal joint, the resulting contact between two parallel cylinders can lead to high Hertzian contact stresses. The theoretical contact pattern

of two concentric, parallel cylinders is a line, however, in practicality, small deformations on both components occur, creating a larger contact area which decreases the contact stresses. If the contact stresses exceed the allowable, then pitting of the surface can result, leading to third body wear particles. The surface damage and presence of wear particles can accelerate the wear process, leading to early failure.¹⁰⁶ Two spheres in contact (ball and socket) results in a theoretical point of contact area, compared to a line contact profile of two cylinders in contact. In reality, both contacting surfaces will deform slightly to change the theoretical point and line to a circle and ellipse respectively. Due to the length over which the contact forces are distributed in a two-cylinder configuration, the Hertzian contact stresses will be considerably less than in sphere-on-sphere contact since the force is spread over a much larger area. The deformability of both materials involved also has a role in the contact stress. If the contact is between metal and polyethylene, (the common materials for a ball and socket joint implant) the polyethylene deforms due to its low modulus and thus creates a larger contact area than would be found if both components were made of metal.

The Hertzian contact stress is a function of the two radii of curvature, the length of contact, material properties, and the forces on the cylinders. (The equations can be found in Appendix E). The magnitude and distribution of stresses resulting from contact may be calculated and plotted using Hertzian contact theory.

Friction and surface roughness are not accounted for in the Hertzian model. These simplifications are not fully realistic in practical applications. Therefore, a generous safety factor is beneficial to compensate for these assumptions.

The resultant force magnitude from the Orthoload database was used as the normal force to calculate the Hertzian contact stress. A sliding fit was used to allow free rotation while minimizing the angular misalignment of the pins. The pin and hole diameters with the maximum difference in radii of curvature were used as a worst-case scenario. (Tolerance calculations can be found in Appendix D.)

3.2.3 Static Yielding Analysis

Static yielding was analyzed for two loading scenarios; one in which a participant abducted a 2 kg weight to 90°, and the other where the participant lifted 2 kg to 90° of forward elevation (Figure 3.2). Because of the relatively large moment arm of the weight in the hand to the glenohumeral joint, high joint reaction forces are experienced in the joint. These forces are among the highest measured in the available data and represent a worst-case scenario, especially considering the target patients for a linked shoulder implant are not expected to have high muscular strength or subject the joint to high loads. It is worth noting that the only participants in the study who could complete this task were men in their mid-sixties, (weight close to 200lbs). The more elderly female participants were only capable of performing the unloaded activities, and we consider this to be a more accurate representation of the target functional requirements of the linked implant.



Figure 3.2: Loading scenarios used for analysis

Left: Participant abducts a 2 kg weight to 90°. Middle: Participant lifts a 2 kg weight to 90° of forward elevation. Right: Participant abducts arm to 40° with no weight in the hand (unloaded).

The linkage components were moved to the appropriate configuration to replicate the relevant glenohumeral joint angle in SolidWorks and then imported to Simsolid. A local coordinate system was defined in Simsolid that corresponded to the load measurements taken by Orthoload (Figure 3.3). The origin coincided with the humeral head center of rotation, and the X-axis pointed anteriorly, Y-axis superiorly, and Z-axis distally. With common references and coordinate systems between the model and the load data, no

coordinate transformations were required. The loads and moments were applied to the appropriate faces as remote loads, which automatically transforms the load components to the specified location for load application and compensates for this transformation with an additional moment. The following sections outline the boundary conditions for each part analyzed.

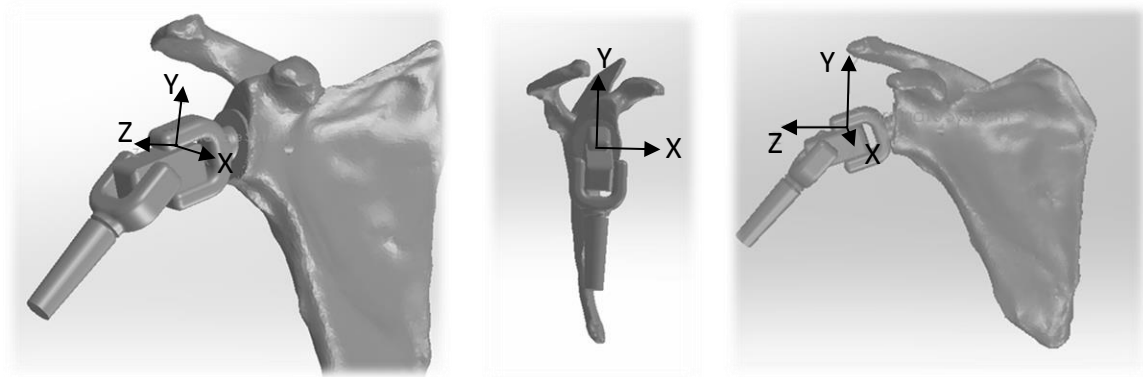


Figure 3.3: Local Coordinate System

The origin coincides with the sphere fit center of the native humeral head. +Y-axis points superiorly, +Z-axis points distally, and +X-axis points anteriorly. This coordinate system is consistent with the measured joint loads by Bergmann et al.^{102,107} Left: Isometric view. Middle: View of XY plane. Right: View of YZ plane.

This procedure was tested for the vertical glenoid yoke, with the glenoid yoke lowered 5mm from the center of the glenoid face, tilted 20° inferiorly, with an 8 mm offset in the center trunnion block, corresponding to the configuration that provided the most range of motion as determined in the preceding chapter.

The maximal stress value and location were recorded from the results of both software. Additionally, average stresses in regions of interest were probed and compared with the material yield strength.

Humeral Yoke

The humeral yoke component was analyzed with consistent boundary conditions and loading between SolidWorks and Simsolid as shown below in Figure 3.4. The stem of the yoke was fixed in place, and the load applied through the pin holes, in a reversed direction, such that the component was still under a compressive bending load. Additionally, the flat inner faces were considered a sliding boundary condition to replicate the sliding contact with the center link component.

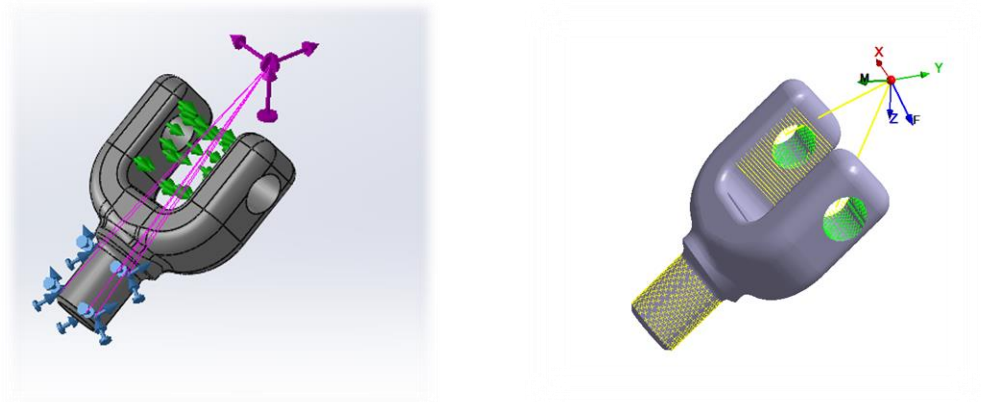


Figure 3.4: Boundary conditions of humeral yoke

Left: SolidWorks depiction of boundary conditions and load. Green arrows represent a sliding connection. Blue arrows represent fixed geometry. Purple arrows represent the resolved load, with the tails travelling back to the face which bears the load. Right: Simsolid depiction of boundary conditions and load. Yellow markers represent both the fixed proximal yoke base, and the sliding boundary condition on the 2 flat faces. The faces that bear the input load are shown with green markers.

The regions of interest probed for average stress values were: the anterior and posterior inner corners of the humeral yoke, the distal and proximal circumferential regions of the base, and the inner faces of the pin holes.

Center Link Subassembly

All connections were considered bonded to provide rigidity and replicate the static position held at each load scenario when the load was applied. Boundary conditions were consistent between SolidWorks and Simsolid as shown in Figure 3.5. Sliding boundary conditions were added on the four longitudinal faces of the center linkage block to constrain movement, as the inner faces of the yokes would provide this constraint in the assembly. The glenoid pin faces that would be in contact with their corresponding holes in the glenoid yoke were fixed. The middle section of both the proximal and distal pins (inside the center link) were constrained using a sliding boundary condition. A remote load was applied to the two outer faces of the humeral pin, referencing the origin of the humeral head sphere fit.

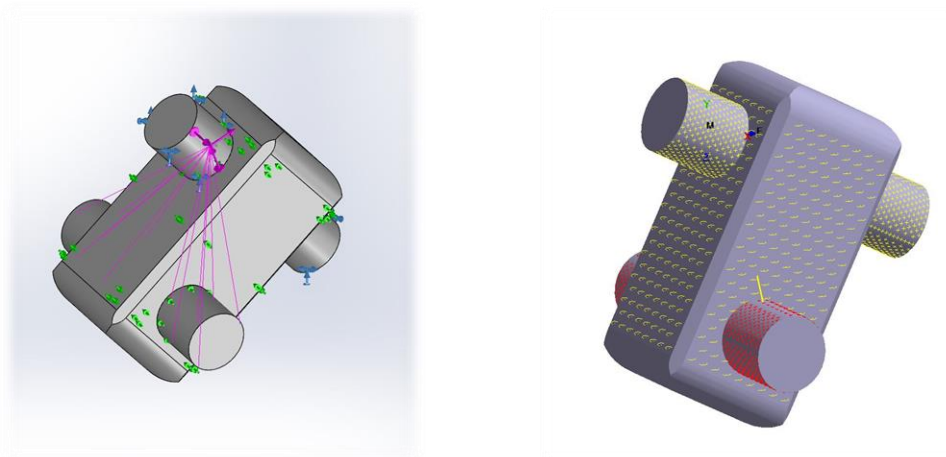


Figure 3.5: Boundary conditions of center trunnion assembly

Left: SolidWorks depiction of boundary conditions and load. Green arrows represent a sliding connection and hinge. Blue arrows represent fixed geometry. Purple arrows represent the resolved load, with the tails travelling back to the face which bears the load. Right: Simsolid depiction of boundary conditions and load. Yellow markers represent both the fixed proximal hinge, and the sliding boundary condition on the 4 flat sides. The distal pin faces that bear the input load are shown with red markers.

Glenoid Yoke

The medial face of the glenoid yoke was fixed in place to model implant fixation. A sliding boundary condition was applied to the inner faces of the yokes to simulate the center trunnion constraint. The remote load acted on the faces of the yoke's pin holes according to the Orthoload joint reaction force. The component was under a compressive bending load, with the resultant force directed superiorly, medially, and slightly anteriorly. (Figure 3.6)

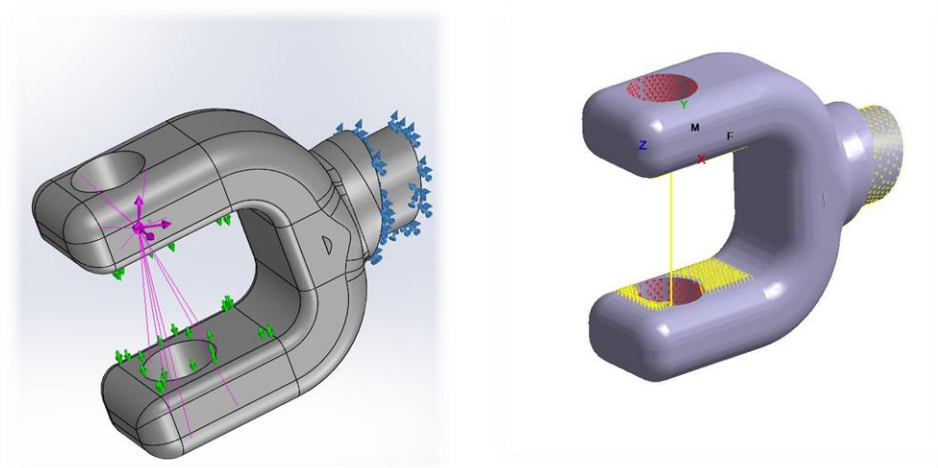


Figure 3.6: Boundary conditions of glenoid yoke

Left: SolidWorks depiction of boundary conditions and load. Green arrows represent a sliding connection and hinge. Blue arrows represent fixed geometry. Purple arrows represent the resolved load, with the tails travelling back to the face which bears the load. Right: Simsolid depiction of boundary conditions and load. Yellow markers represent both the fixed proximal yoke base, and the sliding boundary condition on the 2 flat faces. The distal faces that bear the input load are shown with red markers.

The forces experienced during a loaded forward elevation are higher than that from abduction. Thus, it was considered the critical loading scenario for static yielding.

3.2.4 Fatigue Failure Analysis

Using an instrumented shirt to track arm movements throughout the day, Langohr et al. showed that most arm motion occurs at low elevation angles.⁴⁸ These results are corroborated by Coley et al.⁴⁹ The current ASTM standard F1378 for testing shoulder prosthesis outlines testing to only 100,000 cycles.⁵⁹ However, this value corresponds to less than one year of extrapolated arm abduction cycles using both Langohr and Coley's results.

For fatigue analysis of this implant, a 40° abduction cycle was used to correspond with the most frequent joint angle recorded by Langohr and Coley's studies.^{48,49} If daily activity levels from these studies are extrapolated to a yearly basis, over 2 million 40° cycles per year are expected. It is notable that these studies were performed on healthy subjects, as well as subjects who had undergone successful shoulder arthroplasty, and therefore are expected to have higher functional requirements of the joint than those with chronic instability would expect. Nonetheless, infinite life criteria was used for fatigue analysis at this loading cycle.

Orthoload data was again extracted to correspond with the humerus abducted to 40°. Data was extracted for multiple participants as well as multiple trials, since with a high degree of freedom, the force profiles were quite variable. The highest reported force values from this pool were used, which came from heavier participants with greater muscle strength. The maximum stresses were recorded for comparison with the endurance limit from published S-N curves.¹¹⁶

The maximum von Mises stress value was recorded for each component, along with the corresponding critical location. Following that, average stress values in regions of interest were probed to ensure stress concentrations due to mesh geometry were removed and evaluate for consistency between SolidWorks and Simsolid. The results (maximum and average regional stresses) from both software were compared with separate one-way repeated measures ANOVA's with pairwise comparisons.

3.3 Results

3.3.1 Hertzian Contact Stress Analysis

With a nominal pin diameter of 7.5 mm and a sliding fit, the maximum hole diameter was determined to be 7.520 mm and the minimum pin diameter 7.491 mm. Since contact stresses will be highest with the largest radial mismatch of components, these dimensions represent the worst case scenario. The maximum Hertzian contact stresses occurred in the loading scenario corresponding to a 2 kg in the hand loaded 90° forward extension movement. Calculations may be found in Appendix E. The maximum contact stress within the center trunnion was 60 MPa, less than one tenth of the yield strength (980 MPa) of the material (Cobalt Chromium Molybdenum alloy).

3.3.2 Static Failure Analysis

All components had stress levels lower than the yield stress of wrought medical grade cobalt chrome (Co28Cr6Mo hot worked, high carbon ASTM F1537, UNS R31538).¹¹⁷ The mechanical properties have been reported as: Young's Modulus 220 GPa, yield strength 980 MPa, ultimate tensile strength of 1300 MPa, and a fatigue strength of 624 MPa at over 10 million cycles.^{116–119}

The minimum factor of safety was 1.6 in SolidWorks and 2.0 in Simsolid, occurring in the humeral yoke in the loaded 90° forward elevation loading scenario. The maximum stress result from the SolidWorks finite element model was very concentrated and appears to be a result of a stress concentration due to a mesh effect. Thus, the achieved factor of safety is sufficiently close to the design target factor of safety of 2, providing confidence the linkage component will not yield when loaded in an extreme scenario.

No difference was found comparing the maximum stresses ($p=0.086$) or the average regional stresses ($p=0.25$) recorded in SolidWorks to those recorded in Simsolid. Each component (humeral yoke, center trunnion subassembly, and glenoid yoke) was analyzed for three different loading conditions: (1) loaded abduction, (2) loaded forward elevation, and (3) unloaded low angle abduction. The results for each component in different loading scenarios are presented below.

LOADING CONDITION 1: LOADED ABDUCTION

Humeral Yoke

The location of the highest stress was at the base of the humeral shaft, at the transition between the area constrained by the constrained humeral shaft and the base of the yokes, which is expected given the fixed boundary condition constraint. This location agrees with the intuitive bending stresses expected given the compressive forces acting on the component. Both software show stress distribution concentrated at the base of the yoke, and dissipating outward. (Figure 3.7)

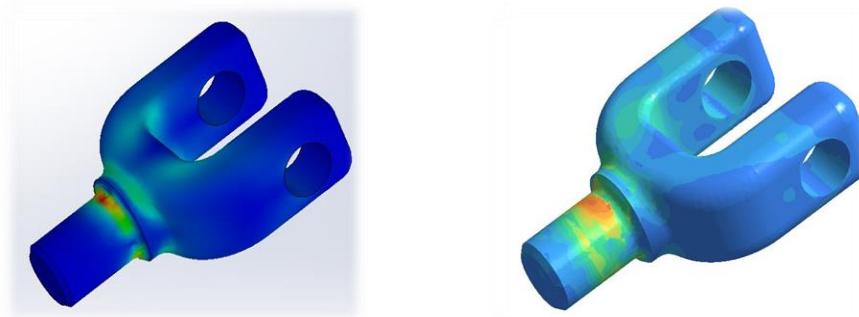


Figure 3.7: Von Mises stress distribution in the humeral yoke under loaded 90° abduction

Stress distribution colour map ranges from 0 MPa (blue) to 480 MPa (red).

Average stresses were recorded for different regions of interest in both software, and found to be well below the yield strength. (Figure 3.8) The minimum factor of safety was 1.6 for the humeral yoke in loaded abduction.

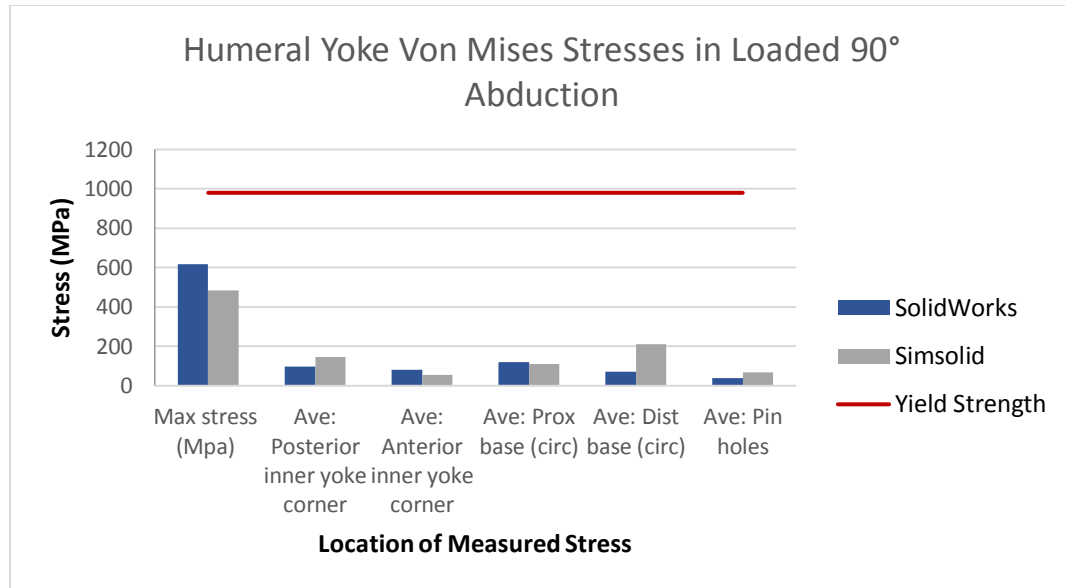


Figure 3.8: Von Mises stress in humeral yoke (CoCrMo) under 90° loaded abduction by region

Glenoid Yoke

The location of highest stress in the glenoid yoke was the outer fillet of the superior yoke. (Figure 3.9) With the resultant force primarily directed superior and medial, the superior yoke bears most of the stress. This fillet could be smoothed in future iterations, however with a factor of safety of 5 at this location, (Figure 3.10) this change is unnecessary for mechanical integrity of the component.

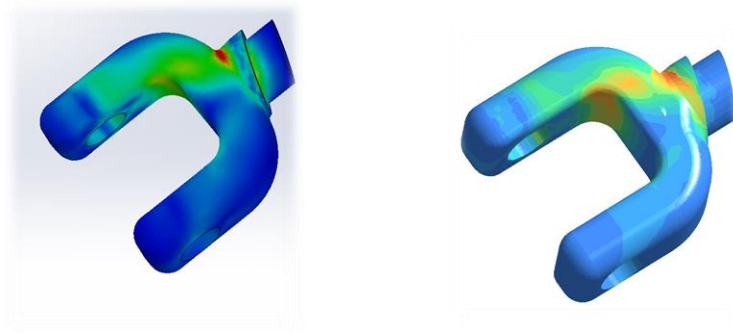


Figure 3.9: Von Mises stress distribution in the glenoid yoke under loaded 90° abduction

Stress distribution colour map ranges from 0 MPa (blue) to 150 MPa (red).

Excellent agreement between SolidWorks and Simsolid average regional stresses was found. (Figure 3.10)

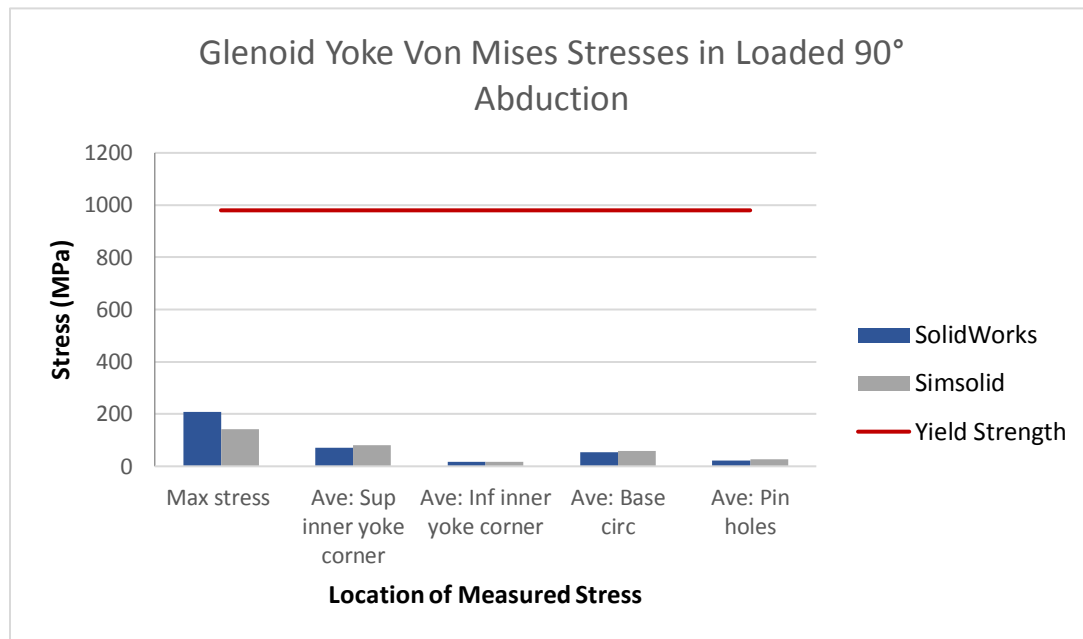


Figure 3.10: Von Mises stress in glenoid yoke (CoCrMo) under 90° loaded abduction by region

Center Trunnion Subassembly

The location of highest stresses in the center trunnion subassembly was on the humeral pins, just outside of the block, and spreading though the center block surrounding the pin. (Figure 3.11)

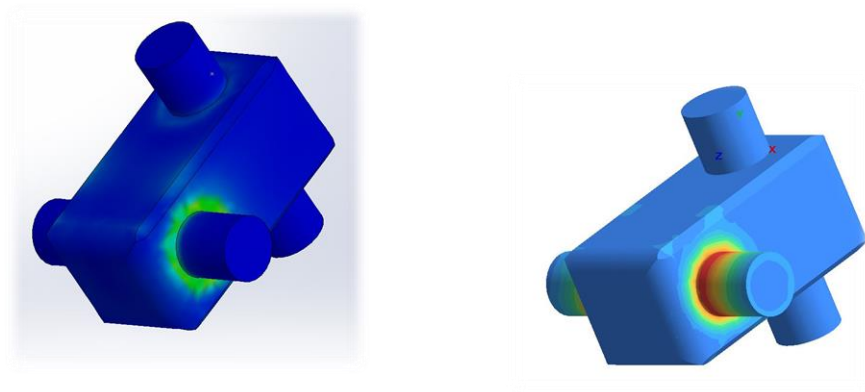


Figure 3.11: Von Mises stress distribution in the center trunnion subassembly under loaded 90° abduction

Stress distribution colour map ranges from 0 MPa (blue) to 120 MPa (red).

The comparison between the SolidWorks and Simsolid stress outputs in the center trunnion subassembly is shown in Figure 3.12 below.

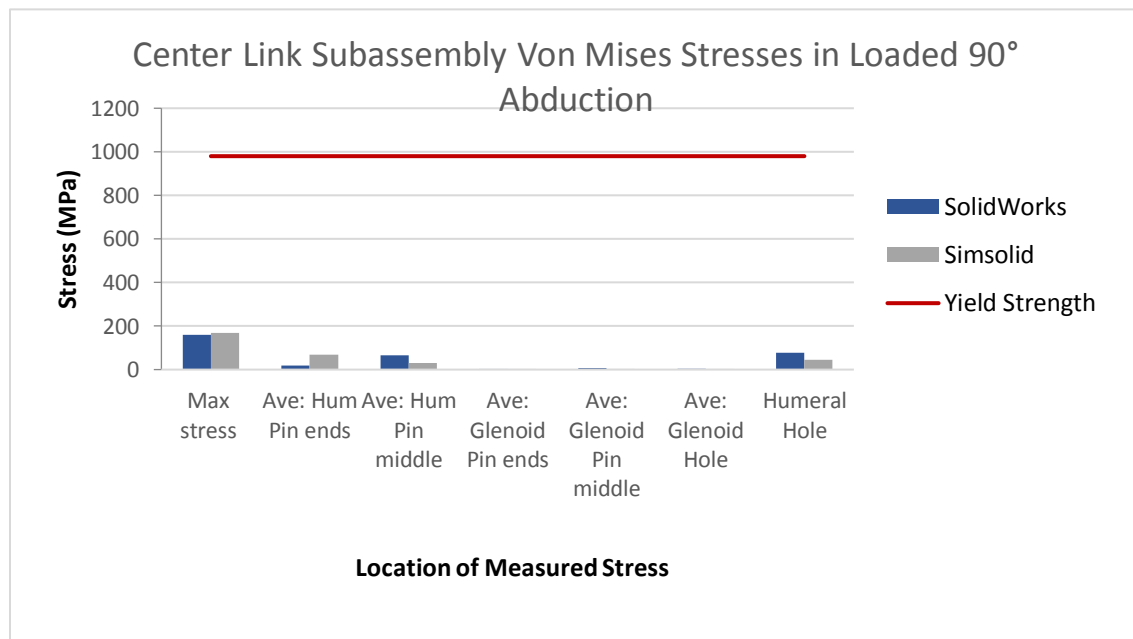


Figure 3.12: Von Mises stress in center trunnion (CoCrMo) under loaded 90° abduction by region

LOADING CONDITION 2: LOADED FORWARD ELEVATION

Humeral Yoke

As in the loaded 90° abduction loading scenario, the critical location in the humeral yoke was in the area between the constrained base and the radius distal to the yokes. (Figure 3.13) The minimum factor of safety for this component is just over 2.

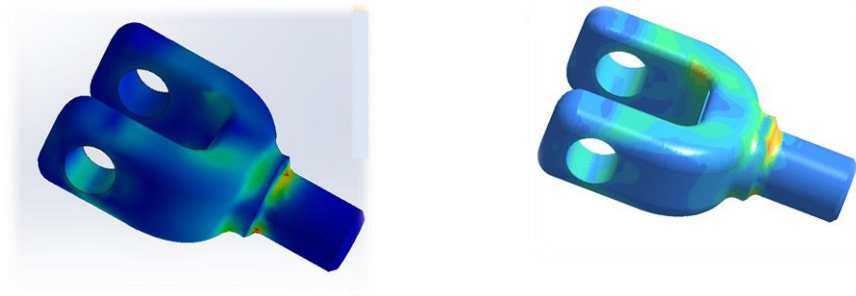


Figure 3.13: Von Mises stress distribution in the humeral yoke under loaded 90° forward elevation

Stress distribution colour map ranges from 0 MPa (blue) to 400 MPa (red).

Interestingly, the singular maximum stress for the loaded forward elevation case is lower than for the loaded abduction case, even with a higher joint force.

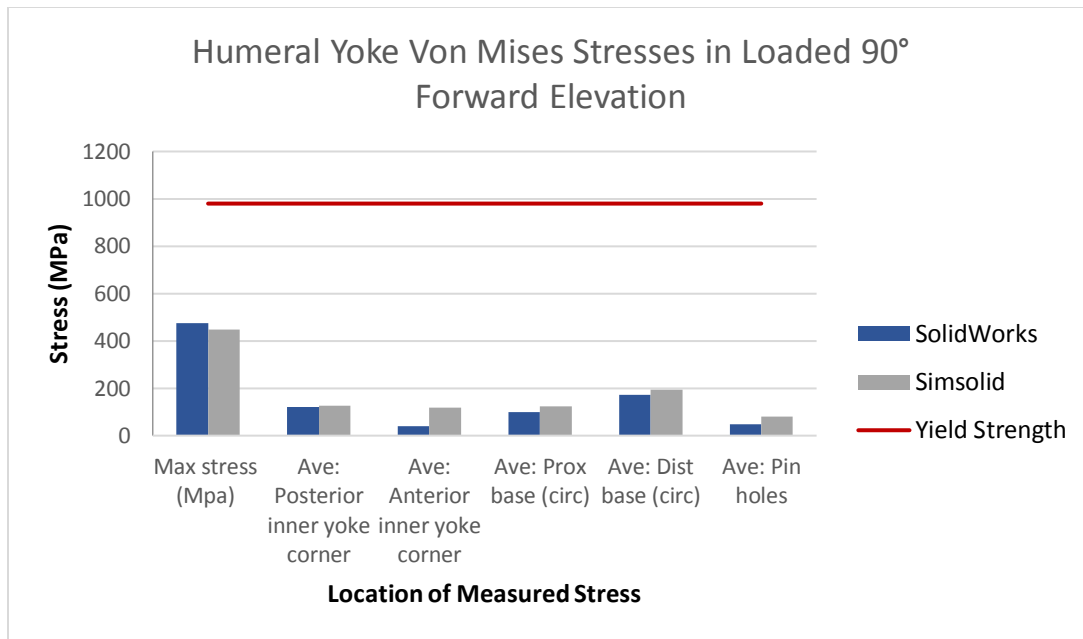


Figure 3.14: Von Mises stress in humeral yoke (CoCrMo) under loaded 90° forward elevation by region

Glenoid Yoke

The stress distribution pattern in the glenoid yoke matches that of the loaded abduction scenario above, although with a slightly higher magnitude of maximum stresses. (Figure 3.15 and Figure 3.16) Since the joint load is approximately 150% of the loaded abduction case, an increase in stress values is in line with expectations.

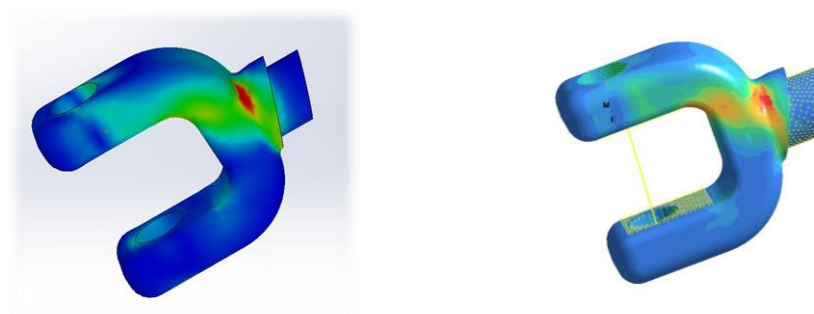


Figure 3.15: Von Mises stress distribution in the glenoid yoke under loaded 90° forward elevation

Stress distribution colour map ranges from 0 MPa (blue) to 200 MPa (red).

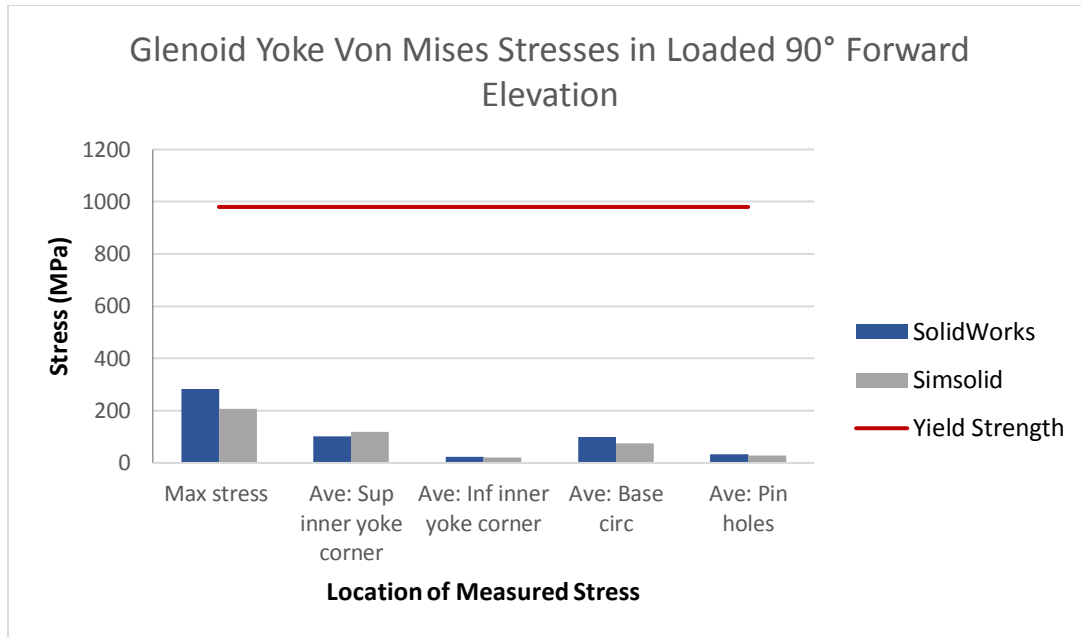


Figure 3.16: Von Mises stress in glenoid yoke (CoCrMo) under loaded 90° forward elevation by region

Center Trunnion Subassembly

The locations of highest stress in the center trunnion subassembly are once again the humeral pin where the load is applied, and the surrounding area of the center block. (Figure 3.17 and Figure 3.18)

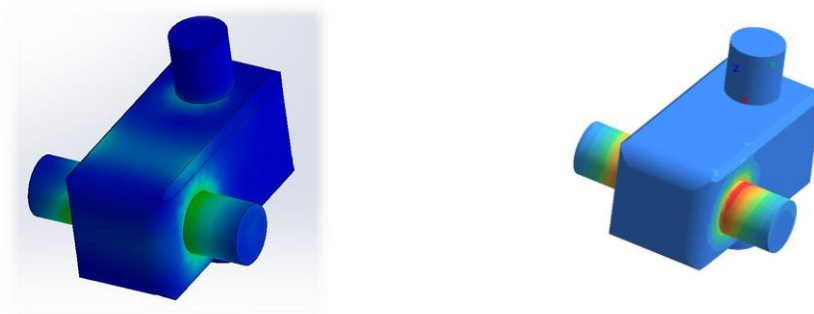


Figure 3.17: Von Mises stress distribution in the center trunnion subassembly under loaded 90° forward elevation

Stress distribution colour map ranges from 0 MPa (blue) to 250 MPa (red).

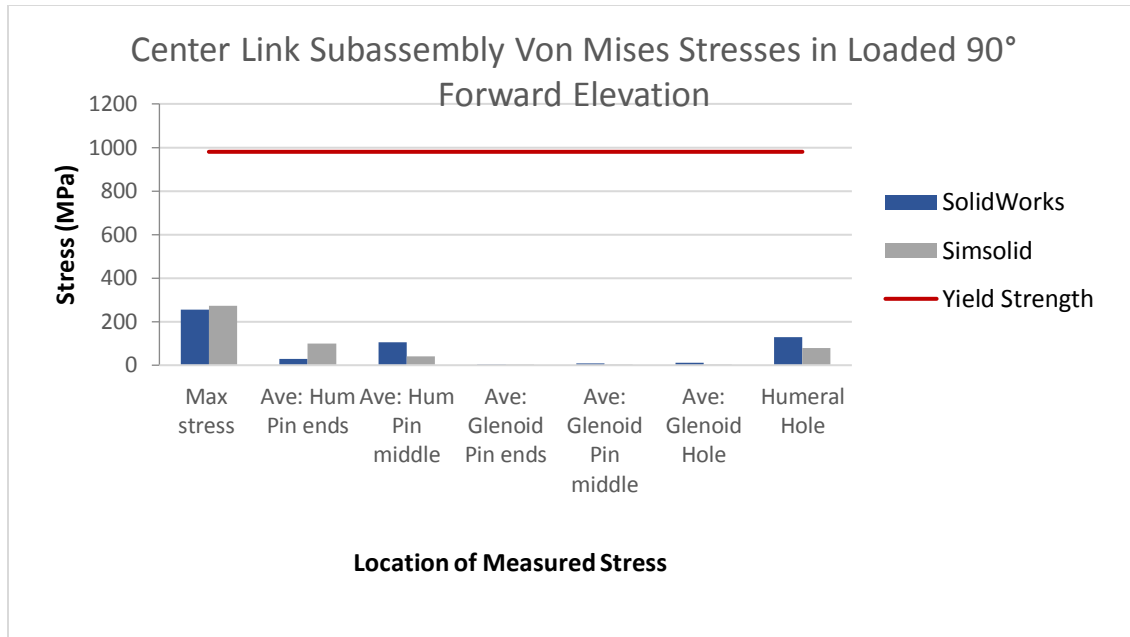


Figure 3.18: Von Mises stress in center trunnion (CoCrMo) under loaded 90° forward elevation by region

3.3.3 Fatigue Failure Analysis

In order to estimate the lifetime of a component, the fluctuating stress must be compared with the fatigue strength. Because the modelled cyclic motion for this analysis is the movement from a neutral position to 40° of abduction, the stresses can be simplified to a fluctuating stress scenario, meaning the minimum stress is 0, and the maximum stress corresponds to the amplitude of the variable stress. This simplification is possible because the components will not be fluctuating between tensile and compressive bending in this low abduction range. Full calculations are presented in Appendix F.

LOADING CONDITION 3: UNLOADED LOW ANGLE ABDUCTION

Humeral Yoke

The location of highest stress in the humeral yoke under low angle, unloaded abduction is also at the transition of the constrained base cylinder and the base of the yokes. (Figure 3.19)

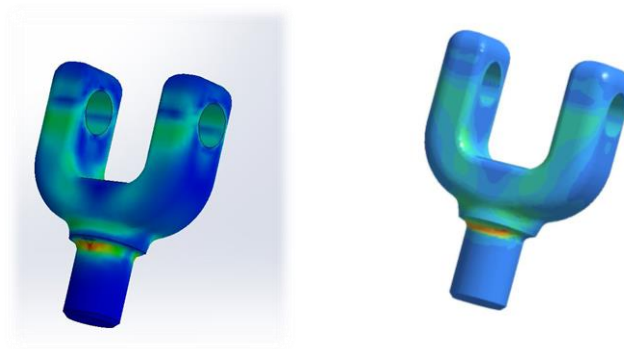


Figure 3.19: Von Mises stress distribution in the humeral yoke under unloaded 40° abduction.

Stress distribution colour map ranges from 0 MPa (blue) to 140 MPa (red).

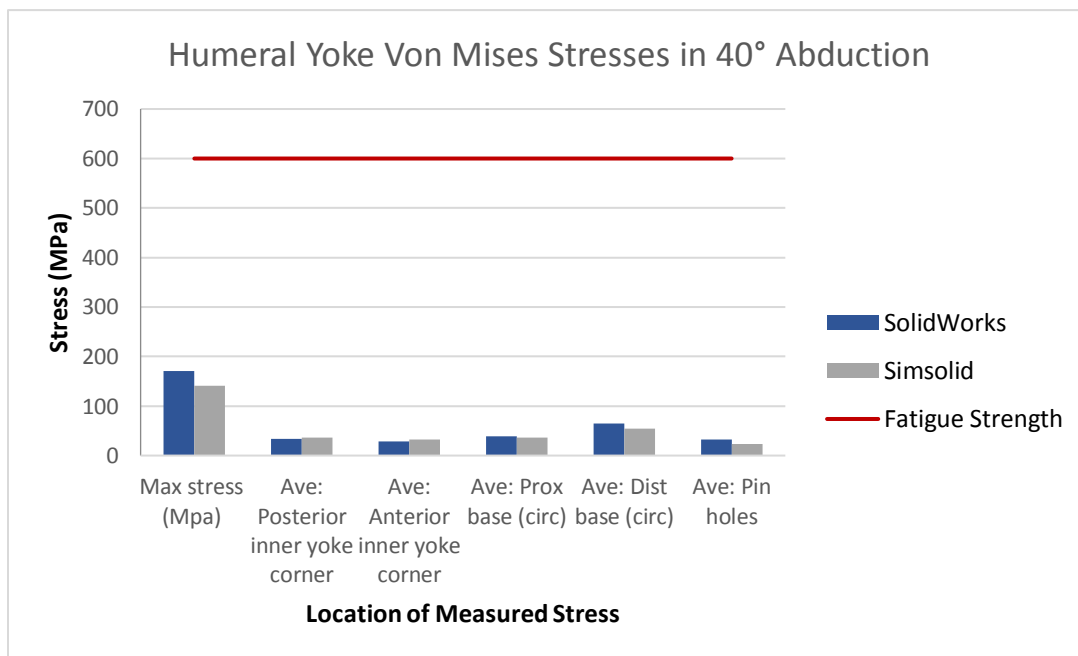


Figure 3.20: Von Mises stress in humeral yoke (CoCrMo) under unloaded 40° abduction by region

Glenoid Yoke

The glenoid yoke in low angle unloaded abduction shows a different stress pattern than that of the loaded 90° abduction. The loading pattern of the unloaded low angle abduction

is mostly a superior force, with only a small compressive force contribution, causing the inferior yoke to experience higher stress, as seen in Figure 3.21.

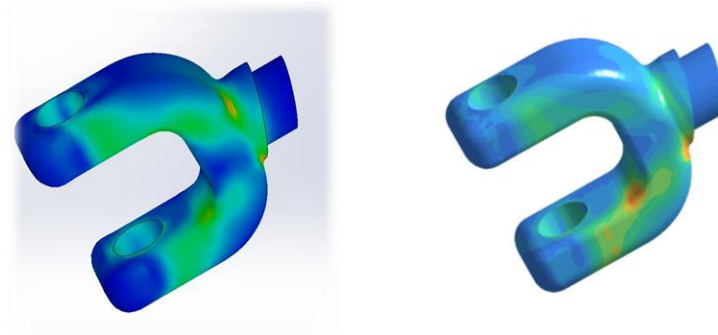


Figure 3.21: Von Mises stress distribution in the glenoid yoke under unloaded 40° abduction

Stress distribution colour map ranges from 0 MPa (blue) to 24 MPa (red).

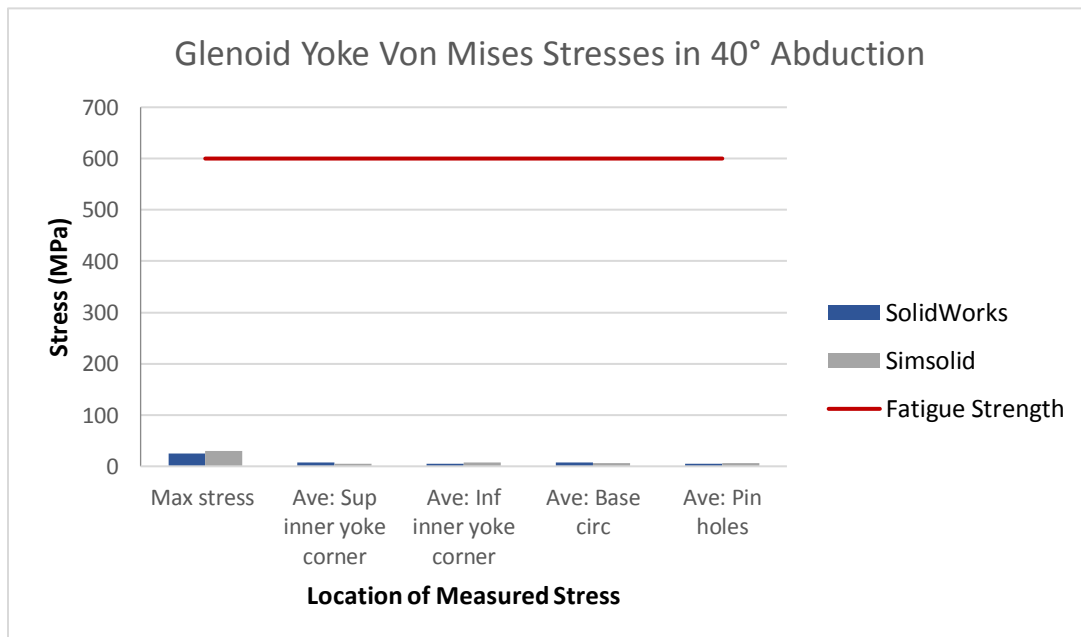


Figure 3.22: Von Mises stress in glenoid yoke (CoCrMo) under unloaded 40° abduction by region

Center Trunnion Subassembly

The humeral pin had the highest stresses in the center trunnion subassembly, due to the compressive forces acting on the exposed faces and the constraint provided by the center block. (Figure 3.23)



Figure 3.23: Von Mises stress distribution in the center trunnion subassembly under unloaded 40° abduction

Stress distribution colour map ranges from 0 MPa (blue) to 90 MPa (red).

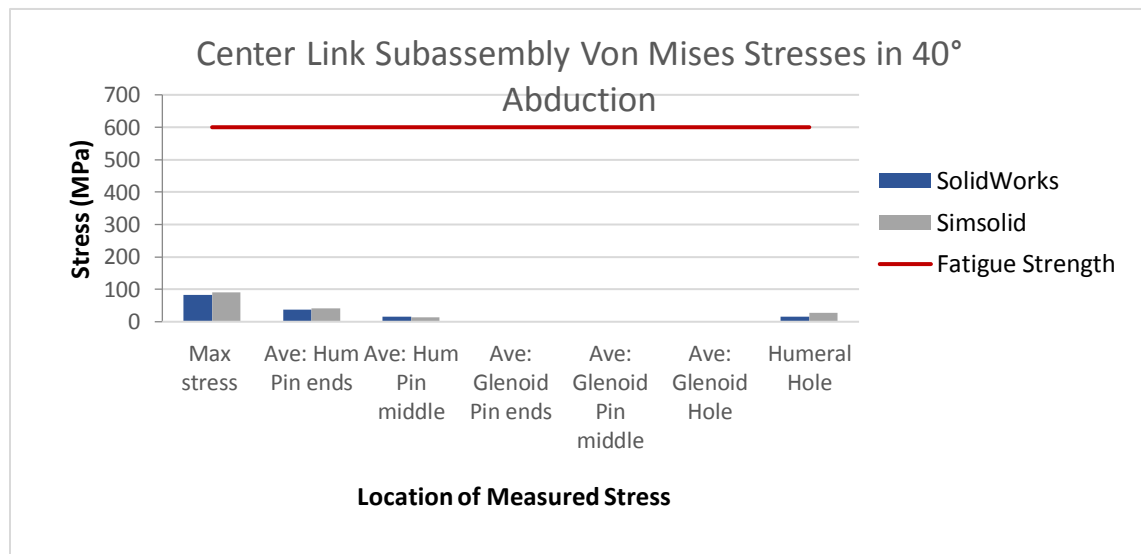


Figure 3.24: Von Mises stress in center trunnion (CoCrMo) under unloaded 40° abduction by region

3.4 Conclusion

All components had a sufficient yield factor of safety (above 1.6) in all loading scenarios tested. The minimum fatigue factor of safety based on an infinite life was 2.15. There was consistency between SolidWorks and Simsolid in both the maximum stress and average stress, as well as the regions where these stresses occurred. Additionally, the locations of the highest stresses were confirmed by both software and are reasonable based on the expected loading scenarios, further serving as validation of the results.

The highest von Mises stress measured in the linkage was experienced in the humeral yoke in all loading scenarios, at the junction of the fixed cylindrical base and the base of the yokes. This may be explained by the longer bending moment arm between the fixed base geometry and the acting point of the load compared to the other components.

Several limitations are present in any modelling study and include stress concentrations due to the automatic meshing in SolidWorks. The seemingly random stress concentrations shown in the base of the humeral yoke suggest that this is an effect of the mesh geometry used, which is further supported by the lack of a focal stress concentration in the meshless Simsolid analysis. Isolating each component for individual stress analysis required the use of boundary conditions to mimic the interaction each part would have with its neighboring parts. Sliding boundary conditions were used, however can over constrain the parts by preventing compression or other out of plane displacements. Another limitation is that Simsolid software allows only one boundary or load condition to be applied on each face, and cannot solve with frictional effects. Friction is expected to be minimal in a lubricated mechanism, but can never truly be eliminated. While in-situ loading data from a TSA implant is expected to provide a more accurate joint force than has been estimated previously, it is unknown how changing the joint geometry from a ball and socket to the linked universal joint will affect the direction and magnitude of the joint reaction force.

It must be conceded that component geometry and material selection play an integral role in static failure and fatigue, and that these details have not yet been established for this linked implant design. The purpose of this chapter was to determine whether an implant of this general linked configuration would be at all feasible – within a wide margin of safety

– based solely on its universal joint design, and the configurations determined in Chapter 2. With this now determined, the analysis moves to bone fixation failure criteria in the following chapter.

Chapter 4

4 Finite Element Analysis of the Glenoid Component Fixation

OVERVIEW: Unlike traditional and reverse shoulder arthroplasty implants, the proposed implant is constrained through its linkage, and thus, it is conceivable that it might impart greater bending moments into its bone fixation. Based on previous constrained implant designs, the glenoid fixation is expected to be a likely failure mode. Therefore, the scope of this chapter is to estimate bone stresses in the context of static bone fixation failure, in order to further evaluate the feasibility and safety of the proposed design.

4.1 Introduction

In order for a joint replacement to be successful, it must be securely fixed to the bone around it to effectively transfer loading through the bone. Loosening of an implant is of significant clinical concern as it is one of the most common reasons for revision surgery, and can impair the fixation ability of the revised component due to bone damage.^{42,61,120,121} Implant loosening is thought to be influenced by multiple factors, and to understand it, the underlying structure and composition of bone must be explored.

Bone is distinguished into two major types: cortical and trabecular bone (Figure 4.1). Cortical bone is harder and more dense than trabecular bone and forms the thin outer shell of a bone. The remaining inner bone is comprised of trabecular bone, a porous, irregular lattice-type structure. Implants primarily interact with the trabecular bone, making it a more important criterion for fixation analysis.

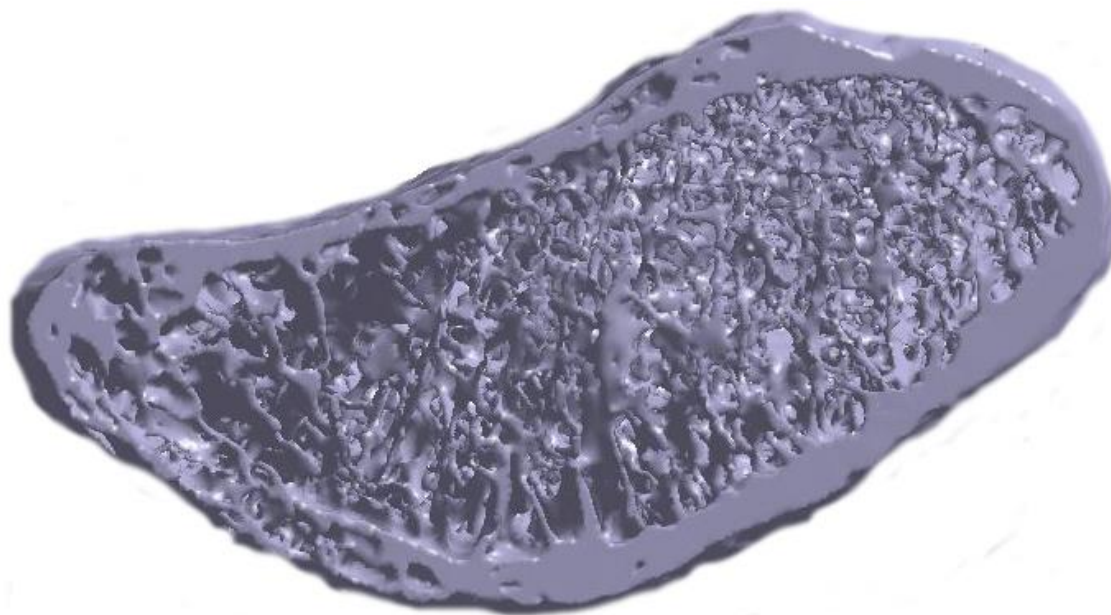


Figure 4.1: Cortical shell surrounding inner trabeculae

Image taken from a cross section of the scapula at the base of the acromion process.

The material properties of bone are highly variable, dependent on factors such as: bone mineral density, age, sex, region of the skeleton, loading, pathology (such as osteoporosis, arthritis).^{122–124} Since bone is a living tissue, it adapts to its loading environment, and through a continual balanced process of resorption and rebuilding, the bone tailors its shape to efficiently support the movements and loads that the joint experiences.^{125,126} As the body ages, this remodeling process becomes less balanced, resulting in a gradual loss of bone density and strength, which causes increased fragility and higher fracture risk.

Bone remodeling around an implant is a complex process that cannot be fully predicted, but is key to preventing implant loosening. Many implants are now coated with a rough surface covered with calcium phosphate to encourage the growth of trabeculae to integrate with the implant surface, thereby achieving a stronger bond between implant and bone.^{25,127} This process is compromised by excessive motion before the new bone growth can be completed, damage to the trabeculae from previous implant removal or third body particles contributes to bone resorption, and the slower bone growth process in older patients.^{60,76}

The region of the skeleton in question is related to its strength, with larger, more load bearing bones having greater density and strength. However, the best predictor of a bone's strength is its apparent density.^{122,128–130} Several authors have aimed to quantify the relationship between apparent density and the mechanical properties of bone.¹²⁹

Both the mechanical properties as well as the geometry of the bone and its individual trabeculae have implications on the fixation strength of an implant. The fixation strength is defined as the maximum stress that can be tolerated before failure of the bone surrounding the implant. Localized failure can lead to implant loosening at the bone–implant interface. While loosening can occur at the implant interface with the humerus or glenoid, the focus of this study is on the glenoid fixation since it is thought to be the weak link of the semi- or fully-constrained shoulder prostheses systems.^{131,132}

There are differences in fixation strength depending on whether an implant is cemented into the bone or fixed with screws and a porous central peg, which allows for bony ingrowth. In this study, uncemented fixation is studied, due primarily to its widespread use in RSA and fixed fulcrum implant designs.^{25,54} Uncemented fixation is thought to provide a stronger bond with the bone, as porous fixation allows for trabecular remodeling and integration of the implant with the bone.¹²⁷

As both RSA and fixed fulcrum shoulder implant systems are considered to have a semi-constrained CoR, an additional loading burden – in the form of bending moments – is imparted on the glenoid component, and transferred to the glenoid bone by way of the fixation pegs and screws.^{131–133} Where the CoR is lateralized from the native shoulder, a higher bending moment is generated due to the load acting at a longer fulcrum distance from the glenoid bone.

The first designs of shoulder replacement prostheses closely resembled modern hip replacement systems, implementing a constrained ball and socket design. These designs were abandoned in favor of less constrained designs due to their high incidence of loosening.¹³¹ The increased rate of loosening was generally considered to be caused by the lateralized CoR imparting greater stresses at the bone-implant interface from an increased moment arm; however, as Pupello¹³⁴ points out, no studies were performed at the time to

establish causation.¹³⁴ Now, as constrained fixed fulcrum implant designs are more likely used for salvage procedures, and semi-constrained RSA designs are gaining favor as primary procedures,³⁴ the effects of lateralizing CoR on bone fixation stress become a more prominent concern.^{35,76} However, most studies on glenoid fixation aim to estimate micromotion of the glenoid baseplate with respect to the bone, rather than the bone stresses. Achieving bony ingrowth depends at least partially on ensuring low levels of implant motion while the bone accommodates the implant.¹³⁵ Longer term success of the implant depends on the bone's ability to withstand the stresses transferred to it from the lateralized CoR.

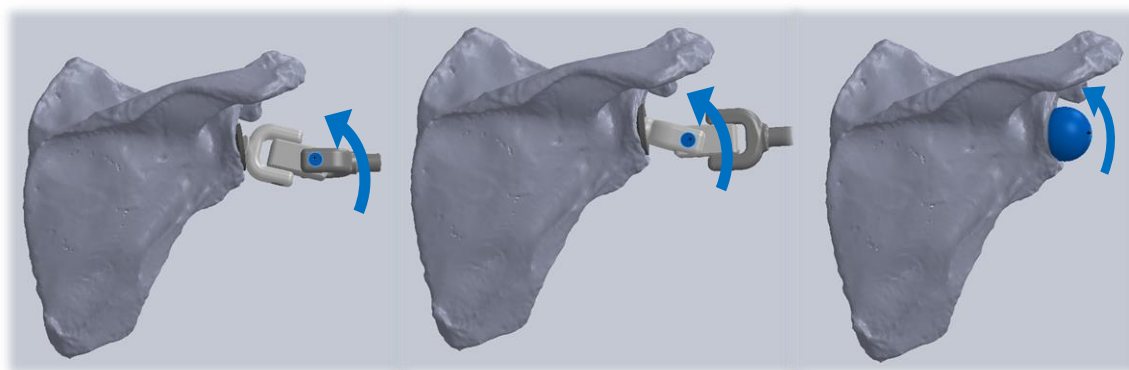


Figure 4.2: Lateralization of the abductor hinges for comparison

Left: Vertical glenoid yoke. The abduction hinge revolves around the distal pin of the linkage. Middle: Horizontal glenoid yoke. The abduction hinge revolves around the proximal pin of the linkage. Right: RSA Glenosphere. The humeral cup revolves around the sphere center.

The purpose of this study was to compare the bone stresses in the glenoid under physiologically relevant loading conditions, based on differing levels of CoR lateralization, and evaluate whether the resulting bone stresses approached the failure limit of bone. The distance of CoR lateralization was based on an existing lateralized RSA implant design (Reverse Shoulder Prosthesis, DJO Global, Texas),⁷⁷ and both the horizontally and vertically oriented glenoid yokes of the linked shoulder joint design (Figure 4.2). It is hypothesized that the further lateralized CoR of the vertically oriented glenoid yoke (VG)

will result in higher bone fixation stresses than either the horizontal glenoid yoke (HG) configuration, or the commercial lateralized RSA (LatRSA) glenosphere.

4.2 Materials and Methods

A 3D scapular model was converted from a cadaveric scapula CT scan (Mimics, Materialise Corp.). The donor was a 78 year old male with no pathology (height: 65 inches, weight: 159 lbs, Donor ID: 15-10049L). The scapula was extracted from the CT scan data using a threshold of 200 HU, and manual post-processing was done to fill any cavities in the 3D model. The scapular model was then exported as an .STL file for import into SolidWorks. A glenoid baseplate for a lateralized RSA implant, based on the DJO RSP, was modelled in SolidWorks as a single part. The baseplate diameter was 25 mm, with a 6.5 mm diameter central screw, and four peripheral screws (4.5 mm diameter) with angle adjustable up to 30°. Both the central and peripheral screws were 25 mm long. The back face was domed with a 3 mm height. The central peg hole was angled 20° in the glenoid bone inferiorly to accommodate the desired tilt of the glenoid yoke, as determined in Chapter 2.

The baseplate was virtually positioned in the scapula, with screw trajectories placed to maximize bony contact (Figure 4.3). The placement was confirmed by a fellowship trained shoulder surgeon (GSA). The central screw and two of the peripheral screws perforated the glenoid vault, which was unavoidable given the 25 mm screw length.

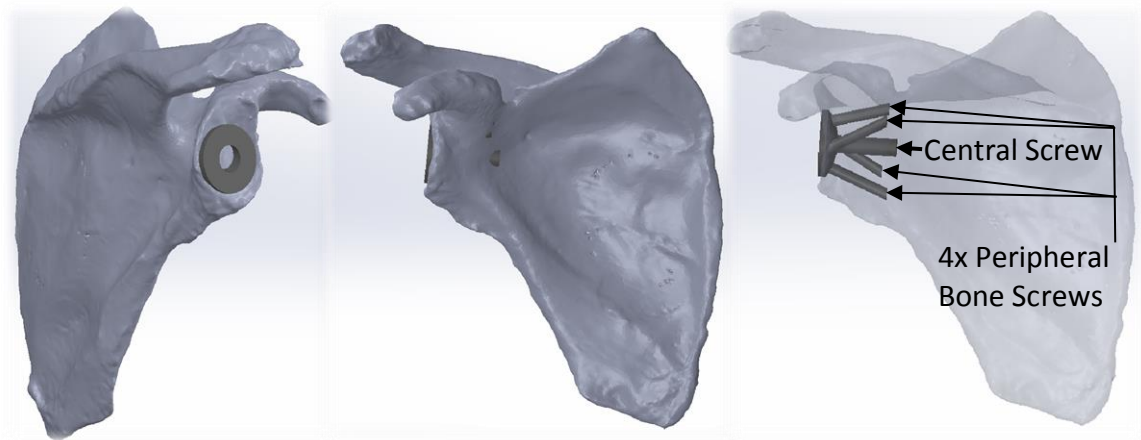


Figure 4.3: Scapula with implanted glenoid baseplate

Left: Oblique view of the glenoid face, showing the position of the baseplate relative to the glenoid. Middle: Anterior view of the scapula, showing alignment of the baseplate relative to the plane of the glenoid rim, and screw perforations of the glenoid vault. Right: Anterior view of the scapula (transparent) to illustrate screw trajectories.

Once the baseplate and screws were positioned in the scapula, the baseplate was Boolean subtracted from the glenoid to simulate a surgical reaming procedure, which establishes a conforming contact surface between the bone and baseplate backside. An adaptive surface mesh was then overlaid onto the glenoid, and then converted into a volume mesh of tetrahedral elements (Abaqus, Dassault Systems, France). A mesh size convergence study was performed for the scapula, resulting in an adaptive surface mesh of 1.3 mm maximum edge length. The baseplate was adaptive surface meshed at a maximum edge length of 0.75 mm. The surface meshes were converted in Abaqus to a quadratic tetrahedral volume mesh (C3D10 elements).⁷⁶

The volume mesh was superimposed onto the original stacked DICOM images from the CT scan in order to assign material properties to each tetrahedral element based on the apparent density of the tissue¹³⁶ (Bonemat v3.2, Istituto Ortopedico Rizzoli, Italy). The apparent density is correlated to the Young's Modulus based on a power function with multiple coefficients reported by various authors.¹²⁹ The individual scanner parameters were calibrated base on the known density of a phantom material (in this case dipotassium

phosphate (K_2HPO_4) and scaling the bone density accordingly. The modulus of each element was calculated by the following equations determined by Eberle et al.¹³⁷:

$$\rho_{ash} = 1.22\rho_{K_2HPO_4} + 0.0523 \quad (1)$$

$$E = 10,200\rho_{ash}^{2.01} \quad (2)$$

All elements in the scapula were assigned a Poisson's ratio of 0.3. The range of Young's moduli calculated for the scapular volume elements was between 65 MPa and 24 GPa. This scapula model was then exported for finite element analysis in Abaqus.

The scapula and baseplate Abaqus files were combined into an assembly (Figure 4.4). The medial edge of the scapula was rigidly tied to a fixed reference point in the middle of the edge to restrict any scapular translational and rotational movement. The contact between the baseplate and the bone was separated into two interactions: the first was comprised of the curved back of the baseplate and central peg, and the second interaction was the four peripheral screws and the surrounding bone. The central peg and baseplate were set as a surface to surface explicit contact, with the baseplate as the master surface, and overclosure adjustment on. This interaction was set to a frictionless, hard contact, which represents an idealized case of the initial implantation of the implant before any bony ingrowth has occurred. The peripheral screws were tied to the surrounding bone. Finally, a damping effect was incorporated to slow the introduction of loading, with a damping coefficient of 0.1 in all directions.

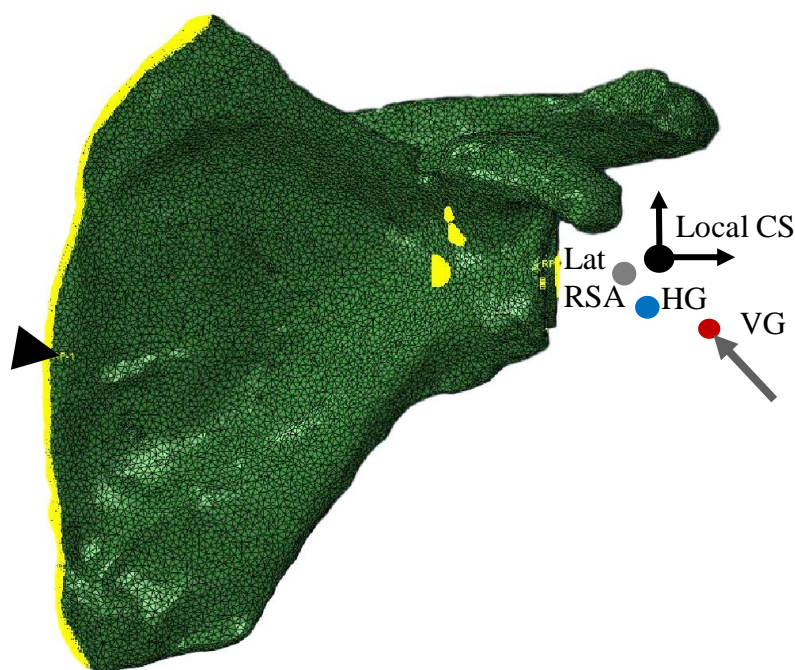


Figure 4.4: FEA model of implanted scapula showing loading and boundary conditions.

All nodes highlighted along the medial edge of the scapula are rigidly tied to a fixed reference point (black triangle) to prevent rotation and translation of the scapula. Loads were applied to each of the three implant hinge points (shown as coloured dots) corresponding to a hinge at 90° abducted arm position. Load (grey arrow) shown acting at VG yoke hinge point. The local coordinate system (Local CS) was located at the sphere fit center of the native humeral head.

The simulated joint load was applied to the lateral face of the baseplate, at a reference node located according to the position of the hinge point. Remote loads were used to account for the load application occurring at different locations than originally measured with a telemeterized implant.¹⁰⁷ The remote load function translates the load to the specified face, and adds the appropriated bending moment to compensate for the translation. To compare the effects of lateralization of the hinge on bone stress, three different positions of the hinge (LatRSA, HG, VG) were used for each loading scenario, and moved as necessary to reflect the fact that the hinge point moves in the VG and LatRSA configurations depending on the

arm position. The load magnitudes and directions were chosen to reflect a variety of activities of daily living, including:

1. 90° of abduction, with a body weight (756 N) in each of the shear (superior) and compressive directions, resulting in a 1080 N combined load. This is a common loading scenario for glenoid fixation FEA studies and is the testing standard for ASTM F2028.^{138–140}
2. Unloaded 40° of abduction: As discussed in the previous chapter, most daily upper extremity movement occurs at low levels of abduction and forward elevation.^{48,49,102}
3. Loaded 90° of abduction: This loading scenario reflects the measured joint load when a participant raised a 2 kg weight to 90° of abduction, from the Orthoload database. The force magnitude is similar to the ASTM F2028 loading scenario, at 1250 N, split primarily between the superior and compressive directions.¹⁰²
4. Loaded 90° of forward elevation: Considered the worst-case scenario, this load represents 2 kg in the hand with a straight arm raised to 90° of forward elevation. It has the highest joint load tested (1700 N), split nearly evenly between the compressive, superior shear, and posterior directions.¹⁰² This load represents over twice the body weight for a 77 kg person. Given that the target patients for a linked shoulder implant have limited function due to chronic instability, and generally lower upper arm strength, this load is likely too aggressive to be performed. However, loads at 1.5-2 times body weight have been estimated for some daily living activities, such as using the arms to lift oneself out of a chair, so this loading scenario was considered aggressive but relevant.^{61,107}
5. Unsupported arm hanging at side: As opposed to active arm movement, which imparts compressive forces on the joint, the unsupported arm hanging at side will put tension on the bone-implant fixation. The weight of the arm was estimated at 5% of total body weight¹⁴¹ and acting at the hinge point of the joint, straight down (-Y direction).

6. Unsupported arm at side with 10 kg weight in hand: The arm weight plus an additional 10 kg was modelled to represent a patient carrying items such as groceries. This resulted in 130 N acting in the -Y direction, acting at the hinge point of the joint. The loads reported by Bergmann et al.¹⁰² are consistent with the forces calculated for loading scenarios 5 and 6.

Once all loads were input and the models were run, the relevant bone stresses were extracted. Von Mises stresses at the centroid of each bone element surrounding each screw were recorded. The 99th percentile,¹⁴² 95th percentile, and 90th percentile^{143–145} maximum stress values and averages were reported (Appendix G) so that the effects of stress concentrations due to mesh geometry could be discounted. All stress values were plotted for visualization of stress distribution, with stress results from each lateralization displayed on the same plot for comparison. A threshold of 10 MPa¹⁴⁶ was used for the glenoid trabecular bone failure limit.

Since the highest stresses occurred surrounding the central screw, a two-way repeated measures ANOVA was performed for the central bone screw, with the load magnitude and lateralization set as factors. There were three levels of lateralization (LatRSA, HG, and VG), and six load levels. Separate one-way repeated measures ANOVA's were performed for the central peg bone stresses for each loading scenario to evaluate pairwise comparisons between the three implant lateralizations. Significance was set at $p < 0.05$.

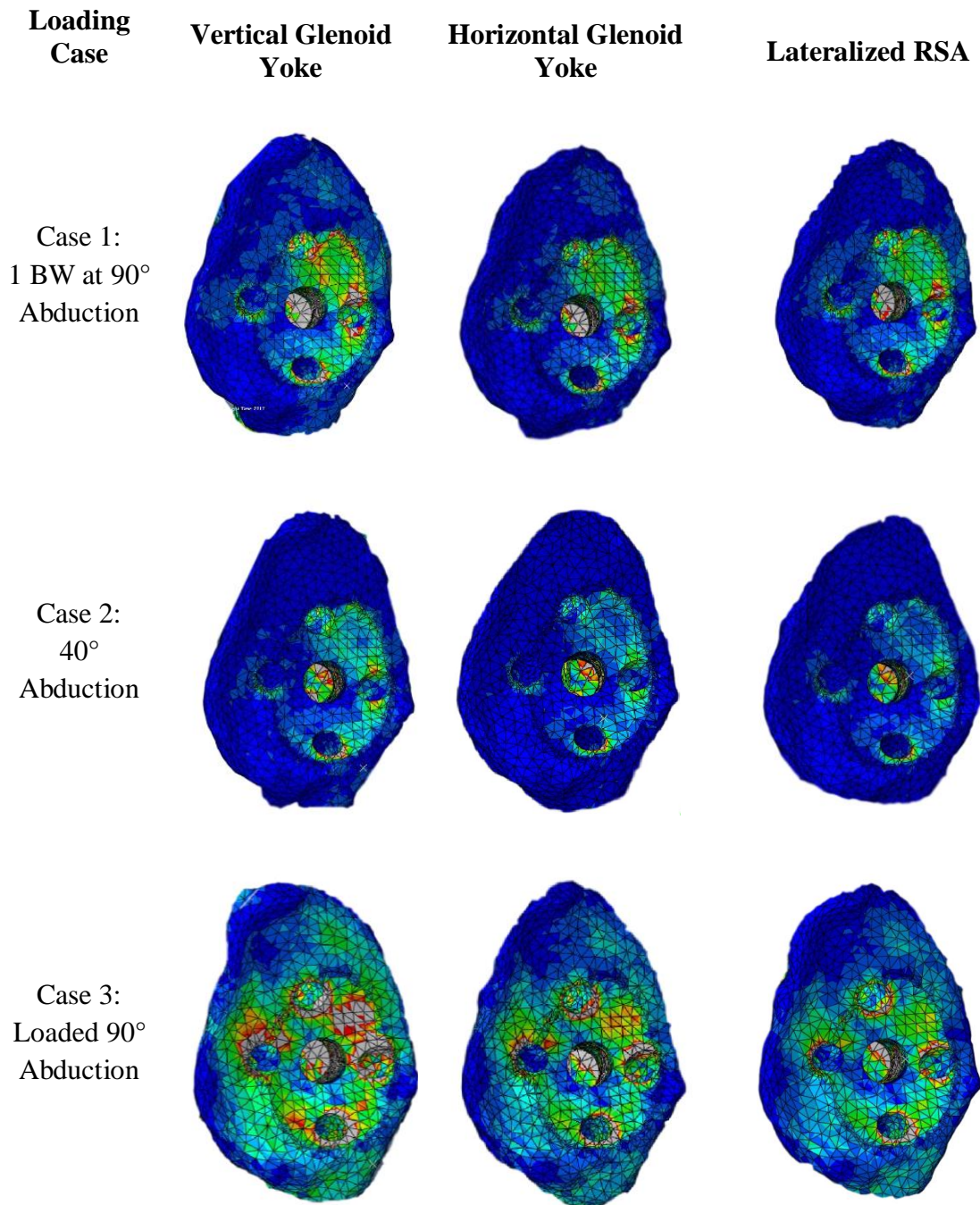
4.3 Results

The two-way RM ANOVA indicated that both lateralization and loading scenario were found to have a significant effect on measured bone stresses in the central screw ($p < 0.0005$). Additionally, a significant interaction was found between lateralization and load ($p < 0.0005$).

The highest stresses reported were found to be in the body of the scapula. Since the scapula is a floating bone, and not rigidly constrained along the medial edge as was done in this model, these stresses were considered an artifact of the boundary conditions. Additionally,

the stresses in the scapular body are unrelated to the fixation strength, so only the stresses surrounding the implant fixation were considered.

The stress distributions by colour mapping within the glenoid face for all loading cases are shown in Figure 4.5.



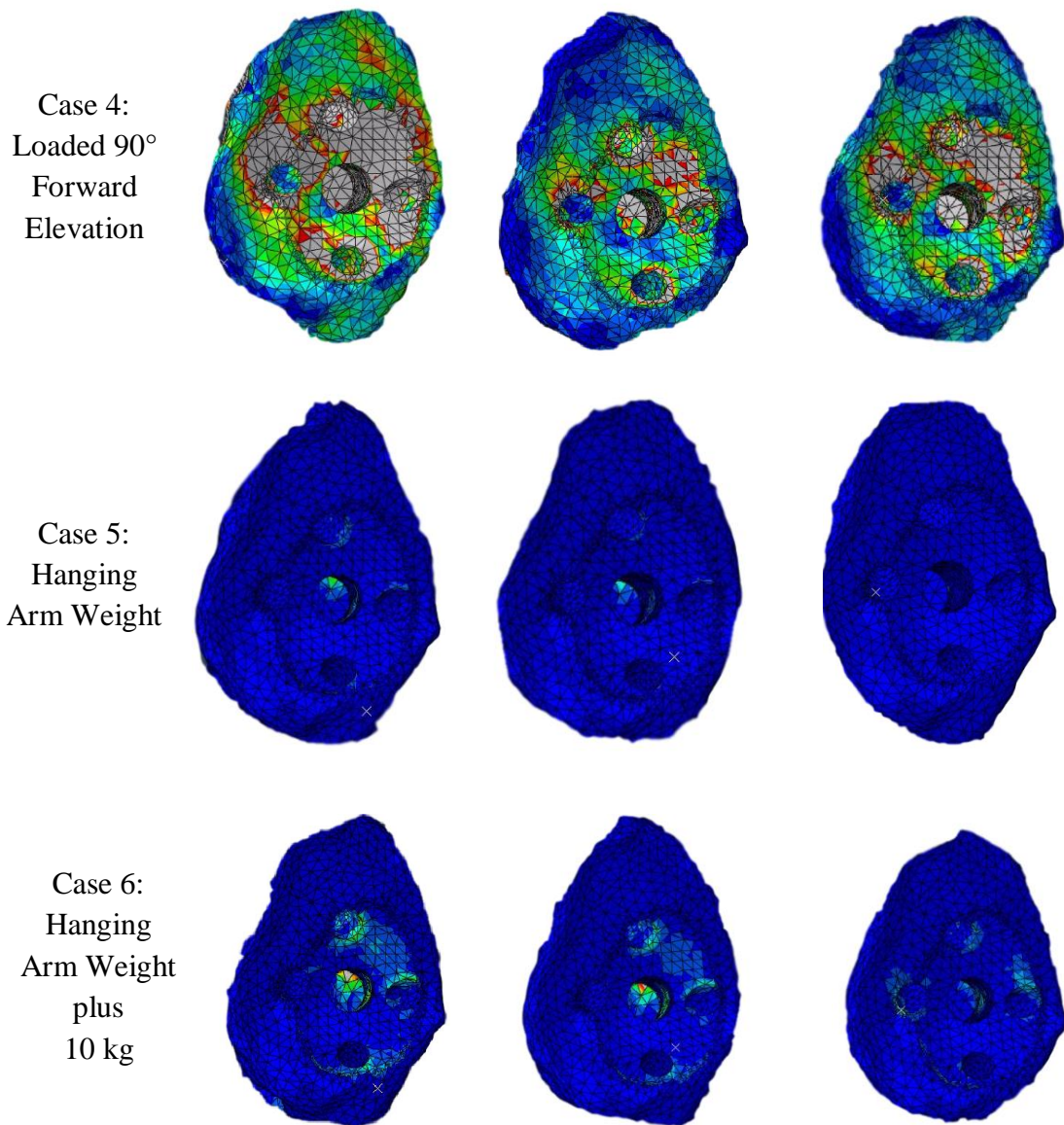


Figure 4.5: Stress distribution in glenoid face

Stress distribution colour map ranges from 0 MPa (dark blue) to 10 MPa (red). Elements with stresses exceeding 10 MPa are depicted in grey.

The bone stresses surrounding the central peg were the highest for all loading cases, thus the bone surrounding it is considered to have the highest fracture risk. Results are plotted in Figure 4.6 - Figure 4.11 for the 90th percentile max and mean stresses for all locations

and loading conditions. The mean and maximum values determined by the 90th, 95th, and 99th percentiles are tabulated in Appendix G.

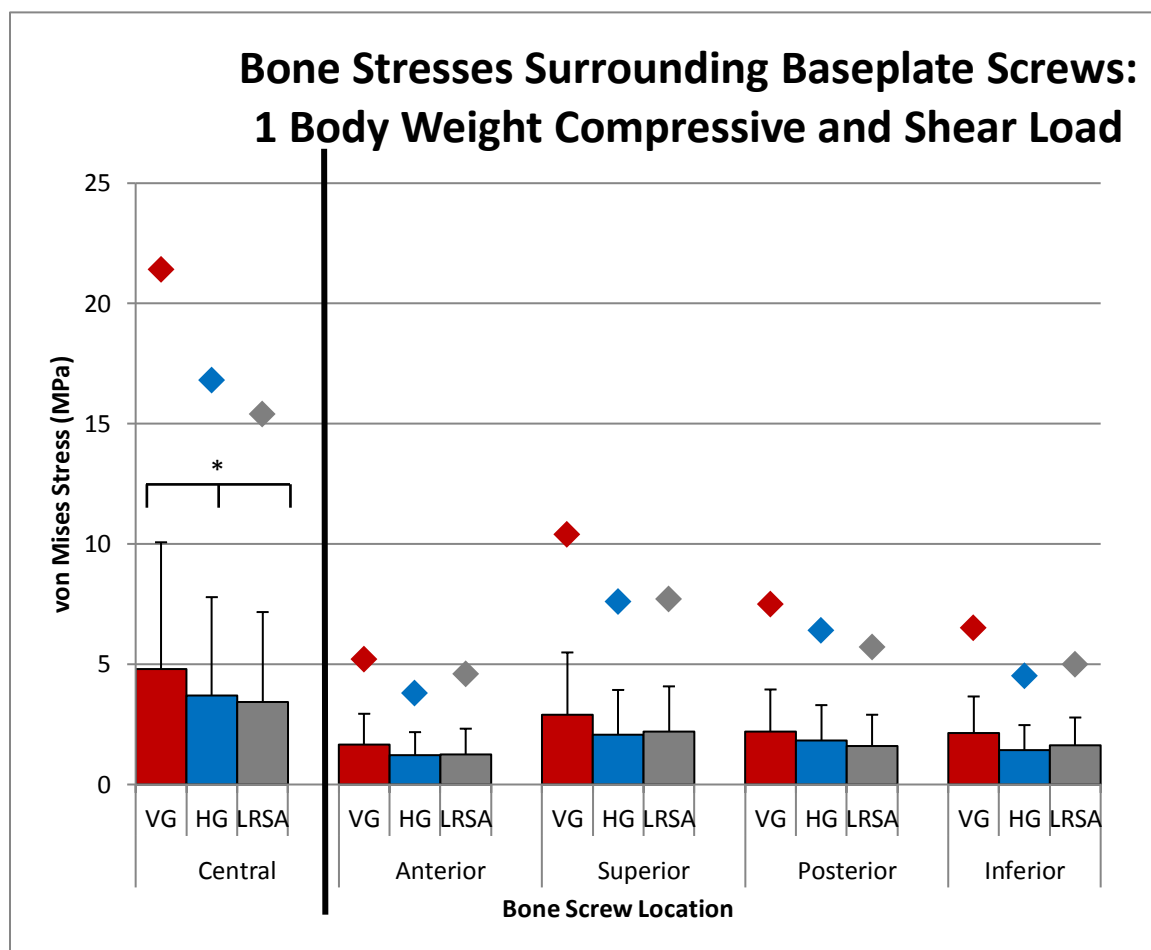


Figure 4.6: Glenoid bone stress: 1 BW Shear and Compressive Load

90th percentile bone stresses surrounding each bone screw grouped by bone screw location. Columns represent the average stress values, the whiskers represent the standard deviation, and the diamonds represent maximum values. Significant differences within the pairwise comparison of the stresses surrounding the central screw are designated with an asterisk ($p < 0.0005$).

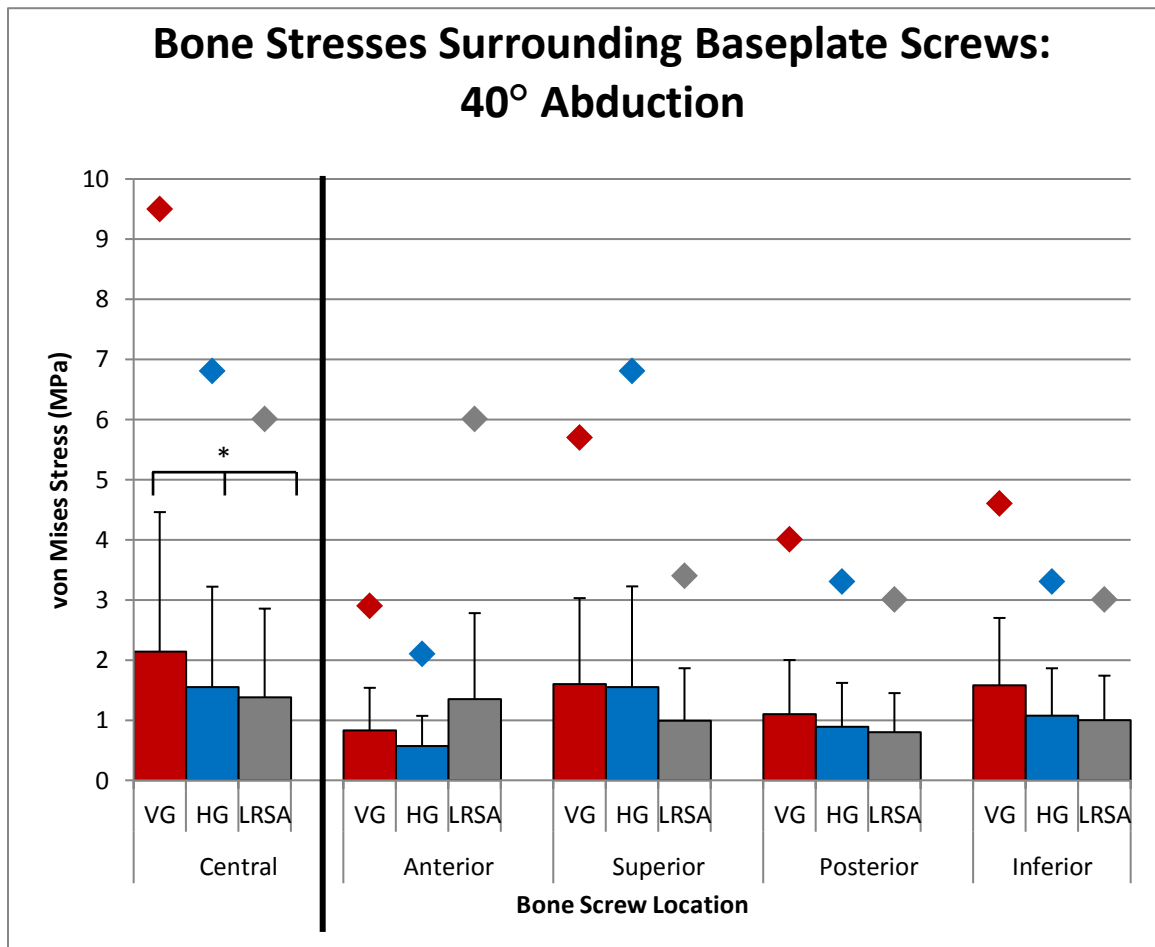


Figure 4.7: Glenoid Bone Stress: Unloaded 40° Abduction

90th percentile bone stresses surrounding each bone screw grouped by bone screw location. Columns represent the average stress values, the whiskers represent the standard deviation, and the diamonds represent maximum values. Significant differences within the pairwise comparison of the stresses surrounding the central screw are designated with an asterisk ($p < 0.0005$).

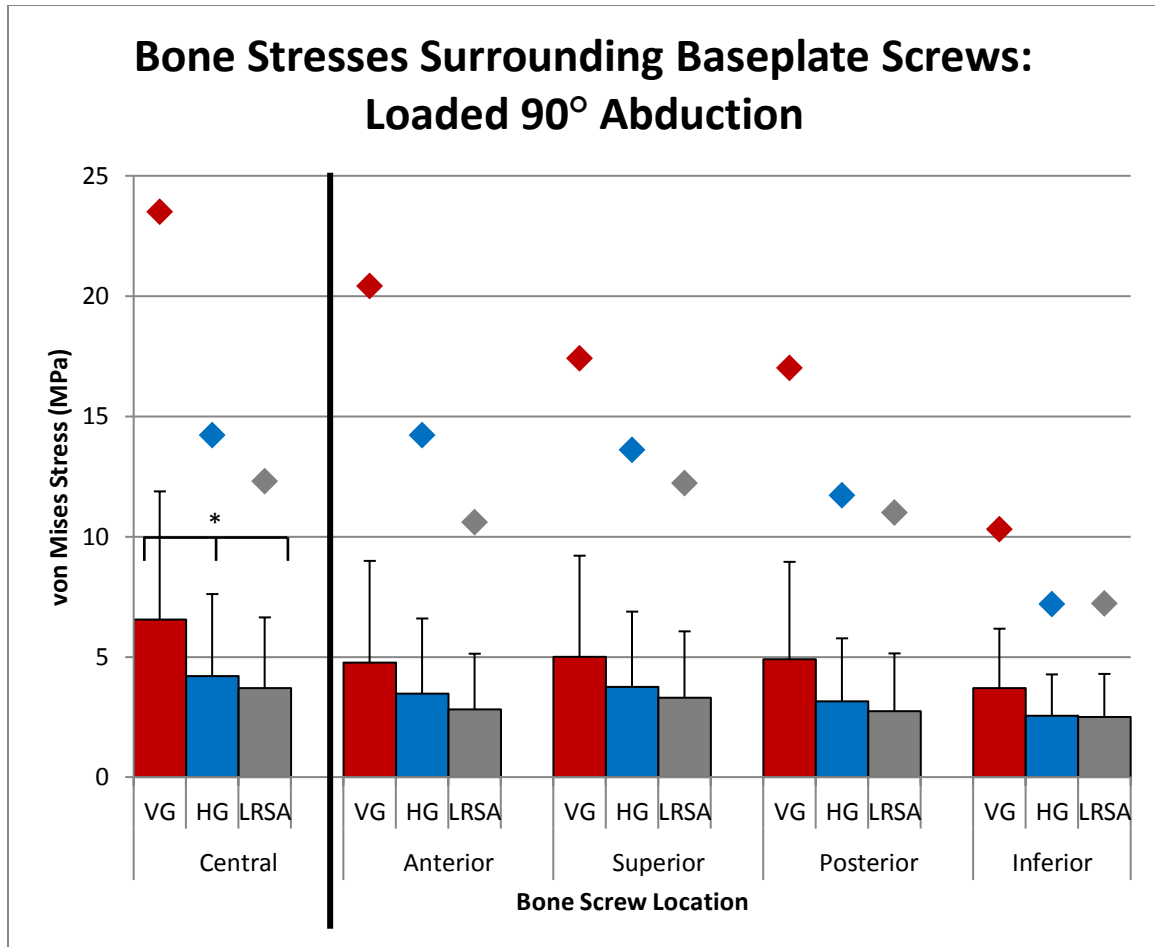


Figure 4.8: Glenoid Bone Stress: Loaded 90° Abduction

90th percentile bone stresses surrounding each bone screw grouped by bone screw location. Columns represent the average stress values, the whiskers represent the standard deviation, and the diamonds represent maximum values. Significant differences within the pairwise comparison of the stresses surrounding the central screw are designated with an asterisk ($p < 0.0005$).

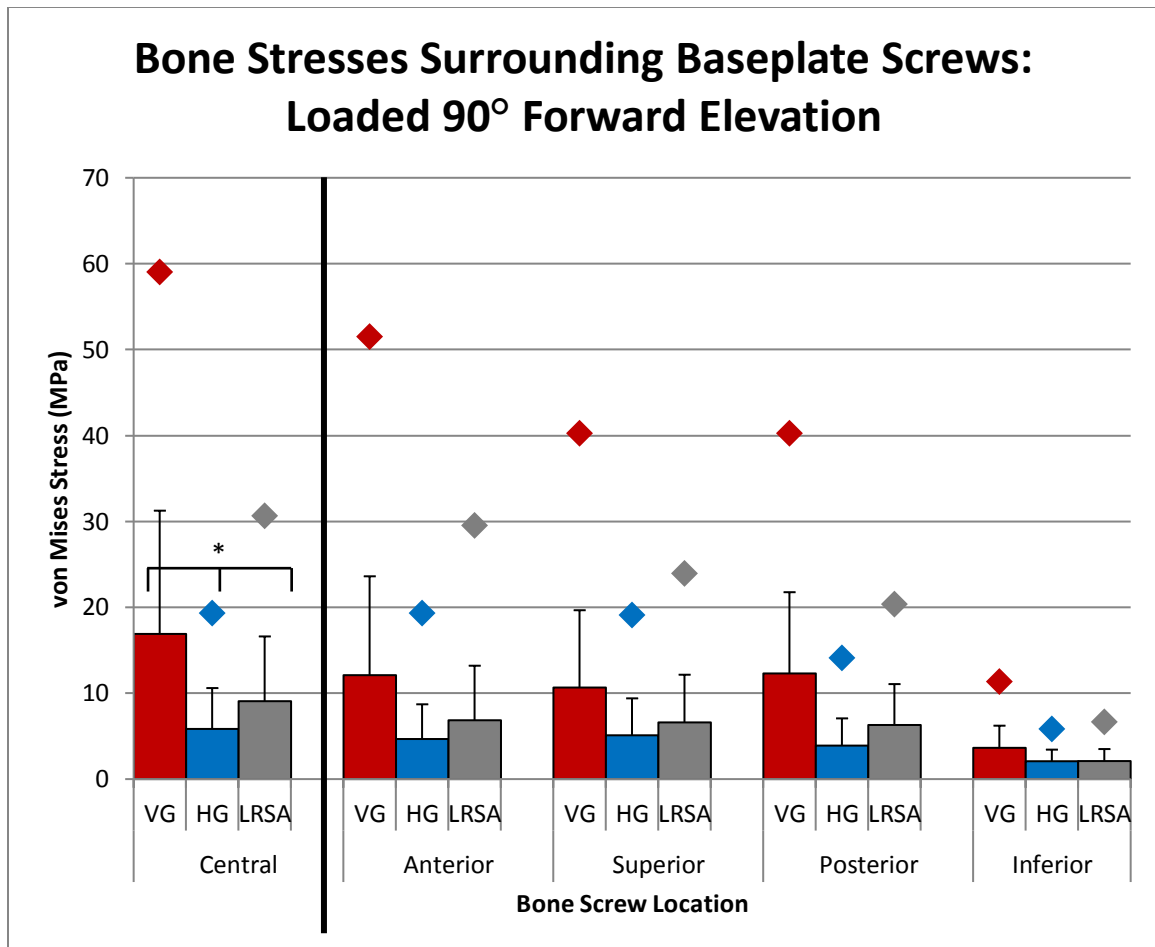


Figure 4.9: Glenoid Bone Stress: Loaded 90° Forward Elevation

90th percentile bone stresses surrounding each bone screw grouped by bone screw location. Columns represent the average stress values, the whiskers represent the standard deviation, and the diamonds represent maximum values. Significant differences within the pairwise comparison of the stresses surrounding the central screw are designated with an asterisk ($p < 0.0005$).

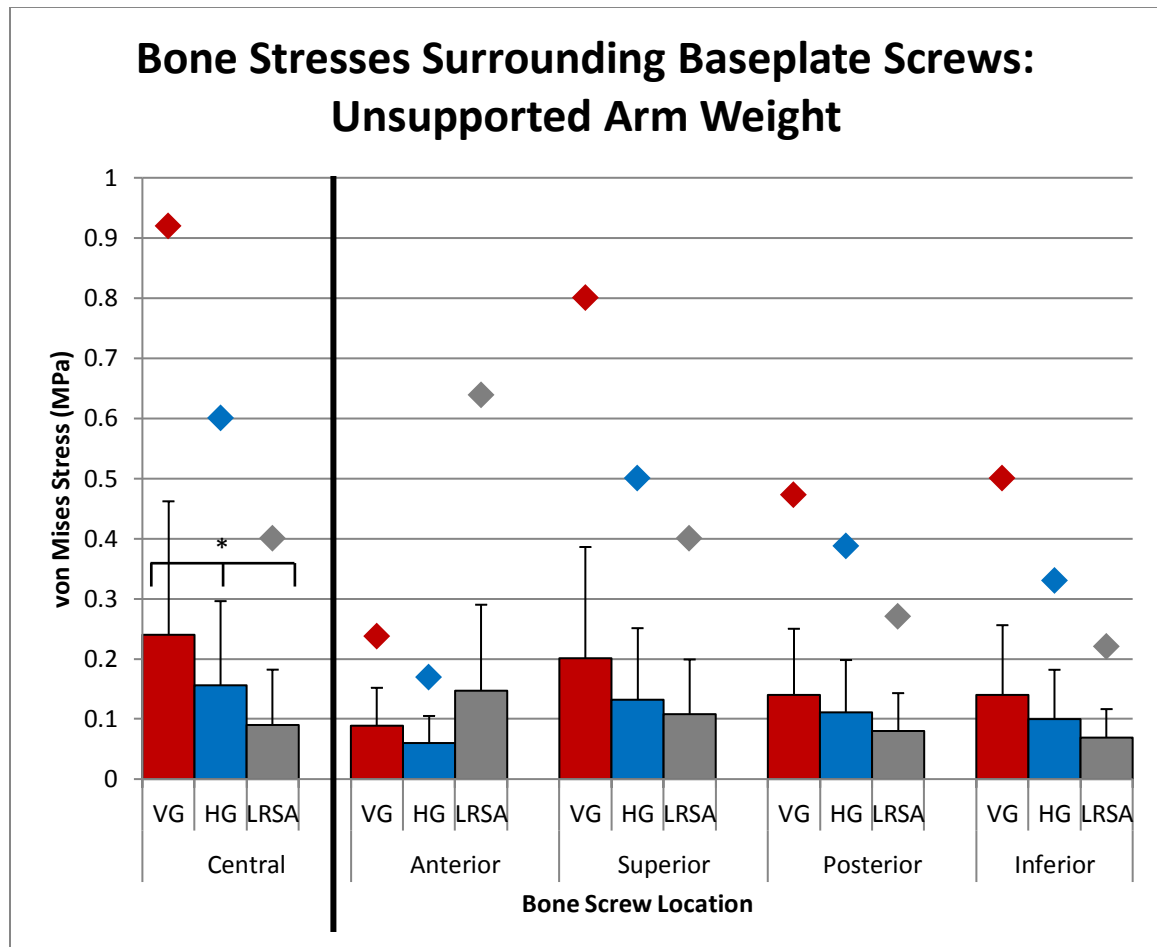


Figure 4.10: Glenoid Bone Stress: Unsupported Arm Weight

90th percentile bone stresses surrounding each bone screw grouped by bone screw location. Columns represent the average stress values, the whiskers represent the standard deviation, and the diamonds represent maximum values. Significant differences within the pairwise comparison of the stresses surrounding the central screw are designated with an asterisk ($p < 0.0005$).

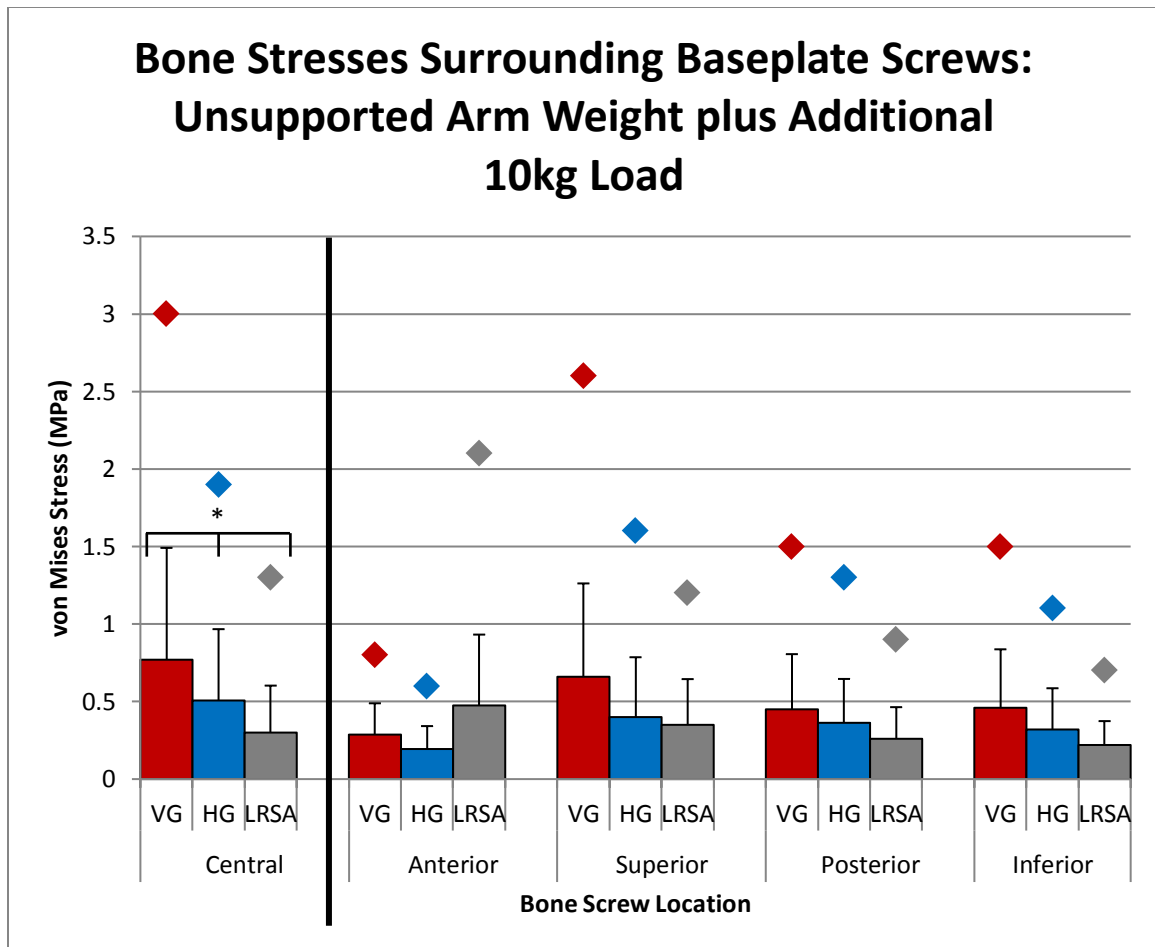


Figure 4.11: Glenoid Bone Stress: Unsupported Arm Weight plus 10 kg weight

90th percentile bone stresses surrounding each bone screw grouped by bone screw location. Columns represent the average stress values, the whiskers represent the standard deviation, and the diamonds represent maximum values. Significant differences within the pairwise comparison of the stresses surrounding the central screw are designated with an asterisk ($p < 0.0005$).

Except for the most extreme loading scenario of 90° forward elevation with a 2 kg weight in the hand, the average bone stresses stayed below the 10 MPa bone strength threshold. Localized maximum stresses exceeded the threshold in the 90° abduction cases (both 1BW and with 2 kg weight in the hand), indicating a risk of localized bone failure. Low demand loading cases (40° abduction, arm hanging at side with and without weight) resulted in low bone stresses, with no elements in the 90th percentile dataset exceeding the bone strength threshold.

4.4 Conclusions

The lateralization of the CoR in the vertical glenoid yoke consistently increased the bone stresses compared to the HG or LatRSA designs. The failure strength of bone (approximately 10 MPa), was exceeded in the more extreme loading scenarios, indicating substantial risk of fixation failure. These results suggest that patients with a linked implant should avoid activities that subject the joint to high loads, especially where bony ingrowth to the fixation interface is impaired.

Although the bone stresses between the HG and LatRSA implants were closer in value to each other than stresses resulting from the VG yoke, significant differences were found in bone stresses between the HG yoke and LatRSA for equivalent loading cases. With the exception of loaded 90° forward extension, the HG yoke resulted in higher bone stresses than the LatRSA, but the differences were less than 0.5 MPa. Although the VG provided superior ROM compared to the HG linked implant, the tradeoff between ROM and bone stresses may be tipped in favor of achieving better glenoid fixation, especially in patients with poor quality bone stock. In the most extreme loading case (loaded 90° FE) the stresses for HG were about half that for the VG. This is contrasted with a 10° overall penalty in RoM for the HG, noticed primarily in the posterior and forward elevation quadrants. This sacrifice may be needed to ensure reliable fixation in the glenoid. It is worth noting that the bone stresses with the linked HG implant were comparable to those of the commercial LatRSA implant.

This linked implant has been designed for patients with low functional demands, which correspond to lower stresses on the bone. The loading cases where bone stresses

approached or exceeded the 10 MPa bone strength threshold were considered worst case loading scenarios, and the patients of this device may not have the necessary muscular strength to perform them.

The contact properties of the implant and bone were modelled to reflect the initial fixation of the implant, where the peripheral screw threads are engaged with the trabecular bone, but prior to bony ingrowth on the central screw or back face. As the bone remodels to integrate into these surfaces, the fixation strength should improve.^{127,140}

The strengths of this study include creating a bone model that incorporates the spatial variation of mechanical properties of bone. Several authors have found that the central/posterior region of the glenoid is denser and stronger than other areas.^{125,147,148} This creates a more realistic model than a foam block or homogenous material properties assigned to all cortical and trabecular bone elements. Additionally, inclusion of a common clinical lateralized RSA model provided a clinically relevant baseline to compare results from the linked implant.

There were several limitations of this modelling study. A single non-pathologic, intact scapula was used, which is not representative of clinical revision cases, with compromised bone. This study should be repeated with clinical CT scans of several patients, since bone density and material properties are highly variable even within age-matched samples.^{146,148,149}

Determining an appropriate bone strength limit was difficult, given the wide range of reported experimental values. Average glenoid trabecular bone ultimate strength has been experimentally found as low as 1 MPa,¹²³ and as high as 67 MPa.¹⁴⁹ Anglin et al.¹⁴⁶ determined a mean trabecular bone strength of the glenoid of 10 MPa, which has been used as the bone allowable strength in several FE glenoid fixation studies.^{139,150} A uniform stress criterion of 10 MPa was used; a limitation of VM criteria is that it assumes isotropic material properties. Bone is not considered isotropic. However, VM stress incorporates the principal stresses into a single value. Additionally, since the purpose of this study was a comparison of bone stresses between different implant lateralizations, a relative stress measure was sufficient.

Additionally, a continuum model was used to represent the scapular trabecular bone, where in reality, this is a porous structure. The geometry of the trabecular structure has a major effect on the bone strength. Also, the cylindrical contact area modelled between the bone and screws does not fully represent the individual points of contact between the screws and trabeculae. Clinical CT scanner resolution and computational constraints limit the ability to perform a traditional FE analysis on trabecular bone interactions.

Future work could include using a larger selection of baseplate and screw configurations. Codsì et al.⁶¹ found screw positioning to have a significant effect on fixation strength. Ahir et al.¹³³ found that a fixed fulcrum shoulder with a single, oversized, coarse-threaded central screw that had some purchase into the cortical shell of the scapula allowed the stresses to be effectively dispersed through the stronger bone shell in FEA simulation. Upon analysis of a retrieved component, evidence of bone ingrowth to the threads was seen,¹³³ which bears promise for this linked implant design. Additionally, with more investigation into the optimal lateralization of the CoR on muscle loading, the yokes of the linked implant may be shortened which would reduce the moment arm of the load, thereby reducing bone fixation stresses.

In conclusion, bone stresses are influenced by the lateralization distance of the joint CoR. The additional CoR lateralization of the linked implants VG yoke resulted in bone stresses double that of HG or LatRSA in some loading conditions, and may exceed the bone failure strength in high loading scenarios. A linked implant with a horizontal glenoid yoke orientation produces bone stresses at the fixation interface similar to a commercial lateralized RSA implant.

Chapter 5

5 General Conclusions and Future Work

OVERVIEW: This chapter reviews the feasibility of the linked implant is discussed in terms of the objectives defined in Chapter 1. A summary of the computational models developed to test the performance of the proposed implant design is provided. The strengths and limitations of this work are discussed. Finally, future studies are proposed to further the evaluation of the proposed implant design.

5.1 Summary and General Discussion

Various shoulder replacement systems have been used to treat shoulder pathologies with generally successful outcomes.^{20,27,37} However, a small subset of patients continues to experience chronic shoulder instability after joint replacement, with higher risk identified in patients undergoing revision surgery and with severe rotator cuff deficiency. Surgical management of these cases is still unsatisfactory.^{40,45} With this population in mind, a linked shoulder implant based on a universal joint was designed to provide stability while restoring a normal range of motion.

The starting point of this analysis was the creation of the basic design of a linked implant (Chapter 2). Variable parameters were identified as the orientation of the glenoid yoke, the location of the glenoid yoke within the glenoid face, the tilt of the glenoid yoke with respect to the glenoid plane, and the offset distance of the hinges in the center trunnion. These parameters were varied to create 24 multiple configurations of the linked implant for a three-dimensional range of motion assessment. The ability to measure a 3D circumduction RoM in a repeatable protocol is an improvement on the 2D planar ROM assessments commonly reported clinically. Objective 1 was satisfied by several configurations of the implant achieving normal joint range of motion. The adduction/ abduction range of motion was limited only by the bony prominences of the shoulder, indicating that the implant itself will not impair joint motion. Cross-body joint angles exceeded the requirements to perform basic tasks of daily life.

Once it was determined that the linked implant was capable of restoring normal range of motion to the shoulder, it was then analyzed for static and fatigue stress in the context of clinically relevant activities of daily living. Chapter 3 indicated that the linkage had the mechanical integrity to withstand the expected loading of the joint based on measured joint loads. Stresses were highest in the humeral yoke component, but still well under the yield strength of the material. The minimum static factor of safety against yielding was found to be 1.6. The minimum factor of safety for fatigue failure under low angle abduction was found to be greater than 2, confirming the mechanical feasibility of the implant. Thus, Objective 2 was satisfied. Additionally, a cross-validation between a novel meshless analysis software (Simsolid) and traditional finite element analysis software (SolidWorks) was performed. No difference was found between the results generated from Simsolid and SolidWorks, which also serves as a validation of Simsolid.

Finally, Objective 3 was to evaluate the fixation of the implant to the glenoid bone using physiologically relevant loading scenarios. Using the same loading scenarios that the linkage components were subjected to, with the addition of the unsupported arm load, Chapter 4 compared the bone stresses generated within the glenoid between the proposed linked implant and an existing implant. This was done to predict a relative increase in fracture risk based on the lateralization distance of the center of rotation. The lateralization associated with the abduction hinge for the vertical glenoid yoke configuration with superior range of motion also resulted in approximately double the glenoid bone stresses compared to that of a commercial lateralized RSA implant used as a baseline. In light of these results, consideration should be given to a configuration that limits the lateralization of the center of rotation to a similar distance of a lateralized RSA. The horizontal glenoid yoke configuration maintains the CoR close to that of a lateralized RSA implant. Although the available RoM is on average 10° less than that of the vertical glenoid yoke, glenoid bone stresses around the central screw are an average of 0.5 MPa or 9% lower than for the lateralized RSA. The available range of motion still fulfills the joint angles required for activities of daily living.⁹²

Overall, the feasibility of this implant has been confirmed; normal range of motion can be restored, the implant can withstand high loads statically, and moderate loads in fatigue analysis, and bone fixation stresses are comparable to clinically used lateralized RSA implants.

5.2 Strengths and Limitations

One of the main strengths of this work was the parametric design that allowed the variability of parameters, and the ability to isolate the effects of these changes. The design of the implant was varied to test four different parameters on the circumduction range of motion. The repetition of testing across multiple bony models helped remove the influence of differing bony morphology on the range of motion.

Additionally, the loads used for finite element analysis were based on measured joint loads under physiologically relevant activities of daily living, increasing confidence that appropriate load magnitudes and directions were simulated. The results were then cross validated with two different software, to mitigate errors associated with mesh-based stress concentration effects, and due to simplifications of the boundary conditions.

The methodology of the glenoid bone fixation FEA involved individually mapped material properties to each element based on the CT scan density, which reflects the gradient of material properties found in human bone. This is considered a more realistic model than a homogenous foam block. Additionally, consistent screw placement was maintained between all cases to ensure that only load inputs and lateralization distances would affect the stress.

Since this implant was designed as a salvage procedure, it is likely that previous revision surgeries may compromise the glenoid bone quality. We used an intact, normal scapular bone for the fixation stress analysis instead of a specimen that had previously undergone shoulder replacement. Although this may include defects that are clinically relevant to revision surgery, the variability of defect size, positioning and severity encountered clinically is difficult to predict, or find a representative bone specimen. The study was

performed as a comparison based on lateralization distance of the CoR, thus the results are still transferable in different bone quality cases.

5.3 Future Work

The purpose of this work was to functionally analyze a parametric implant design of a linked shoulder implant to investigate the feasibility of this novel implant. As this functional analysis has yielded promising results in terms of restoring normal range of motion and withstanding physiologic joint loads, further testing and refinement of the implant is worthwhile to pursue in cadaver-based experiments.

To further investigate the effects of each variable parameter on the range of motion, a large sample size study using the same protocol could be performed across all configurations. This would allow a multi-way repeated measures ANOVA to be performed and isolate the effects of each variable parameter. Undertaking a study of this size would have been premature prior to completing this feasibility study, but would provide useful information as part of an iterative design process.

Additionally, a physical prototype of the linked implant will be created. This prototype will allow physical replication of the computational simulations performed in this work for validation. Strain gauges could be integrated to validate the results of the finite element analysis on component stresses. The components can be implanted in a cadaver model to assess the effects of soft tissue on the range of motion. For clinical testing, muscle wrapping and implant isolation will need to be addressed.

Furthermore, the stresses in the implant and glenoid fixation were evaluated based on anatomic loads, which were primarily generated by the deltoid and rotator cuff. The joint load may change based on the geometry of this implant and in cases of rotator cuff deficiency. The effects of these factors on joint loading should be assessed.

The linked implant is intended to be implemented within a protective boot that will isolate it from the body. The boot design should be developed now that the mechanical feasibility of the linked implant has been confirmed. As part of the boot design, muscle wrapping of the rotator cuff and deltoid need to be considered. Muscle wrapping may be compromised

by the amount of bone resected or bone defects arising from previous surgery. The virtual surgical technique used in this thesis may need to be revised in light of muscle attachment requirements. The design of the boot should also consider muscle wrapping; this may include incorporating anchors for muscle reattachment. The surgical technique and attachment anchors may affect the range of motion; thus, the boot design and muscle wrapping strategy should be developed in tandem.

5.4 Conclusion

The proposed linked implant is able to meet or exceed the normal range of motion, as measured from a bony model in circumduction. The implant is expected to withstand physiologically relevant loads without yielding based on finite element models of the linkage. The fixation stress in the glenoid bone should be comparable to that of a lateralized RSA system, depending on the chosen glenoid yoke orientation. A tradeoff between range of motion and fixation stress must be made depending on the quality of bone stock available at the time of surgery.

References or Bibliography

1. Howell SM, Galinat BJ, Renzi AJ, et al. Normal and abnormal mechanics of the glenohumeral joint in the horizontal plane. *J Bone Joint Surg Am* 1988; 70: 227–32.
2. Graichen H, Stammberger T, Bonel H, et al. Glenohumeral translation during active and passive elevation of the shoulder — a 3D open-MRI study. *J Biomech* 2000; 33: 609–613.
3. McClure PW, Michener LA, Sennett BJ, et al. Direct 3-dimensional measurement of scapular kinematics during dynamic movements in vivo. *J Shoulder Elb Surg* 2001; 10: 269–277.
4. Budge MD, Lewis GS, Schaefer E, et al. Comparison of standard two-dimensional and three-dimensional corrected glenoid version measurements. *J Shoulder Elbow Surg* 2011; 20: 577–83.
5. Itoi E, Motzkin NE, Morrey BF, et al. Scapular inclination and inferior stability of the shoulder. *J Shoulder Elb Surg* 1992; 1: 131–139.
6. Sugaya H, Moriishi J, Dohi M, et al. Glenoid rim morphology in recurrent anterior glenohumeral instability. *J Bone Joint Surg Am* 2003; 85–A: 878–84.
7. Terry GC, Chopp TM. Functional Anatomy of the Shoulder. *J Athl Train* 2000; 35: 248–255.
8. Sarrafia SK. Gross and Functional Anatomy of the Shoulder. *Clin Orthop Relat Res* 1983; 173: 11–19.
9. Edwards TB, Boulahia A, Walch G. Radiographic analysis of bone defects in chronic anterior shoulder instability. *Arthrosc J Arthrosc Relat Surg* 2003; 19: 732–739.
10. Lafosse L, Lejeune E, Bouchard A, et al. The Arthroscopic Latarjet Procedure for the Treatment of Anterior Shoulder Instability. *Arthrosc J Arthrosc Relat Surg* 2007; 23: 1–5.
11. Burkhart SS, De Beer JF, Barth JRH, et al. Results of Modified Latarjet Reconstruction in Patients With Anteroinferior Instability and Significant Bone Loss. *Arthrosc J Arthrosc Relat Surg* 2007; 23: 1033–1041.
12. Kim S-H, Ha K-I, Kim S-H. Bankart repair in traumatic anterior shoulder instability. *Arthrosc J Arthrosc Relat Surg* 2002; 18: 755–763.
13. Tauber M, Resch H, Forstner R, et al. Reasons for failure after surgical repair of anterior shoulder instability. *J Shoulder Elb Surg* 2004; 13: 279–285.

14. Hovelius LK, Sandström BC, Rösmark DL, et al. Long-term results with the Bankart and Bristow-Latarjet procedures: Recurrent shoulder instability and arthropathy. *J Shoulder Elb Surg* 2001; 10: 445–452.
15. Terrier A, Ramondetti S, Merlini F, et al. Biomechanical consequences of humeral component malpositioning after anatomical total shoulder arthroplasty. *J Shoulder Elbow Surg* 2010; 19: 1184–90.
16. de Groot JH, Brand R. A three-dimensional regression model of the shoulder rhythm. *Clin Biomech* 2001; 16: 735–743.
17. Ebaugh DD, McClure PW, Karduna AR. Three-dimensional scapulothoracic motion during active and passive arm elevation. *Clin Biomech* 2005; 20: 700–709.
18. Borich MR, Bright JM, Lorello DJ, et al. Scapular Angular Positioning at End Range Internal Rotation in Cases of Glenohumeral Internal Rotation Deficit relationship identifies a possible mechanism for development of excessive scapular anterior tilt. *J Orthop Sport Phys Ther* 2006; 36: 926–934.
19. Warner JJP, Micheli LJ, Arslanian LE, et al. Scapulothoracic Motion in Normal Shoulders and Shoulders with Glenohumeral Instability and Impingement Syndrome: A Study Using Moire Topographic Analysis. *Clin Orthop Relat Res* 1992; 285: 191–199.
20. Boileau P, Sinnerton RJ, Chuinard C, et al. Arthroplasty of the shoulder. *J Bone Joint Surg Br* 2006; 88: 562–75.
21. Farng E, Zingmond D, Krenek L, et al. Factors predicting complication rates after primary shoulder arthroplasty. *J Shoulder Elbow Surg* 2011; 20: 557–63.
22. Biomet Orthopedics Inc. *Comprehensive Total Shoulder System: Surgical Technique*. Warsaw, IN, USA. 2014.
23. Zimmer Inc. *Trabecular Metal Humeral Stem: Surgical Technique*. Warsaw, IN, USA. 2010.
24. Depuy Orthopaedics Inc. *Global Advantage Shoulder arthroplasty System: Surgical Technique*. 2000; 8–13.
25. DJO Surgical. *Surgical Technique: Reverse Shoulder Prosthesis*. 2005.
26. Cofield RH. Total shoulder arthroplasty with the Neer prosthesis. *J Bone Joint Surg Am* 1984; 66: 899–906.
27. Singh JA, Sperling JW, Cofield RH. Revision surgery following total shoulder arthroplasty: analysis of 2588 shoulders over three decades (1976 to 2008). *J Bone Joint Surg Br* 2011; 93: 1513–7.

28. Boileau P, Watkinson D, Hatzidakis AM, et al. The Grammont reverse shoulder prosthesis: Results in cuff tear arthritis, fracture sequelae, and revision arthroplasty. *J Shoulder Elb Surg* 2006; 15: 527–540.
29. Schoch BS, Barlow JD, Schleck C, et al. Shoulder arthroplasty for post-traumatic osteonecrosis of the humeral head. *J Shoulder Elbow Surg* 2016; 25: 406–412.
30. Westermann RW, Pugely AJ, Martin CT, et al. Reverse Shoulder Arthroplasty in the United States: A Comparison of National Volume, Patient Demographics, Complications, and Surgical Indications. *Iowa Orthop J* 2015; 35: 1–7.
31. Schairer W, Nwachukwu B, Lyman S, et al. National utilization of reverse total shoulder arthroplasty in the United States. *J Shoulder Elb Surg* 2015; 24: 91–97.
32. Gallo RA, Gamradt SC, Mattern CJ, et al. Instability after reverse total shoulder replacement. *J Shoulder Elb Surg* 2011; 20: 584–590.
33. Frankle M, Siegal S, Pupello D, et al. The Reverse Shoulder Prosthesis for glenohumeral arthritis associated with severe rotator cuff deficiency. A minimum two-year follow-up study of sixty patients. *J Bone Joint Surg Am* 2005; 87: 1697–705.
34. Kim SH, Wise BL, Zhang Y, et al. Increasing incidence of shoulder arthroplasty in the United States. *J Bone Joint Surg Am* 2011; 93: 2249–54.
35. Jobin CM, Brown GD, Bahu MJ, et al. Reverse total shoulder arthroplasty for cuff tear arthropathy: the clinical effect of deltoid lengthening and center of rotation medialization. *J Shoulder Elb Surg* 2012; 21: 1269–1277.
36. Hasan SS, Leith JM, Campbell B, et al. Characteristics of unsatisfactory shoulder arthroplasties. *J Shoulder Elb Surg* 2002; 11: 431–441.
37. Bohsali KI, Bois AJ, Wirth MA. Complications of Shoulder Arthroplasty. *J Bone Jt Surg* 2017; 99: 256–269.
38. Boileau P, Watkinson DJ, Hatzidakis AM, et al. Grammont reverse prosthesis: design, rationale, and biomechanics. *J Shoulder Elbow Surg* 2005; 14: 147S–161S.
39. Edwards TB, Williams MD, Labriola JE, et al. Subscapularis insufficiency and the risk of shoulder dislocation after reverse shoulder arthroplasty. *J Shoulder Elb Surg* 2009; 18: 892–896.
40. Chalmers BP, Wagner ER, Sperling JW, et al. Treatment and Outcomes of Reverse Shoulder Arthroplasty Dislocations. *J Shoulder Elb Arthroplast* 2017; 1: 1–6.
41. Zumstein MA, Pinedo M, Old J, et al. Problems, complications, reoperations, and revisions in reverse total shoulder arthroplasty: A systematic review. *J Shoulder Elb Surg* 2011; 20: 146–157.

42. Boileau P, Melis B, Duperron D, et al. Revision surgery of reverse shoulder arthroplasty. *J Shoulder Elb Surg* 2013; 22: 1359–1370.
43. Lädermann A, Williams MD, Melis B, et al. Objective evaluation of lengthening in reverse shoulder arthroplasty. *J Shoulder Elb Surg* 2009; 18: 588–595.
44. Clark JC, Ritchie J, Song FS, et al. Complication rates, dislocation, pain, and postoperative range of motion after reverse shoulder arthroplasty in patients with and without repair of the subscapularis. *J Shoulder Elb Surg* 2012; 21: 36–41.
45. Kohan EM, Chalmers PN, Salazar D, et al. Dislocation following reverse total shoulder arthroplasty. *J Shoulder Elb Surg* 2017; 26: 1238–1245.
46. Gutiérrez S, Walker M, Willis M, et al. Effects of tilt and glenosphere eccentricity on baseplate/bone interface forces in a computational model, validated by a mechanical model, of reverse shoulder arthroplasty. *J Shoulder Elb Surg* 2011; 20: 732–739.
47. Kontaxis A, Johnson GR. The biomechanics of reverse anatomy shoulder replacement – A modelling study. *Clin Biomech* 2009; 24: 254–260.
48. Langohr GD, Haverstock JP, Johnson JA, et al. Total Shoulder Arthroplasty Restores Shoulder Motion Levels Similar to the Contralateral Side. *Bone Jt Orthop Proc*; 98–B.
49. Coley B, Jolles BM, Farron A, et al. Arm position during daily activity. *Gait Posture* 2008; 28: 581–587.
50. Langohr GDG, Willing R, Medley JB, et al. Contact mechanics of reverse total shoulder arthroplasty during abduction: the effect of neck-shaft angle, humeral cup depth, and glenosphere diameter. *J Shoulder Elb Surg* 2016; 25: 589–597.
51. Terrier A, Merlini F, Pioletti DP, et al. Comparison of polyethylene wear in anatomical and reversed shoulder prostheses. *Bone Joint J* 2009; 91–B: 977–982.
52. Giles JW, Langohr GDG, Johnson JA, et al. Implant Design Variations in Reverse Total Shoulder Arthroplasty Influence the Required Deltoid Force and Resultant Joint Load. *Clin Orthop Relat Res* 2015; 473: 3615–3626.
53. Lädermann A, Denard PJ, Boileau P, et al. Effect of humeral stem design on humeral position and range of motion in reverse shoulder arthroplasty. *Int Orthop* 2015; 39: 2205–2213.
54. Stanmore Implants Worldwide Ltd. Bayley Walker Total Shoulder Replacement by Stanmore Implants <http://www.stanmoreimplants.com/bayley-walker-total-shoulder-replacement.php> (2016, accessed 28 June 2017).

55. Mohammed AA, Frostick SP. Linked shoulder replacement: current design problems and a new design proposal. *Musculoskelet Surg* 2016; 100: 25–29.
56. Wittig JC, Bickels J, Wodajo F, et al. Constrained Total Scapula Reconstruction after Resection of a High-Grade Sarcoma. *Clin Orthop Relat Res* 2002; 397: 143–155.
57. Fan H, Fu J, Li X, et al. Implantation of customized 3-D printed titanium prosthesis in limb salvage surgery: a case series and review of the literature. *World J Surg Oncol* 2015; 13: 308.
58. Cedars-Sinai <https://www.cedars-sinai.edu/Patients/Programs-and-Services/Imaging-Center/For-Physicians/Musculoskeletal-Radiology/Exhibits-and-Presentations/Imaging-Findings-Limb-Sparing-Surgery/Reconstruction-.aspx> (accessed 25 April 2017).
59. Schoch B, Schleck C, Cofield R, et al. Shoulder arthroplasty in patients younger than 50 years: min 20-year follow-up. *J Shoulder Elb Surg* 2015; 24: 705–710.
60. McGuire D, Vrettos B, Roche S, et al. Bone loss in shoulder replacement surgery: A review of current management. *SA Orthop J* 2012; 11: 47–55.
61. Codsí MJ, Iannotti JP. The effect of screw position on the initial fixation of a reverse total shoulder prosthesis in a glenoid with a cavitory bone defect. *J Shoulder Elb Surg* 2008; 17: 479–486.
62. Anglin C, Wyss UP, Nyffeler RW, et al. Loosening performance of cemented glenoid prosthesis design pairs. *Clin Biomech* 2001; 16: 144–150.
63. Mantripragada VP, Lecka-Czernik B, Ebraheim NA, et al. An overview of recent advances in designing orthopedic and craniofacial implants. *J Biomed Mater Res A* 2013; 101: 3349–64.
64. Orr TE, Carter DR. Stress analyses of joint arthroplasty in the proximal humerus. *J Orthop Res* 1985; 3: 360–71.
65. Scalise JJ, Iannotti JP. Bone Grafting Severe Glenoid Defects in Revision Shoulder Arthroplasty. *Clin Orthop Relat Res* 2008; 466: 139–145.
66. Vlachopoulos L, Dünner C, Gass T, et al. Computer algorithms for three-dimensional measurement of humeral anatomy: analysis of 140 paired humeri. *J Shoulder Elbow Surg* 2016; 25: 38–48.
67. Pruksakorn D, Chantarapanich N, Arpornchayanon O, et al. Rapid-prototype endoprosthesis for palliative reconstruction of an upper extremity after resection of bone metastasis. *Int J Comput Assist Radiol Surg* 2015; 10: 343–50.

68. Boileau P, Bicknell RT, Mazzoleni N, et al. CT scan method accurately assesses humeral head retroversion. *Clin Orthop Relat Res* 2008; 466: 661–9.
69. Nyffeler RW, L Werner CM, Simmen BR, et al. Analysis of a retrieved Delta III total shoulder prosthesis. *J Bone Jt Surg [Br]* 2004; 86B: 1187–91.
70. Mills A. Robert Hooke's 'universal joint' and its application to sundials and the sundial-clock. *Notes Rec* 2007; 61: 219–236.
71. Cadosch D, Chan E, Gautschi OP, et al. Metal is not inert: Role of metal ions released by biocorrosion in aseptic loosening-Current concepts. *J Biomed Mater Res Part A* 2009; 91A: 1252–1262.
72. Jacobs JJ. Loosening and Osteolysis Associated with Metal-on-Metal Bearings: A Local Effect of Metal Hypersensitivity? *J Bone Jt Surg* 2006; 88: 1171.
73. Liao Y, Hoffman E, Wimmer M, et al. CoCrMo metal-on-metal hip replacements. *Phys Chem Chem Phys* 2013; 15: 746–56.
74. Morwood MP, Garrigues GE. Shoulder arthroplasty in the patient with metal hypersensitivity. *J Shoulder Elb Surg* 2015; 24: 1156–1164.
75. Chebli C, Huber P, Watling J, et al. Factors affecting fixation of the glenoid component of a reverse total shoulder prosthesis. *J Shoulder Elb Surg* 2008; 17: 323–327.
76. Elwell J, Choi J, Willing R. Quantifying the competing relationship between adduction range of motion and baseplate micromotion with lateralization of reverse total shoulder arthroplasty. *J Biomech* 2017; 52: 24–30.
77. Harman M, Frankle M, Vasey M, et al. Initial glenoid component fixation in 'reverse' total shoulder arthroplasty: A biomechanical evaluation. *J Shoulder Elb Surg* 2005; 14: S162–S167.
78. Biomet Orthopedics Inc. Bio-Modular Choice Shoulder System: Surgical Technique.
79. SAE International. *Universal Joints and Driveshafts*. J901, 2000.
80. William HJ. *Boot for universal joints*. US2308073
Ahttps://www.google.com/patents/US2308073 (1940, accessed 22 March 2017).
81. Anstaett G, Klardie MR, Folsom AC, et al. *Implant module unit and rotating seal for prosthetic joint*. US5755807 Ahttps://www.google.com/patents/US5755807 (1996, accessed 17 August 2017).
82. Collier JP. *Enclosure member for prosthetic joint*. 4731088
Ahttps://www.google.com/patents/US4731088 (1986, accessed 17 August 2017).

83. DSM Biomedical. Elasthane™ Thermoplastic Polyether Polyurethane (TPU) (2012, accessed 25 August 2017).
84. DSM Biomedical. CarboSil® Thermoplastic Silicone Polycarbonate Polyurethane (TSPCU) (2012, accessed 25 August 2017).
85. DSM Biomedical. Bionate® Thermoplastic Polycarbonate Polyurethane (PCU) (2012, accessed 25 August 2017).
86. DSM Biomedical. BioSpan® Segmented Polyether Polyurethane (SPU) (2012, accessed 25 August 2017).
87. Iannotti JP, Spencer EE, Winter U, et al. Prosthetic positioning in total shoulder arthroplasty. *J Shoulder Elb Surg* 2005; 14: S111–S121.
88. Wu G, van der Helm F, Veeger HEJ, et al. ISB recommendation on definitions of joint coordinate systems of various joints for the reporting of human joint motion—Part II: shoulder, elbow, wrist and hand. *J Biomech* 2005; 38: 981–992.
89. Lempereur M, Leboeuf F, Brochard S, et al. In vivo estimation of the glenohumeral joint centre by functional methods: Accuracy and repeatability assessment. *J Biomech* 2010; 43: 370–374.
90. Wong MT, Langohr GDG, Athwal GS, et al. Implant positioning in reverse shoulder arthroplasty has an impact on acromial stresses. *J Shoulder Elb Surg* 2016; 25: 1889–1895.
91. Stryker Orthopaedics Inc. *Solar Total Shoulder System: Upper Extremity Surgical Protocol*. Warsaw, IN, USA, 2004.
92. Gates DH, Walters LS, Cowley J, et al. Range of Motion Requirements for Upper-Limb Activities of Daily Living. *Am J Occup Ther* 2016; 70: 1–10.
93. Elwell J, Athwal G, Willing R. Reverse Shoulder Arthroplasty neck-shaft angle and Glenoid Lateralisation have varied effects on global circumduction range of motion. In: *Journal of Bone and Joint Surgery*. British Editorial Society of Bone and Joint Surgery, pp. 111–111.
94. Harrold F, Wigderowitz C. A three-dimensional analysis of humeral head retroversion. *J Shoulder Elbow Surg* 2012; 21: 612–7.
95. Pearl ML. Proximal humeral anatomy in shoulder arthroplasty: Implications for prosthetic design and surgical technique. *J Shoulder Elbow Surg* 2005; 14: 99S–104S.
96. Knowles NK, Carroll MJ, Keener JD, et al. A comparison of normal and osteoarthritic humeral head size and morphology. *J Shoulder Elbow Surg* 2016; 25: 502–509.

97. Matsumura NN, Ogawa K, Kobayashi S, et al. Morphologic features of humeral head and glenoid version in the normal glenohumeral joint. *J Shoulder Elb Surg* 2014; 23: 1724–1730.
98. Nyffeler RW, Werner CML, Gerber C. Biomechanical relevance of glenoid component positioning in the reverse Delta III total shoulder prosthesis. *J Shoulder Elb Surg* 2005; 14: 524–528.
99. De Wilde LF, Berghs BM, VandeVyver F, et al. Glenohumeral relationship in the transverse plane of the body. *J Shoulder Elb Surg* 2003; 12: 260–267.
100. Yian EH, Ramappa AJ, Arneberg O, et al. The constant score in normal shoulders. *J Shoulder Elb Surg* 2005; 14: 128–133.
101. Barnes CJ, Van Steyn SJ, Fischer RA. The effects of age, sex, and shoulder dominance on range of motion of the shoulder. *J Shoulder Elb Surg* 2001; 10: 242–246.
102. Westerhoff P, Graichen F, Bender A, et al. In vivo measurement of shoulder joint loads during activities of daily living. *J Biomech* 2009; 42: 1840–1849.
103. Langohr GDG, Giles JW, Athwal GS, et al. The effect of glenosphere diameter in reverse shoulder arthroplasty on muscle force, joint load, and range of motion. *J Shoulder Elb Surg* 2015; 24: 972–979.
104. Burkhart SS, Morgan CD, Ben Kibler W. The disabled throwing shoulder: spectrum of pathology part III: the SICK scapula, scapular dyskinesis, the kinetic chain, and rehabilitation. *Arthrosc J Arthrosc Relat Surg* 2003; 19: 641–661.
105. Cawley J, Metcalf JE., Jones AH, et al. A tribological study of cobalt chromium molybdenum alloys used in metal-on-metal resurfacing hip arthroplasty. *J Wear* 2003; 255: 999–1006.
106. Antunes RA, de Oliveira MCL. Corrosion fatigue of biomedical metallic alloys: Mechanisms and mitigation. *Acta Biomater* 2012; 8: 937–962.
107. Bergmann G, Graichen F, Bender A, et al. In vivo gleno-humeral joint loads during forward flexion and abduction. *J Biomech* 2011; 44: 1543–1552.
108. Anglin C, Wyss UP. Arm motion and load analysis of sit-to-stand, stand-to-sit, cane walking and lifting. *Clin Biomech* 2000; 15: 441–448.
109. Charlton IW, Johnson GR. A model for the prediction of the forces at the glenohumeral joint. *Proc Inst Mech Eng Part H J Eng Med* 2006; 220: 801–812.
110. Poppen NK, Walker PS. Forces at the Glenohumeral Joint in Abduction. *Clin Orthop Relat Res* 1978; 135: 165–170.

111. Seherr-Thoss HC, Schmelz F, Aucktor E. *Universal Joints and Driveshafts: Analysis, Design, Applications*. 2nd ed. Berlin: Springer, 2006.
112. ABSSAC Ltd. Universal Joints | ABSSAC (2017, accessed 11 July 2017).
113. PT Motion. PTMotion - High Strength Universal Joints (accessed 11 July 2017).
114. Lakshmi Precision Screws Limited. Fastener Materials (2009, accessed 11 July 2017).
115. Holley Performance Products. Lakewood 23019 HIGH PERFORMANCE U-JOINTHolley Performance Products (2017, accessed 11 July 2017).
116. Bayrak Ö, Yetim AF, Alsaran A, et al. Fatigue life determination of plasma nitrided medical grade CoCrMo alloy. *Fatigue Fract Eng Mater Struct* 2010; 33: 303–309.
117. ASTM International. *Standard Specification for Wrought Cobalt-28Chromium-6Molybdenum Alloys for Surgical Implants (UNS R31537, UNS R31538, and UNS R31539)*. F1537, New York, 2011. Epub ahead of print 2011. DOI: 10.1520/F1537-11.
118. 3TRP. *Material Specification Cobalt Chrome Alloy Co28Cr6Mo*. 2015.
119. Anubis 3D. *Material Data Sheet: EOS Cobalt Chrome MP1 for EOSINT M 270*. 2010.
120. Namdari S, Goel DP, Romanowski J, et al. Principles of glenoid component design and strategies for managing glenoid bone loss in revision shoulder arthroplasty in the absence of infection and rotator cuff tear. *J Shoulder Elb Surg* 2011; 20: 1016–1024.
121. Couteau B, Mansat P, Estivalèzes É, et al. Finite element analysis of the mechanical behavior of a scapula implanted with a glenoid prosthesis. *Clin Biomech* 2001; 16: 566–575.
122. Galante J, Rostoker W, Ray RD. Physical properties of trabecular bone. *Calcif Tissue Res* 1970; 5: 236–246.
123. Kalouche I, Crépin J, Abdelmoumen S, et al. Mechanical properties of glenoid cancellous bone. *Clin Biomech* 2010; 25: 292–298.
124. Oftadeh R, Perez-Viloria M, Villa-Camacho JC, et al. Biomechanics and mechanobiology of trabecular bone: a review. *J Biomech Eng* 2015; 137: 1–15.
125. Li X, Williams P, Curry EJ, et al. Trabecular Bone Microarchitecture and Characteristics in Different Regions of the Glenoid. *Orthopedics* 2015; 38: e163–e168.

126. Prendergast P. Finite element models in tissue mechanics and orthopaedic implant design. *Clin Biomech* 1997; 12: 343–366.
127. Suárez DR, Weinans H, van Keulen F. Bone remodelling around a cementless glenoid component. *Biomech Model Mechanobiol* 2012; 11: 903–913.
128. Pomwenger W, Entacher K, Resch H, et al. Need for CT-based bone density modelling in finite element analysis of a shoulder arthroplasty revealed through a novel method for result analysis. *Biomed Tech* 2014; 59: 421–430.
129. Knowles NK, Reeves JM, Ferreira LM. Quantitative Computed Tomography (QCT) derived Bone Mineral Density (BMD) in finite element studies: a review of the literature. *J Exp Orthop* 2016; 3: 36.
130. Ford CM, Keaveny TM. The dependence of shear failure properties of trabecular bone on apparent density and trabecular orientation. *J Biomech* 1996; 29: 1309–1317.
131. Flatow EL, Harrison AK. A history of reverse total shoulder arthroplasty. *Clin Orthop Relat Res* 2011; 469: 2432–9.
132. Al-Hadithy N, Rumian AP. Reverse shoulder arthroplasty current concepts. *Orthop Trauma* 2013; 27: 312–321.
133. Ahir SP, Walker PS, Squire-Taylor CJ, et al. Analysis of glenoid fixation for a reversed anatomy fixed-fulcrum shoulder replacement. *J Biomech* 2004; 37: 1699–1708.
134. Pupello D. Origins of Reverse Shoulder Arthroplasty and Common Misconceptions. In: *Reverse Shoulder Arthroplasty*. Cham: Springer International Publishing, pp. 3–18.
135. Engh C, O'Connor D, Jasty M, et al. Quantification of Implant Micromotion, Strain Shielding, and Bone Resorption with Porous-Coated Anatomic Medullary Locking Femoral Prostheses. *Clin Orthop Relat Res* 1992; 13–29.
136. Taddei F, Pancanti A, Viceonti M. An improved method for the automatic mapping of computed tomography numbers onto finite element models. *Med Eng Phys* 2004; 26: 61–69.
137. Eberle S, Göttlinger M, Augat P. An investigation to determine if a single validated density–elasticity relationship can be used for subject specific finite element analyses of human long bones. *Med Eng Phys* 2013; 35: 875–883.
138. Virani NA, Harman M, Li K, et al. In vitro and finite element analysis of glenoid bone/baseplate interaction in the reverse shoulder design. *J Shoulder Elb Surg* 2008; 17: 509–521.

139. Denard PJ, Lederman E, Parsons BO, et al. Finite element analysis of glenoid-sided lateralization in reverse shoulder arthroplasty. *J Orthop Res* 2017; 35: 1548–1555.
140. Nigro PT, Gutiérrez S, Frankle MA. Improving glenoid-side load sharing in a virtual reverse shoulder arthroplasty model. *J Shoulder Elb Surg* 2013; 22: 954–962.
141. Clauser CE, McConville JT, Young JW. *Weight, Volume, and Center of Mass of Segments of the Human Body*. AD-710 622, 1969.
142. Geraldles DM, Hansen U, Amis AA. Parametric analysis of glenoid implant design and fixation type. *J Orthop Res* 2017; 35: 775–784.
143. Birmingham E, Grogan JA, Niebur GL, et al. Computational Modelling of the Mechanics of Trabecular Bone and Marrow Using Fluid Structure Interaction Techniques. *Ann Biomed Eng* 2013; 41: 814–826.
144. Goff MG, Chang KL, Litts EN, et al. The effects of misalignment during in vivo loading of bone: Techniques to detect the proximity of objects in three-dimensional models. *J Biomech* 2014; 47: 3156–3161.
145. Fitzpatrick CK, Clary CW, Cyr AJ, et al. Mechanics of post-cam engagement during simulated dynamic activity. *J Orthop Res* 2013; 31: 1438–1446.
146. Anglin C, Tolhurst P, Wyss UP, et al. Glenoid cancellous bone strength and modulus. *J Biomech* 1999; 32: 1091–1097.
147. Lim D, Kim H-S, Kim J-S, et al. Mapping of the morphological and the material characteristics on the glenoid and estimation of predominant loading condition on the glenoid through the mapping. *J Mech Sci Technol* 2009; 23: 409–419.
148. Mansat P, Barea C, Hobatho MC, et al. Anatomic variation of the mechanical properties of the glenoid. *J shoulder Elb Surg* 1998; 7: 109–15.
149. Frich LH, Jensen NC, Odgaard A, et al. Bone strength and material properties of the glenoid. *J Shoulder Elb Surg* 1997; 6: 97–104.
150. Wee H, Armstrong AD, Flint WW, et al. Peri-implant stress correlates with bone and cement morphology: Micro-FE modeling of implanted cadaveric glenoids. *J Orthop Res* 2015; 33: 1671–1679.
151. Budynas RG, Nisbett JK. *Shigley's Mechanical Engineering Design*. 9th ed. New York City: McGraw Hill, 2008.
152. Leake J, Borgeson JL. *Engineering Design Graphics: Sketching, Modeling, and Visualization: APPENDIX B: ANSI PREFERRED METRIC LIMITS AND FITS*. 2nd ed. Hoboken, NJ: Wiley, 2012.

Appendix A - Glossary of Medical Terms

OVERVIEW: This appendix lists and defines common medical terminology that is relevant to the work of this thesis.

Anterior	Towards the front; opposite posterior
Arthroplasty	Surgical replacement of a joint
Cortical	Hard bone, typically the outer layer of bone
Distal	Relative term reflecting a farther position from the reference point, such as the center of the body
Excise	To remove
Frontal	Plane passing through the body in the medial -lateral direction
Implant	An artificial component surgically installed in the body
Inferior	Relative term reflecting a position below the point of reference
Instability	The inability to maintain a normal joint relationship between the humeral head and the glenoid
Intraoperative	During surgery
<i>In-vitro</i>	Latin translation “in death”. Refers to within a cadaveric specimen
<i>In-vivo</i>	Latin translation “in life”. Refers to within a living subject
Joint	The contact of two or more bones, typically the point of relative motion
Landmarks	Easily recognizable features of bone
Lateral	Refers to a position farther from the sagittal plane (midline) of the body
Ligament	Fibrous tissue connecting bones or cartilage, provides strength and stability to the joint
Medial	Refers to a position towards the sagittal plane of the body
Morphology	Refers to the shape or form of a structure
Muscle	Organ that contracts to effect joint motion

Muscle moment arm	The orthogonal distance from the muscle origin to the axis of rotation
Osteolysis	Pathologic resorption of bone
Physiological	Normal, biological, not pathologic
Posterior	Toward the back; opposite anterior
Prosthesis	An artificial component that replaces a part of the body
Proximal	Relative term reflecting a closer position to the reference point, such as the center of the body
Resorption	Dissolution of a tissue
Sagittal	Plane passing through the body in the anterior -posterior direction
Superior	Relative term reflecting a position above the point of reference
Tendon	Connective tissue that joins muscle to bone or cartilage
Trabecular	Porous inner bone
Transverse	Horizontal plane passing through midline of the body

Appendix B – Detailed Part Drawings of Linked Implant

OVERVIEW: This appendix contains a complete set of manufacturing drawings for the components of the linked shoulder implant.

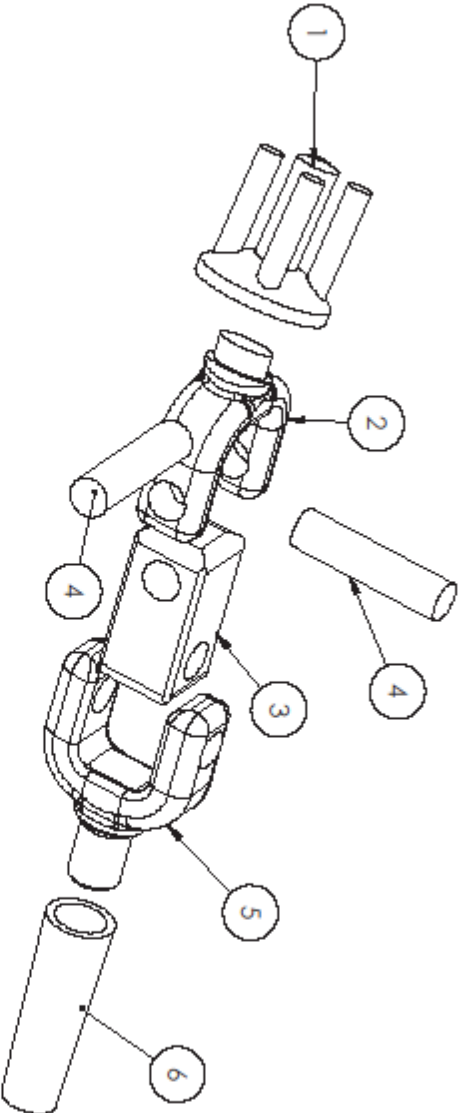
Drawing Number	Description
A_1	Exploded view of the linkage assembly
GY_1	Part drawing of glenoid yoke
CT_1	Part drawing of center trunnion
P_1	Part drawing of pin
HY_1	Part drawing of humeral yoke
HS_1	Part drawing of humeral shaft

2

1

B

A



ITEM NO.	DESCRIPTION	QTY.
1	GLENOID BASEPLATE	1
2	GLENOID YOKE	1
3	CENTER TRUNNION	1
4	PIN	2
5	HUMERAL YOKE	1
6	HUMERAL SHAFT	1

DRAWN

EW

06/17

CHECKED

BUCA/PR

WFO/PR

Q.A.

COMMENTS:

TITLE:

Linked Implant

SIZE

DWG. NO.

SCALE: 1:5

WEIGHT:

SHEET 1 OF 1

REV

A

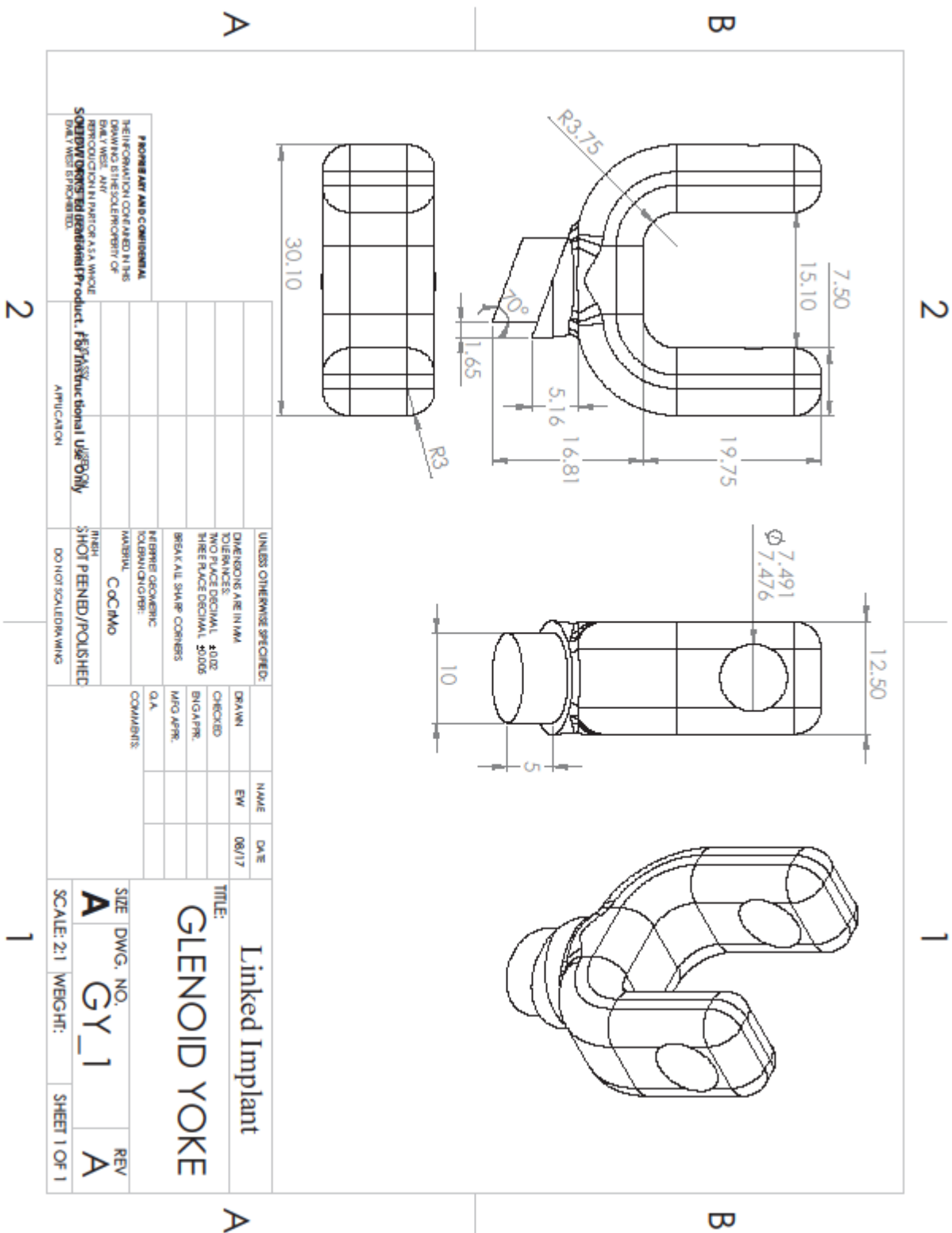
THE INFORMATION CONTAINED IN THIS DRAWING IS THE SOLE PROPERTY OF SOLIDWORKS EDUCATIONAL PRODUCT. FOR INSTRUCTIONAL USE ONLY. NO OTHER REPRODUCTION OR TRANSMISSION OF THIS DRAWING IS PERMITTED.

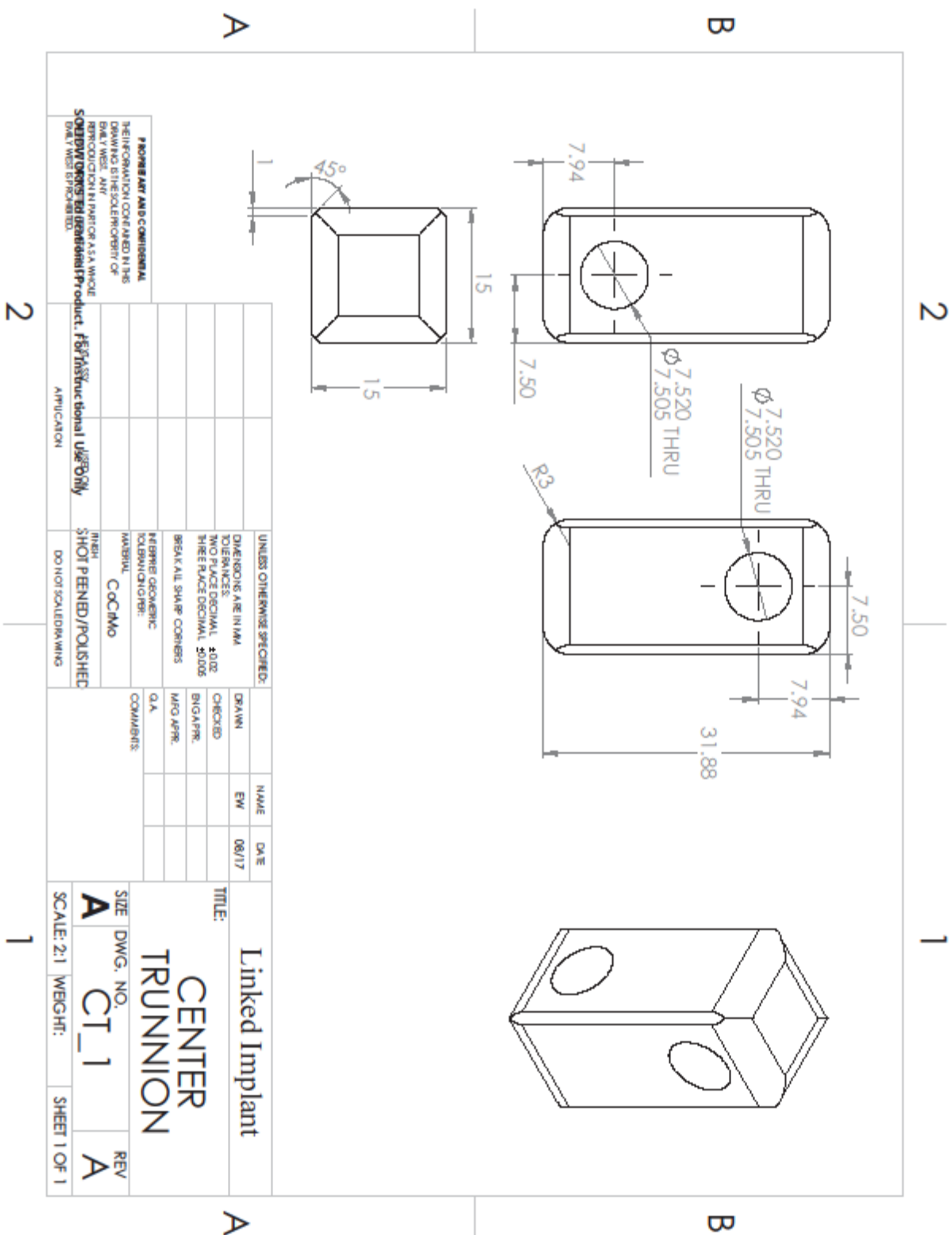
2

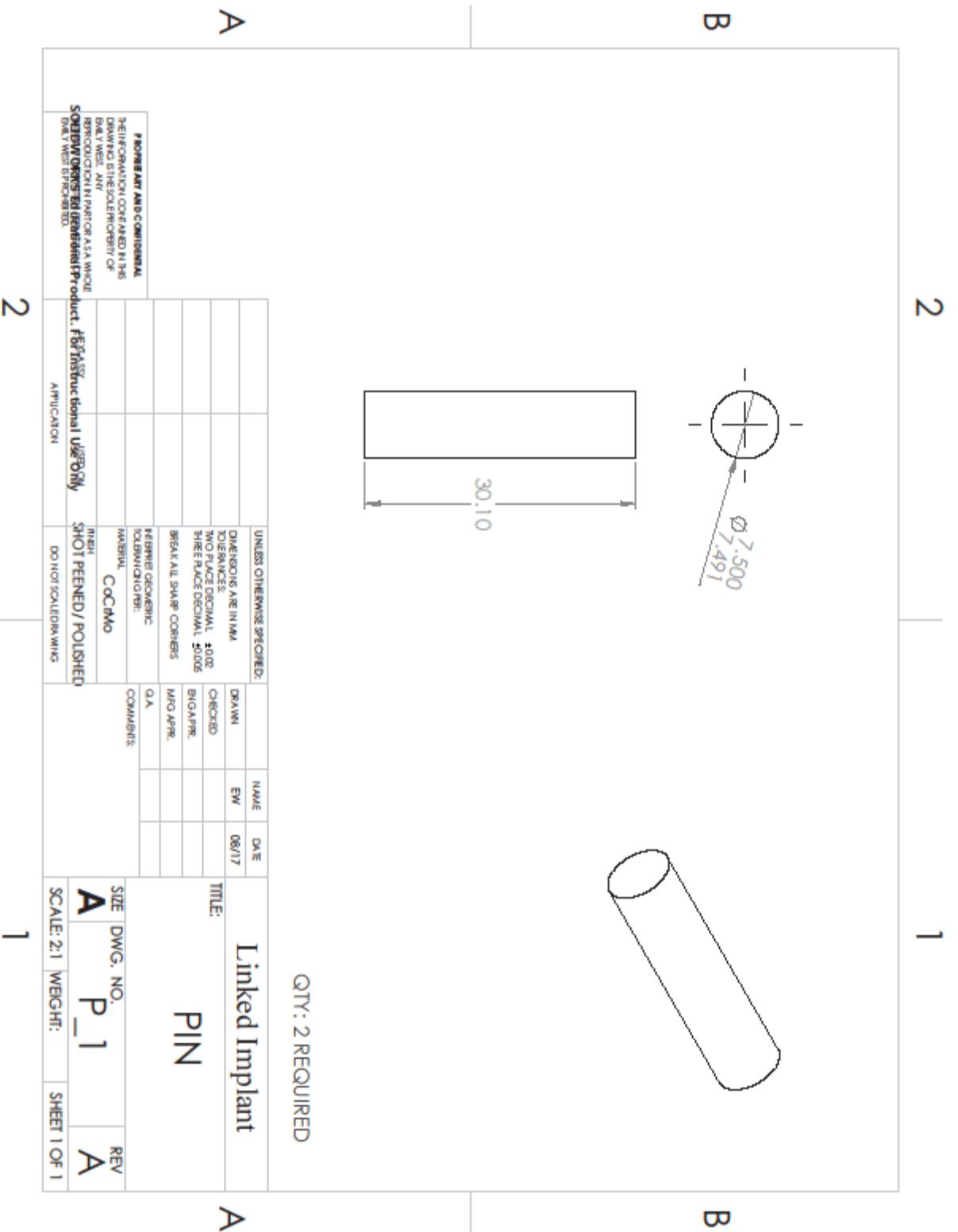
1

B

A







Appendix C – Individual Range of Motion Plots for 6 Repeated Configurations

OVERVIEW: The following reports the mean joint angle for each of the 6 configurations repeated within 3 specimens. The joint angle was measured and plotted at 30 points along the circumduction profile. This data was collected and presented consistent with the method described in Chapter 2.

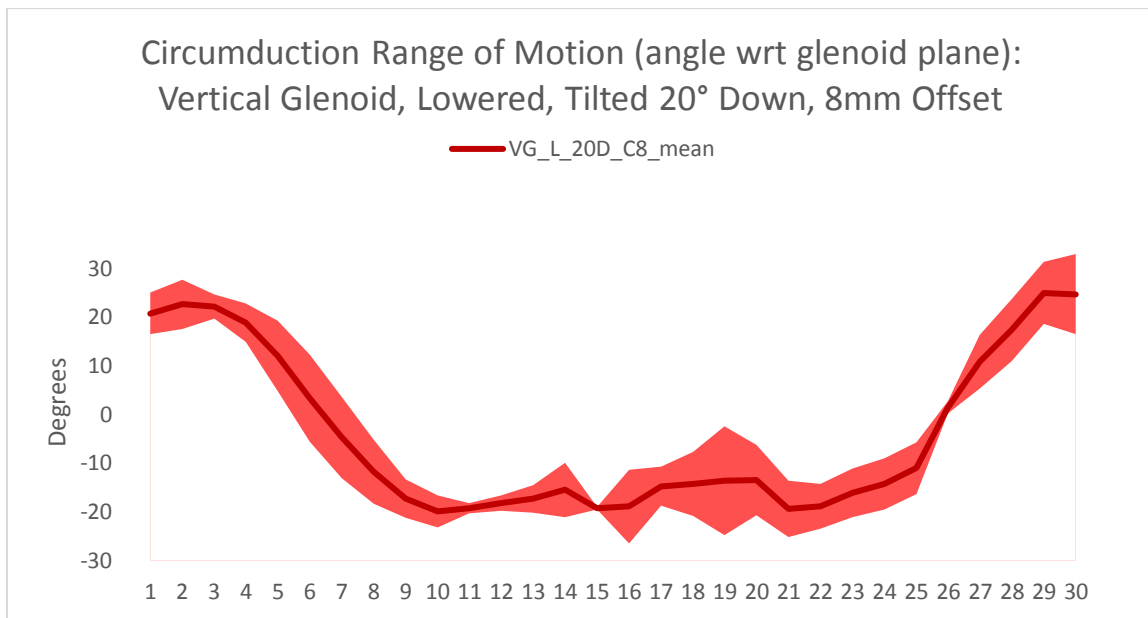


Figure C.1: Circumduction RoM for configuration 1

The joint angle is averaged between three sizes of specimens tested. Dark line represents mean joint angle, with the shaded band depicting one standard deviation on either side of the mean value.

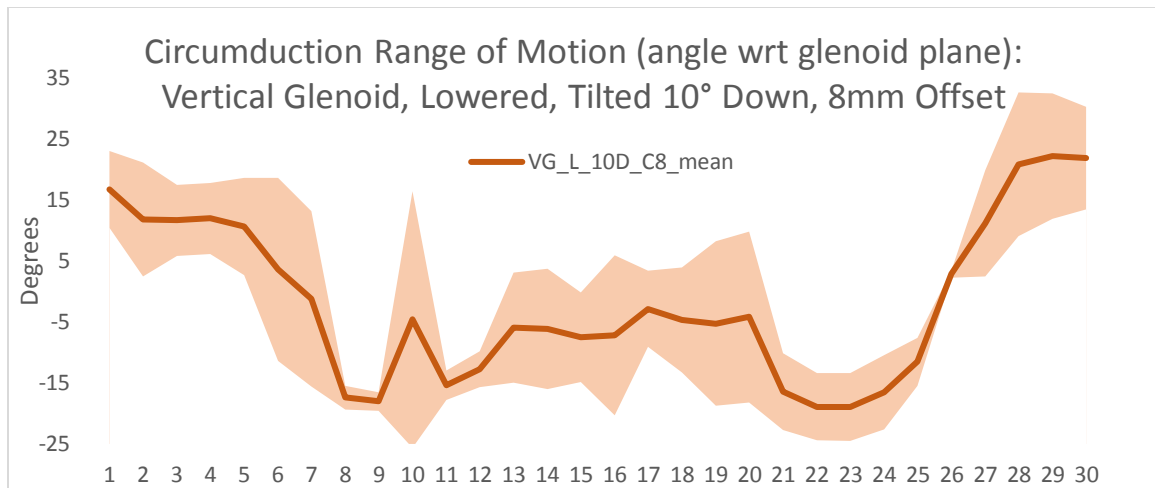


Figure C.2: Circumduction RoM for configuration 2

The joint angle is averaged between three sizes of specimens tested. Dark line represents mean joint angle, with the shaded band depicting one standard deviation on either side of the mean value.

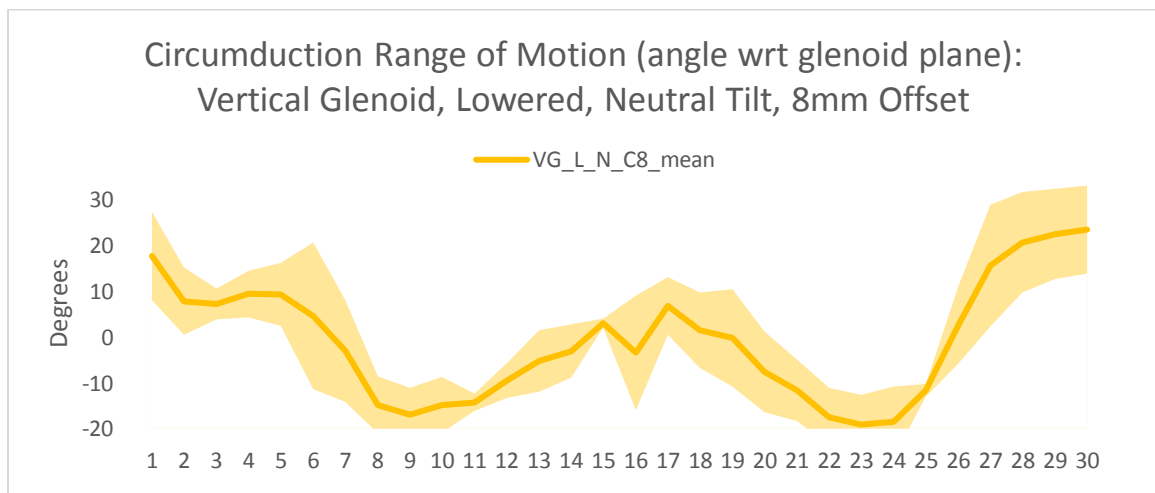


Figure C.3: Circumduction RoM for configuration 3

The joint angle is averaged between three sizes of specimens tested. Dark line represents mean joint angle, with the shaded band depicting one standard deviation on either side of the mean value.

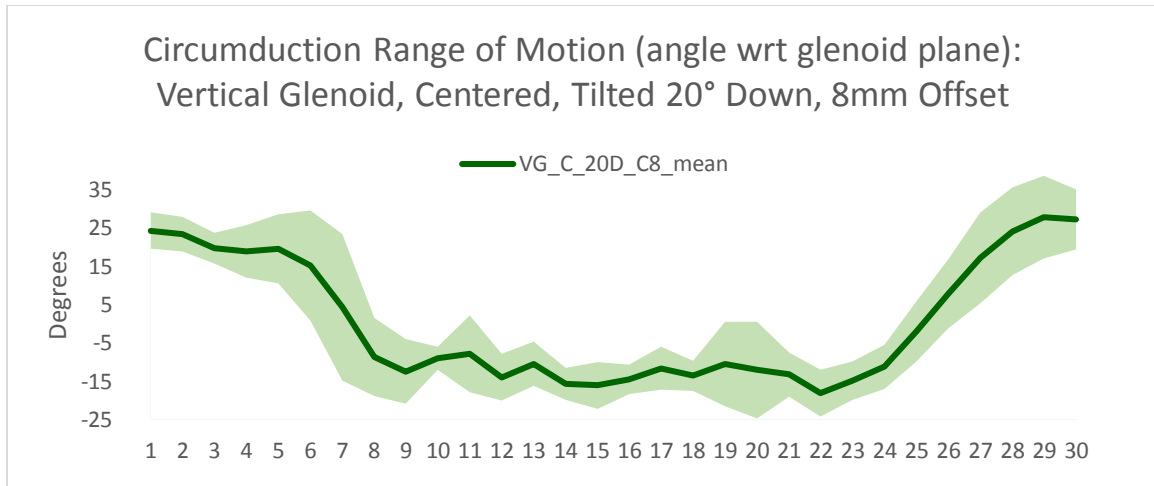


Figure C.4: Circumduction RoM for configuration 4

The joint angle is averaged between three sizes of specimens tested. Dark line represents mean joint angle, with the shaded band depicting one standard deviation on either side of the mean value.

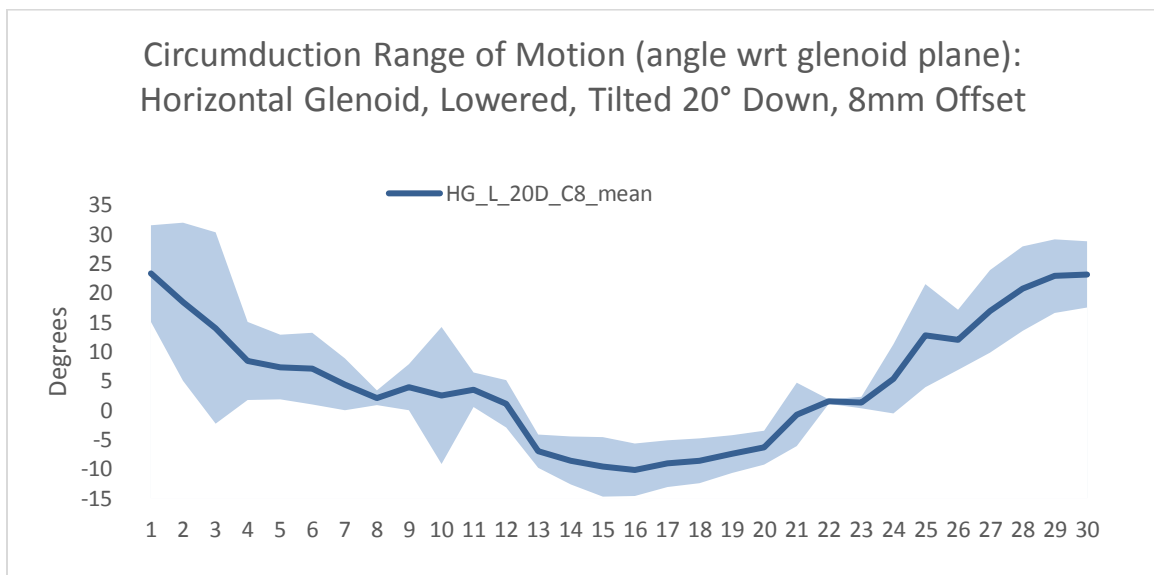


Figure C.5: Circumduction RoM for configuration 5

The joint angle is averaged between three sizes of specimens tested. Dark line represents mean joint angle, with the shaded band depicting one standard deviation on either side of the mean value.

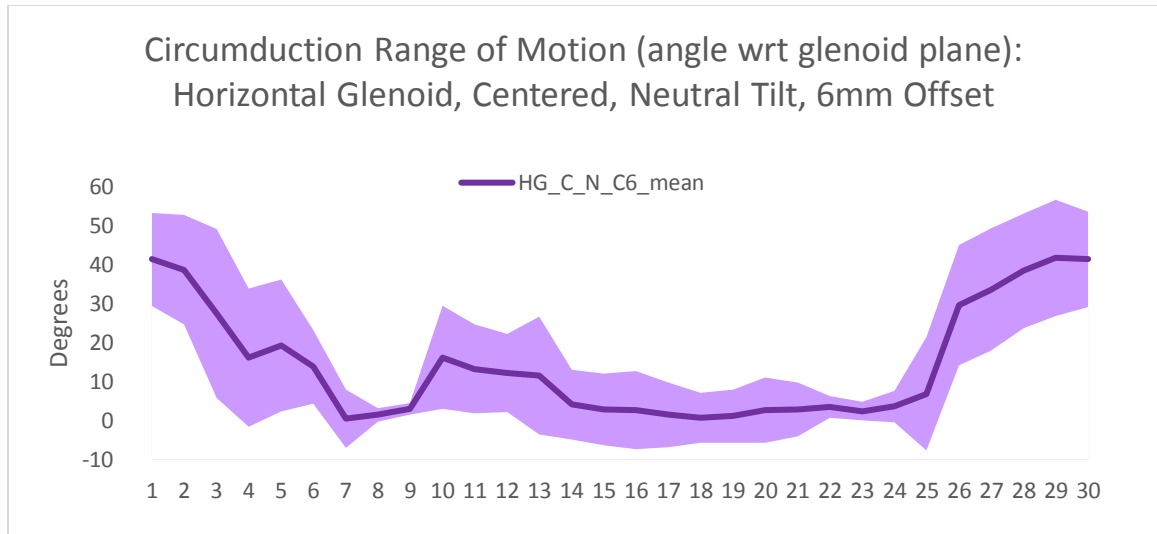


Figure C.6: Circumduction RoM for configuration 6

The joint angle is averaged between three sizes of specimens tested. Dark line represents mean joint angle, with the shaded band depicting one standard deviation on either side of the mean value.

Appendix D: Tolerance Calculations for Pin and Center Trunnion

OVERVIEW: Appendix D presents the tolerance calculations of the pin and center trunnion used to evaluate Hertzian contact stress between these components.

Tolerance was calculated using shaft basis to allow a press fit between the pin and the yokes, and a sliding fit between the pin and center trunnion. The minimum and maximum dimensions for each feature are presented in Table 1.

Pin – Center Trunnion

A sliding fit (G7/h6) was chosen as it is the recommended fit for low speed sliding surfaces, and since it most closely replicates a journal bearing.¹⁵¹

Pin – Yoke

A press fit will be employed between the pin and yoke holes to retain the pins in place without the need for a retaining ring or cap. A locational interference fit (p7/h6) was chosen since there are no requirements to transmit axial torque, simply to hold the pin so that the trunnion may rotate around it.

Based on the chosen tolerances, the maximum and minimum diameters for each component may be determined by adding / subtracting the relevant deviation. Deviation values were taken from ANSI B4.2-1978: Preferred Metric Limits and Fits.¹⁵²

Table D.1: Tolerance Dimensions for Pin, Center Trunnion, and Yoke holes

Component	Fit	Nominal Diameter (mm)	Minimum Diameter (mm)	Maximum Diameter (mm)
Pin	XX/h6	7.5	7.491	7.500
Block hole	G7/h6	7.5	7.505	7.520
Yoke hole	P7/h6	7.5	7.476	7.491

Appendix E: Hertzian Contact Stress Calculations

OVERVIEW: The following reports the calculation of Hertzian contact stress between the pin and center trunnion. The calculations are based on a worst case scenario, using the highest radial mismatch between the pin and center trunnion based on the tolerances calculated in Appendix D. The loading case used was loaded 90° forward elevation with a 2 kg weight in the hand, representing the most aggressive loading scenario.

Table E.1: Variables used for Hertzian contact stress calculations

Variable	Meaning	Value	Units
b	Half width of contact area between 2 cylinders	1.077	mm
l	Length of contact area between 2 cylinders	15	mm
F	Force compressing the 2 cylinders	1700	N
ν	Poisson's ratio	0.3	-
E	Young's Modulus	220	GPa
d_1	Diameter of inner cylinder	7.491	mm
d_2	Diameter of surrounding cylindrical surface	7.520	mm

Note that the subscripts differentiate between the inner cylinder and the surrounding cylindrical surface. For the case of nested cylinders, the d of the internal cylinder is taken as negative.¹⁵¹

The diameters listed above reflect the largest radial mismatch between the pin and corresponding hole in the center trunnion block, thus representing the worst case scenario. The half-width of the contact area is calculated as:

$$b = \sqrt{\frac{2F(1 - \nu_1^2)/E_1 + (1 - \nu_2^2)/E_2}{\pi l \left(\frac{1}{d_1} + \frac{1}{d_2} \right)}} \quad (\text{E.1})$$

The maximum pressure at the contact surface is calculated by equation E.2:

$$p_{max} = \frac{2F}{\pi bl} = 67 \text{ MPa} \quad (\text{E.2})$$

The maximum shear stress occurs beneath the contact surface and is given by:

$$\tau_{max} = 0.3p_{max} = 20.1 \text{ MPa} \quad (\text{E.3})$$

Appendix F: Fatigue Calculations

OVERVIEW: The following reports the calculation of fatigue safety factor in the humeral yoke under fluctuating stress conditions. The loading case used was unloaded 40° abduction.

S-N curves are developed using alternating stress conditions (the test specimen alternates between tension and compression, with the mean stress equal to zero). At low level abduction, the components of the universal joint will fluctuate from minimal stress to a maximal stress value (as calculated in Chapter 3), but will not experience stress reversal from tension to compression. Therefore, adjustments must be made in the fatigue calculations to reflect the fluctuating loading conditions.¹⁵¹

The modified Goodman fatigue criteria was used, after adjusting the fatigue limit published by Bayrak et al.¹¹⁶ for the Marin factors. Relevant equations and intermediate values are presented in Table F.1, calculated according to the methods set out by Shigley et al.¹⁵¹ The minimum factor of safety against fatigue failure based on an infinite lifetime at low angle abduction is 2.2.

Table F.1: Fatigue Calculations and Intermediate Values

Name	Formula	Intermediate values	Equation number
Corrected Endurance Strength	$S_e = K_a k_b k_c K_d K_e K_f S'_e$ $S_e = 426 \text{ MPa}$	$S'_e = 624 \text{ MPa}$	(F.1)
Surface Factor (ground)	$k_a = a(S_{UTS})^b$ $k_a = 0.86$	$a = 1.58$ $b = -0.107$ $S_{UTS} = 1300 \text{ MPa}$	(F.2)
Size Factor	$k_b = 1.24d^{-0.107}$ $k_b = 0.975$	$d = 9.5 \text{ mm}$	(F.3)
Loading Factor	$k_c = 1$	Bending stress	
Temperature Factor	$k_d = 1$	Operates below 40°C	
Reliability Factor	$k_e = 0.814$	99% reliability	
Miscellaneous Effects Factor	$k_f = 1$	Undetermined	
Midrange Stress	$\sigma_m = \frac{1}{2}(\sigma_{max} - \sigma_{min})$ $\sigma_m = 85 \text{ MPa}$	Stresses from FEA in Ch 3 (humeral yoke)	(F.4)
Alternating Stress	$\sigma_a = \sigma_{max}$ $\sigma_a = 170 \text{ MPa}$	Stresses from FEA in Ch 3 (humeral yoke)	(F.5)
Factor of Safety	$n_f = \frac{1}{\frac{\sigma_a}{S_e} + \frac{\sigma_m}{S_{UTS}}}$ $n_f = 2.2$	Modified Goodman	(F.6)

Appendix G: Glenoid Bone Fixation Stress

OVERVIEW: The following reports the tabulated values for mean and maximum glenoid bone stress based on cutoff thresholds of the 90th percentile, 95th percentile, and 99th percentile. Stresses are presented for each bone screw in the glenoid.

Table G.1: Central Screw Bone Stresses

Hinge lateralization	90 th Percentile		95 th Percentile		99 th Percentile	
Central Screw	Mean σ (MPa)	Max σ (MPa)	Mean σ (MPa)	Max σ (MPa)	Mean σ (MPa)	Max σ (MPa)
1 Body Weight Shear and Compressive Load						
LatRSA	3.4	15.4	4.2	20.4	5.1	32.0
HG	3.7	16.8	4.5	22.9	5.5	36.0
VG	4.8	21.4	5.8	28.5	7.0	43.5
Unloaded 40° Abduction						
LatRSA	1.4	6.0	1.7	8.1	2.0	12.5
HG	1.6	6.8	1.9	9.3	2.3	14.1
VG	2.1	9.5	2.6	11.6	3.1	17.4
Loaded 90° Abduction						
LatRSA	3.7	12.3	4.3	23.6	5.4	36.1
HG	4.2	14.2	5.0	28.9	6.3	47.8
VG	6.6	23.5	7.8	44.5	10.0	76.7
Loaded 90° Forward Elevation						
LatRSA	9.1	30.6	10.7	51.2	13.3	102.2
HG	5.8	19.3	6.9	37.5	8.7	64.9
VG	16.9	59.0	20.1	99.3	25.3	202.6
Unloaded Arm Hanging at Side						
LatRSA	0.1	0.4	0.1	0.6	0.1	0.7
HG	0.2	0.6	0.2	0.8	0.2	1.4
VG	0.2	0.9	3.0	1.2	0.3	1.8
Loaded Arm Hanging at Side (Additional 10 kg)						
LatRSA	0.3	1.30.4	0.8	1.8	0.4	2.4
HG	0.5	1.9	0.6	2.8	0.7	4.6
VG	0.8	3.0	0.9	4.0	1.1	6.0

Table G.2: Anterior Screw Bone Stresses

Hinge lateralization	90 th Percentile		95 th Percentile		99 th Percentile	
Anterior Screw	Mean σ (MPa)	Max σ (MPa)	Mean σ (MPa)	Max σ (MPa)	Mean σ (MPa)	Max σ (MPa)
1 Body Weight Shear and Compressive Load						
LatRSA	1.3	4.6	1.4	5.9	1.6	14.5
HG	1.2	3.8	1.4	5.5	1.7	15.5
VG	1.7	5.2	1.9	8.6	2.5	26.9
Unloaded 40° Abduction						
LatRSA	1.4	6.0	1.7	8.1	2.0	12.5
HG	0.6	2.1	0.7	2.8	0.8	7.6
VG	0.8	2.9	0.9	4.6	1.1	13.6
Loaded 90° Abduction						
LatRSA	2.8	10.6	3.3	13.6	3.9	30.8
HG	3.5	14.2	4.2	20.1	5.1	41.3
VG	4.8	20.4	5.8	27.9	7.0	52.0
Loaded 90° Forward Elevation						
LatRSA	6.8	29.5	8.3	40.8	10.4	91.4
HG	4.7	19.3	5.6	24.6	6.9	59.5
VG	12.1	51.5	14.8	74.6	18.4	160.5
Unloaded Arm Hanging at Side						
LatRSA	0.1	0.6	0.2	0.9	0.2	1.3
HG	0.1	0.2	0.1	0.2	0.1	0.7
VG	0.1	0.2	0.1	0.4	0.1	1.4
Loaded Arm Hanging at Side (Additional 10 kg)						
LatRSA	0.5	2.1	0.6	2.8	0.6	4.3
HG	0.2	0.6	0.2	0.8	0.3	2.4
VG	0.3	0.8	0.3	1.4	0.4	4.5

Table G.3: Superior Screw Bone Stresses

Hinge lateralization	90 th Percentile		95 th Percentile		99 th Percentile	
Superior Screw	Mean σ (MPa)	Max σ (MPa)	Mean σ (MPa)	Max σ (MPa)	Mean σ (MPa)	Max σ (MPa)
1 Body Weight Shear and Compressive Load						
LatRSA	2.2	7.7	2.6	12.2	3.1	22.8
HG	2.1	7.6	2.4	11.2	2.9	20.8
VG	2.9	10.4	3.4	15.7	4.1	28.4
Unloaded 40° Abduction						
LatRSA	1.0	3.4	1.2	5.4	1.4	10.2
HG	1.6	6.8	1.9	9.3	2.3	14.1
VG	1.6	5.7	1.9	8.7	2.3	15.9
Loaded 90° Abduction						
LatRSA	3.3	12.2	4.0	22.3	2.3	55.9
HG	3.8	13.6	4.5	23.5	5.9	60.6
VG	5.0	17.4	5.9	29.4	7.7	75.9
Loaded 90° Forward Elevation						
LatRSA	6.6	23.9	7.9	37.7	10.2	103.2
HG	5.1	19.1	6.1	34.0	7.9	79.1
VG	10.7	40.2	12.8	61.3	16.4	150.0
Unloaded Arm Hanging at Side						
LatRSA	0.1	0.4	0.1	0.5	0.2	1.2
HG	0.1	0.5	0.2	0.7	0.2	1.1
VG	0.2	0.8	0.2	1.0	0.3	1.6
Loaded Arm Hanging at Side (Additional 10 kg)						
LatRSA	0.4	1.2	0.4	1.8	0.5	3.9
HG	0.4	1.6	0.5	2.2	0.6	3.6
VG	0.7	2.0	0.8	3.3	0.9	5.3

Table G.4: Posterior Screw Bone Stresses

Hinge lateralization	90 th Percentile		95 th Percentile		99 th Percentile	
Posterior Screw	Mean σ (MPa)	Max σ (MPa)	Mean σ (MPa)	Max σ (MPa)	Mean σ (MPa)	Max σ (MPa)
1 Body Weight Shear and Compressive Load						
LatRSA	1.6	5.7	1.9	8.2	2.2	10.6
HG	1.8	6.4	2.1	9.1	2.5	12.1
VG	2.2	7.5	2.6	11.0	2.9	14.0
Unloaded 40° Abduction						
LatRSA	0.8	3.0	0.9	3.8	1.1	5.9
HG	0.9	3.3	1.0	4.2	1.2	6.7
VG	1.1	4.0	1.3	5.3	1.5	7.9
Loaded 90° Abduction						
LatRSA	2.7	11.0	3.3	16.8	3.9	24.7
HG	3.2	11.7	3.7	17.2	4.4	27.2
VG	4.9	17.0	5.8	23.9	6.7	39.0
Loaded 90° Forward Elevation						
LatRSA	6.3	20.3	7.3	28.4	8.3	48.9
HG	3.9	14.1	4.6	20.1	5.4	33.4
VG	12.3	40.2	14.2	54.7	16.2	90.8
Unloaded Arm Hanging at Side						
LatRSA	0.1	0.3	0.1	0.4	0.1	0.5
HG	0.1	0.4	0.1	0.5	0.1	0.8
VG	0.1	0.5	0.2	0.6	0.2	1.0
Loaded Arm Hanging at Side (Additional 10 kg)						
LatRSA	0.3	0.9	0.3	1.2	0.3	1.7
HG	0.4	1.3	0.1	1.8	0.5	2.5
VG	0.5	1.5	5	2.0	0.6	3.2

Table G.5: Inferior Screw Bone Stresses

Hinge lateralization	90 th Percentile		95 th Percentile		99 th Percentile	
Inferior Screw	Mean σ (MPa)	Max σ (MPa)	Mean σ (MPa)	Max σ (MPa)	Mean σ (MPa)	Max σ (MPa)
1 Body Weight Shear and Compressive Load						
LatRSA	1.6	5.0	1.9	1.2	2.5	31.9
HG	1.4	4.5	1.7	10.5	2.2	29.3
VG	2.1	6.5	2.5	13.4	3.0	37.9
Unloaded 40° Abduction						
LatRSA	1.0	3.0	1.2	6.0	1.5	18.9
HG	1.1	3.3	1.2	5.9	1.5	19.3
VG	1.6	4.6	1.8	7.7	2.2	24.9
Loaded 90° Abduction						
LatRSA	2.5	7.2	2.8	10.7	3.3	22.5
HG	2.6	7.2	2.9	10.6	3.4	21.8
VG	3.7	10.3	4.2	15.0	4.9	30.0
Loaded 90° Forward Elevation						
LatRSA	2.1	6.6	2.4	11.4	3.0	22.3
HG	2.1	5.8	2.4	11.1	2.9	19.5
VG	3.6	11.3	4.2	19.7	5.1	35.1
Unloaded Arm Hanging at Side						
LatRSA	0.1	0.2	0.1	0.6	0.1	1.9
HG	0.1	0.3	0.1	0.6	0.1	2.0
VG	0.1	0.5	0.2	0.7	0.2	2.7
Loaded Arm Hanging at Side (Additional 10 kg)						
LatRSA	0.2	0.7	0.3	2.0	0.4	6.0
HG	0.3	1.1	0.4	1.9	0.5	6.7
VG	0.5	1.5	0.5	2.4	0.7	8.6

Curriculum Vitae

Emily West
MESc Candidate

EDUCATION

- 2015-2017 Candidate for MESc (Biomedical Engineering) in collaboration with Musculoskeletal Health Research, Expected 2017
Supervisors: Dr. Louis Ferreira, Dr. George Athwal
The University of Western Ontario, London, Canada
- 2010-2015 BESC (Mechanical Engineering) with Professional Internship
Graduated with distinction, Deans list (2011- 2015)
The University of Western Ontario, London, Canada

WORK EXPERIENCE

- 2015-2017 **The University of Western Ontario**
Teaching Assistant (Product Design and Development)
Department of Mechanical and Materials Engineering
Teaching Assistant (Mechanical Engineering Design)
Department of Mechatronics Systems Engineering
- 2015 **SNC-Lavalin**, Sarnia, Ontario, Canada
Project Engineering Student
- 2013-2014 **LANXESS Inc.**, Sarnia, Ontario, Canada
Project Engineering Intern

HONOURS and AWARDS

- 2016 **Queen Elizabeth II Scholarship in Science and Technology (\$15,000)**
The University of Western Ontario
- 2011-2015 **Western Engineering Dean's Honour List**
The University of Western Ontario
- 2010 **Entrance Scholarship (\$2000)**
The University of Western Ontario

PUBLICATIONS and PRESENTATIONS

Papers Accepted to Refereed Journals

1. **E. West**, N. Knowles, G. Athwal, L. Ferreira. A 3D Comparison of Humeral Head Retroversion by Sex and Measurement Technique. *Shoulder & Elbow*. In Press 2017. DOI: 10.1177/1758573217711897

Submitted Manuscripts for Publication under Review

1. **E. West**, N. Knowles, L. Ferreira, G. Athwal. A comparison of anatomic to guide-assisted humeral head osteotomy dimensions during shoulder arthroplasty. *Shoulder & Elbow*. In Review 2017.

Proceedings of Refereed Conferences

1. **E. West**, N. Knowles, G. Athwal, L. Ferreira. A 3D Comparison of Humeral Head Retroversion by Sex and Measurement Technique. Orthopedic Research Society, Annual Meeting. San Diego, California, USA. (2017, Poster).
2. **E. West**, N. Knowles, G. Athwal, L. Ferreira. A 3D Comparison of Humeral Head Retroversion by Sex and Measurement Technique. International Society of Technology in Arthroplasty, Boston, Massachusetts, USA (2016, Podium).
3. **E. West**, N. Knowles, L. Ferreira, G. Athwal. Comparison of Humeral Head Osteotomy using Anatomic and Guide-Assisted Cuts. International Society of Technology in Arthroplasty, Boston, Massachusetts, USA (2016, Poster with short talk).
4. **E. West**, N. Knowles, L. Ferreira, G. Athwal. Comparison of Humeral Head Osteotomy using Anatomic and Guide-Assisted Cuts. Canadian Orthopedic Association, Annual Meeting. Quebec City, Quebec, Canada. (2015, Podium).
5. **E. West**, N. Knowles, L. Ferreira, G. Athwal. Comparison of Humeral Head Osteotomy using Anatomic and Guide-Assisted Cuts. Summer Biomechanics, Bioengineering and Biotransport Conference. National Harbor, Maryland, USA. (2016, Poster).

PROFESSIONAL MEMBERSHIPS

2015 Professional Engineers of Ontario (PEO): Engineer in Training (EIT)